THESIS

MODELING AND FIELD EVALUATION OF THE STRENGTH OF SURFACE SOILS FOR VEHICLE MOBILITY

Submitted by

Matthew J. Pauly

Department of Civil and Environmental Engineering

In partial fulfillment of the requirements

For the Degree of Master of Science

Colorado State University

Fort Collins, Colorado

Summer 2019

Master's Committee:

Advisor: Joseph Scalia
Co-Advisor: Jeffrey D. Niemann

Timothy R. Green
Gregory Butters

ABSTRACT

MODELING AND FIELD EVALUATION OF THE STRENGTH OF SURFACE SOILS FOR VEHICLE MOBILITY

Surficial soil strength is a critical variable in vehicle mobility and terrain trafficability analysis and varies substantially in time and space with soil moisture and texture. Fine-resolution (5-30 m grid cell) patterns of soil strength and soil moisture are necessary for routing of off-road vehicle operations and must be estimated for applications when direct measurement is too expensive, labor-intensive, or dangerous. Rating cone index (RCI) is the in-situ method typically used in mobility applications to empirically evaluate the strength of surficial soils. The RCI method provides one simple parameter to evaluate soil trafficability, but in doing so fails to separately characterize the various mechanisms (compressibility, stress independent shear strength, stress dependent shear strength) that govern soil behavior in relation to vehicle traffic. Alternatively, the Bekker soil strength framework, which encompasses pressure-sinkage and shear strength soil properties, offers a mechanics-based representation of soil behavior and has received increased interest from the terramechanics community in recent years. However, because RCI has been the focus of the terramechanics community over several decades, predictive relationships to estimate Bekker parameters using basic spatially- and temporally-variable input data (soil moisture and soil composition) do not exist. The objective of this study is to develop and evaluate a framework for prediction of Bekker parameters (cohesion and friction angle) as a function of soil moisture and soil texture (percentage of sand and clay). A model, termed the Strength of Surface Soils (STRESS) model, is introduced to estimate shear strength of surface soils using soil moisture,

pedotransfer functions based on soil texture, and unsaturated soil mechanics. The STRESS model is paired with an existing soil moisture downscaling model, the Equilibrium Moisture from Topography, Vegetation, and Soil (EMT+VS) model. The pre-existing EMT+VS model includes two untested simplifications that make the model inconsistent with the STRESS model framework, so two previously neglected soil-related hydrologic considerations are introduced to the EMT+VS model: runoff and residual water content. The impacts of runoff and residual on soil moisture downscaling performance and spatial patterns of soil moisture are assessed at a test region in northeastern Colorado called Drake Farm with measured soil moisture data for model calibration and evaluation. The additions are successfully included in the EMT+VS model but the assumptions made in the pre-existing EMT+VS model are shown to be adequate for soil moisture downscaling. After assessing EMT+VS model additions, the STRESS model is applied to Drake Farm to produce spatial patterns of estimated friction angle and cohesion. Model estimates are compared to measured shear strength using a human-powered shear strength bevameter to evaluate the predictive capability of the STRESS model. The model is found to underpredict friction angle and overpredict cohesion at Drake Farm due in part to the use of class-average effective shear strength parameters that do not appear to adequately reflect the properties of surficial soils. Finally, the design and construction of two bevameters are summarized for field and laboratory measurement of Bekker parameters. The results of laboratory tests on the human-powered shear strength bevameter used in STRESS model evaluation are compared to traditional geotechnical strength testing to validate field-testing results and ensure repeatability of measurements. Additionally, the design and construction of a fully automated, laboratory-focused bevameter device with pressure-sinkage and shear strength testing capabilities are described, but this bevameter is not used for testing in this study.

ACKNOWLEDGEMENTS

I gratefully acknowledge the United States Army Research Laboratory Small Business Innovation Research program and the USDA National Institute for Food and Agriculture, Hatch Project 1009616 for their generous financial support. I would like to thank my advisors Dr. Joe Scalia and Dr. Jeff Niemann for their guidance on this project. I also thank committee members Tim Green and Greg Butters as well as Andy Jones, Rob Erskine, Pete Grazaitis, and Paramsothy Jayakumar for their suggestions and collaboration in this work. Finally, I thank Joe Bindner for his assistance in laboratory and field testing, model calibration, and data processing and Logan Pokallus for laboratory support and assistance in electrical design of testing equipment.

TABLE OF CONTENTS

1. INTRODUCTION

Assessing vehicle mobility is a challenge for any application in which a vehicle must traverse natural terrain. Evaluation and prediction of terrain trafficability is crucial to agriculture, forestry, and military applications. Military organizations in the United States and throughout the world are among the key developers and users of vehicle mobility analyses. Concerns of terrain trafficability led to the first formal mobility analyses after wet, soft soils caused vehicle immobilization in World War II (Rula and Nuttall, 1971). Over the several decades since World War II, the U.S. Army and North Atlantic Treaty Organization (NATO) have developed multiple iterations of a military mobility model, termed the NATO Reference Mobility Model (NRMM) to assist in military operations planning (Jurkat et al., 1975; Haley et al., 1979; Ahlvin and Haley, 1992). Each version of the NRMM contains three modules to analyze mobility based on terrain, vehicle, and driver/operator variables. Within the terrain module, soil texture, volumetric water content (soil moisture), soil strength, slope, surface roughness, obstacles (e.g., vegetation, water), and other characteristics are analyzed to determine optimal routing and maximum attainable speeds. Soil strength is a critical variable in evaluation and prediction of off-road vehicle mobility. The strength of surficial soils is controlled by several material properties, including texture (percentage of sand, silt, and clay), density, water content, and organic matter content. Therefore, accurately characterizing soil moisture and corresponding moisture-variable soil strength is integral to vehicle mobility analysis.

Terramechanics is a sub-discipline of mechanical engineering focused on off-road machine's performance in relation to the terrain (Wong, 2010). Methods of characterizing soil strength for vehicle mobility differ from traditional geotechnical testing methods because the soil

conditions and applications differ greatly. In-situ testing methods are generally preferred in terramechanics to determine near-surface soil properties. The soil depth relevant to terramechanics applications (i.e. critical depth) can vary based on soil type, water content, density, and dimensions of the tire or track contacting the soil because the shear stress distribution below the tire or track depends on these variables. The critical depth can vary from what is considered to be the surficial layer (between 0 and 15 cm) to a depth of 60 cm. In most relevant soils, the critical soil layer is the surficial layer, and terramechanics strength measurement methods are typically conducted on the surface to classify the behavior of this critical layer (Wong, 2010). Two in-situ methods are widely used to quantify surface soil strength: rating cone index (RCI) and the Bekker soil strength framework. Rating cone index (RCI) is measured by pushing a circular cone into the soil (Knight, 1956). Force required to insert the cone into soil is divided by the area of the cone to produce the cone index (CI) of the specific measured soil. Cone index is calculated in pounds-per-square-inch (psi) but presented as a dimensionless value. For fine-grained soils, a remolding index (RI) is multiplied by CI to produce RCI. For coarse-grained soils, no RI is necessary and the term RCI is used interchangeably with CI. The RCI is compared to an empirically determined vehicle cone index (VCI) for a specific vehicle to determine if soil is trafficable on a go/no-go basis. The RCI method provides a single quantity to characterize soil trafficability, which according to Bekker (1956) depends on two primary aspects of soil behavior: stability (shear strength) and elasticity (compressibility).

The RCI framework has been used in development of terramechanics databases for decades and therefore is the state-of-practice for the U.S. Army and NATO in mobility modeling. The RCI method is preferred to the Bekker method for simplicity and historic use in military applications (Rula and Nuttall, 1971). However, in many military mobility applications, even the simple RCI

measurement method can be too expensive, labor-intensive, or dangerous for extensive field measurement. For scenarios in which soil strength cannot be directly measured, RCI must be estimated as a function of basic soil properties and soil moisture. The U.S. Army has developed several models to predict soil moisture and soil strength (Smith and Meyer, 1973; Sullivan et al., 1997; Mason et al., 2001; Frankenstein and Koenig., 2004). Each model relies on some variation of a simple water budget framework to estimate soil moisture. In each model, the water budget soil moisture estimates are applied to simple RCI predictive functions from Smith and Meyer (1973) to calculate RCI as a function of soil moisture and Unified Soil Classification System (USCS) classification.

Although RCI has been the preferred soil strength framework of the U.S. Army and NATO over several decades, the Bekker soil strength framework has received increased interest in recent years (McCullough et al., 2017). Numerical models incorporating Bekker parameters as inputs (Choi et al., 2018) are increasingly used to predict speed-made-good and other trafficability metrics. Additionally, Williams et al. (2017) analyzed relationships between CI and several variables related to vehicle performance and showed poor correlations in many cases, indicating that CI is often not suitable for predicting soil strength for vehicle mobility.

The Bekker method characterizes shear strength and compressibility using a bevameter (Bekker, 1956; 1960). The Bekker framework measures compressibility using a pressure-sinkage test and shear strength using a Mohr-Coulomb failure envelope (Coulomb, 1776; Mohr, 1900). This method lacks a simple metric to determine trafficability (such as the RCI-VCI comparison) but provides a more unique description of soil behavior for input into physics-based models (Choi et al., 2018) because shear strength and compressibility are considered separately. Shear strength is also further partitioned into frictional (exterior stress dependent) and cohesive (exterior stress

independent) strength components. The two-fold parameterization of shear strength holds the advantage of incorporation into complex terramechanics numerical models. Despite the advantages of the Bekker method, no model framework exists to predict Bekker parameters from basic soil properties for scenarios in which direct sampling is not an option.

The objective of this study is to develop and evaluate a model framework for prediction of Bekker shear strength parameters as a function of soil moisture and soil texture. The resulting framework is termed the Strength of Surface Soils (STRESS) model. Like soil strength, direct measurement of soil moisture is often difficult or impossible. Therefore, soil moisture must also be estimated. The STRESS model is paired with the Equilibrium Moisture from Topography, Vegetation, and Soil (EMT+VS) model, an existing soil moisture downscaling model, to achieve fine resolution patterns of soil moisture and soil strength for vehicle mobility. Downscaled patterns of soil moisture from the EMT+VS model are input into the STRESS model along with soil textural data (percentage of sand and clay) derived from local data or large-scale databases to estimate spatial patterns of Bekker shear strength parameters using unsaturated soil mechanics. The pre-existing EMT+VS model neglects residual water content, making the pre-existing model inconsistent with the STRESS model framework. Additionally, runoff (another soil-related consideration), is also neglected in the pre-existing EMT+VS model. Thus, to generalize the EMT+VS model and address the prior simplifications, two soil-related hydrologic considerations (runoff and residual water content) are included in the EMT+VS model. Runoff and residual water content are implemented into the EMT+VS model and their effect on model performance and spatial patterns of soil moisture are examined at a test region in northeastern Colorado called Drake Farm. Chapter 2 (EMT+VS Model Development) describes the pre-existing EMT+VS model, introduces updates to the model, and summarizes the effects of those updates on model

performance and patterns of soil moisture. The STRESS model is then developed by applying unsaturated soil mechanics to surficial soils. The predictive performance of the STRESS model is evaluated using a shear strength bevameter at Drake Farm. Chapter 3 (STRESS Model Development) describes the STRESS model methodology and summarizes field evaluation procedure and results. A field-focused shear strength bevameter is designed and constructed for field evaluation of the STRESS model discussed in Chapter 3. Chapter 4 (Bevameter Design) describes design, construction and laboratory validation of the field-focused shear strength bevameter. Additionally, a laboratory-focused bevameter capable of performing both bevameter tests is designed and constructed but is not validated in the laboratory in this study. The design of this device is also discussed in Chapter 4. Conclusions, tables, and figures pertaining to each portion of the study are presented at the end of each chapter. A full list of references is provided at the end of the document.

2. EMT+VS MODEL DEVELOPMENT

2.1 Introduction

Volumetric water content (soil moisture) is a critical variable in many hydrologic, geomorphic, atmospheric, and biologic processes. Fine-resolution maps (10 – 100 m grid cells) of soil moisture are important for agricultural production (Holzman et al., 2014; Phillips et al., 2014), weather and climate modeling (Dirmeyer, 1999; Seuffert et al., 2002), and forest fire prediction (Bartsch et al., 2009). Additionally, soil moisture affects soil strength and compressibility, which are vital to terrain trafficability and vehicle mobility routing (Horn and Fleige, 2003).

Satellite remote sensing is used to estimate soil moisture but at a resolution that is too coarse for many applications. Advanced Microwave Scanning Radiometer-EOS (AMSR-E) (Njoku et al., 2003), Soil Moisture and Ocean Salinity (SMOS) (Kerr et al., 2010), and Soil Moisture Active Passive (SMAP) (Entekhabi et al., 2010; Reichle et al., 2017) measure soil moisture at resolutions ranging from 5 km to 60 km grid cells. Various downscaling methods can be used to produce fine-resolution soil moisture maps from coarse-resolution data. One downscaling technique uses optical/thermal data to estimate fine-resolution soil moisture patterns (Chauhan et al., 2003; Merlin et al., 2005; Merlin et al., 2006; Das et al., 2011; Song et al., 2014; Peng et al., 2016). Optical/thermal methods typically downscale soil moisture to a resolution of 1 km grid cells based on the spatial resolution of the optical/thermal remote sensing data. Another method of downscaling aims to reproduce statistical properties of soil moisture patterns using empirical relationships with ancillary data (Crow et al., 2000; Kim and Barros, 2002; Mascaro et al., 2011). A third downscaling technique, called geo-information downscaling, infers soil moisture patterns from fine-resolution topographic, vegetation, and soil attributes. Many geo-

information methods rely on empirical relationships between soil moisture and the fine-resolution attributes to predict patterns of soil moisture (Wilson et al., 2005; Busch et al., 2012). Other geo-information downscaling methods use models for vadose-zone hydrology to represent major hydrologic processes (Pellenq et al., 2003; Coleman and Niemann, 2013; Ranney et al., 2015). These methods infer fine-resolution patterns of soil moisture by predicting the effects of topographic, vegetation, and soil characteristics on hydrologic processes in the vadose-zone.

The Equilibrium Moisture from Topography, Vegetation, and Soil (EMT+VS) model (Ranney et al. 2015) is a geo-information downscaling method that models the water balance in the hydrologically active soil layer using topographic, vegetation, and soil characteristics. Coleman and Niemann (2013) initially introduced the model as the Equilibrium Moisture from Topography (EMT) model to analyze topographic dependence and temporal instability of fine-resolution soil moisture patterns. Ranney et al. (2015) generalized the model to accept fine-resolution variations in vegetation and soil characteristics. Cowley et al. (2017) added precipitation and potential evapotranspiration (PET) downscaling to the EMT+VS model to assess their impacts on soil moisture patterns. Hoehn et al. (2017) generalized the model to accept multiple coarse grid cells as inputs. Werbylo and Niemann (2014) and Greico et al. (2018) evaluated the performance of the model when calibration data are limited or absent, and Deshon (2018) introduced a stochastic component to capture variability in soil moisture that cannot be explained by the deterministic inputs. The EMT+VS model has been applied at fine resolutions ranging from 10 m to 30 m grid cells and at depths ranging from the top 5 cm to 30 cm of the soil. The model has been applied to and evaluated at regions ranging from 6 ha (0.06 km^2) to 239 km^2.

Ranney et al. (2015) examined the effects of soil properties on soil moisture patterns by considering spatial variations of porosity and saturated vertical hydraulic conductivity in the

EMT+VS model. However, two important aspects of soil hydrology were not considered in that analysis: runoff and residual water content. Runoff is known to depend on antecedent soil moisture for both saturation-excess and infiltration-excess conditions. Studies have shown a link between saturation-excess runoff and antecedent soil moisture in temperate to subtropical regions with moderate to high annual precipitation (Western et al., 1998; Brocca et al., 2004, Wei et al., 2007). Fitzjohn et al. (1998), Zhang et al. (2011), and Schoener and Stone (2019) also demonstrated a relationship between runoff production and antecedent soil moisture in dry climates with sudden, high-intensity rainfall. Additionally, Fitzjohn et al. (1998) showed that runoff production can be highly variable in space due to fine-resolution variation in soil moisture and soil composition. Although numerous studies have examined the effects of antecedent soil moisture on runoff production, the impact of runoff production on the resulting soil moisture patterns is unknown. Runoff production could impact the spatial structure of fine-resolution soil moisture patterns, and thus affect soil moisture downscaling. If the quantity of water that can enter the soil is limited by the infiltration capacity (thus producing runoff), then the subsurface is expected to be drier. Additionally, runoff could travel downslope and infiltrate elsewhere, redistributing the moisture within a region. Runoff is neglected in the pre-existing EMT+VS model and the effect of runoff on soil moisture patterns is not currently assessed.

Residual water content is a component of soil water retention and flow behavior that was not considered by Ranney et al. (2015). Brooks and Corey (1964) introduced residual saturation as the volumetric water content at which hydraulic conductivity approaches zero. Soil water flux ceases at residual water content because soil surface adsorption and discontinuous flow paths disallow conduction of liquid water (Luckner et al., 1989). Recent studies have demonstrated the ability to infer spatial patterns of soil water retention parameters such as permanent wilting point,

field capacity, and porosity from spatial patterns of soil moisture (Bandara et al., 2014; Chandler et al., 2017). Although these studies do not include residual water content, such relationships between soil moisture and other soil water retention characteristics indicate the potential for a link between soil moisture and residual water content. Grayson et al. (2006) demonstrated the effect of residual water content on coarse-resolution soil moisture patterns by varying soil input data in a land-surface model over the whole of Australia. Placing a lower bound on soil moisture at residual water content scales hydrologic processes from residual to porosity rather than from zero to porosity. The effective degree of saturation depends on this lower bound and affects unsaturated hydraulic conductivity and evapotranspiration (ET). During dry conditions, soil moisture is at or very close to the residual and spatial patterns of soil moisture will be determined by spatial patterns of residual water content. The EMT+VS model presents an opportunity to investigate the effects of residual water content on soil moisture patterns at a much finer scale than previously studied by Grayson et al. (2006).

Greico et al. (2018) compared the performance of the locally calibrated EMT+VS model for all previously examined test regions. Model performance was plotted as a function of the spatial average soil moisture. For several regions, the model performs best under moderate soil moisture conditions and decreases for particularly dry or wet dates. The poorer performance for extreme conditions is important because such conditions are often the most critical for applications such as agriculture and vehicle mobility (Wong, 2010; Wijewardana et al., 2018). Implementing runoff and residual water content into the EMT+VS model has the potential to improve model performance for these extreme conditions. Wet conditions are likely to occur shortly after storm events, so those soil moisture patterns might depend on runoff production. During dry conditions,

soil moisture patterns are expected to reflect the pattern of residual water content as shown by Grayson et al. (2006) at larger scales.

The objectives of this study are to examine the effects of runoff production and residual water content on spatial patterns of soil moisture and to determine whether these factors improve soil moisture downscaling. A conceptual runoff expression and residual water content are implemented in the EMT+VS model, and the pre-existing and generalized EMT+VS models are applied to a test region (Drake Farm) that has soil moisture observations available for model calibration and evaluation. During the period of observation, Drake Farm was managed in three distinct manners. In earlier years, the field was under a non-irrigated wheat-fallow crop rotation with a varying spatial pattern of vegetation. Numerous high intensity rainfall events produced measured runoff at a flume near the field's edge. Native grasses were planted over the entire site, and an intermediate period occurred in which the grasses were not yet mature. This intermediate portion is not considered in this study. In later years, the native grasses have become fully mature, and no runoff has been observed at the flume despite the occurrence of several large rainfall events. All three model versions (pre-existing, runoff, residual) are calibrated separately for the initial and final land management periods, and the results are compared to determine the effects of runoff and residual water content on soil moisture downscaling. The calibrated model parameters are also compared between the two land management conditions to understand why the runoff production behavior changed between the two periods.

2.2 Methods and Materials

2.2.1 Pre-existing EMT+VS Methodology

The EMT+VS model simulates a water balance over the hydrologically active layer, which is the soil layer between the surface and any semi-impervious layer that might induce lateral flow.

Four hydrologic processes are included in the water balance: infiltration f, deep drainage G, lateral flow L, and ET E. Key inputs to the model are spatial average (or coarse resolution) soil moisture on the date of interest and fine-resolution topographic, vegetation, and soil data. The model outputs a fine-resolution soil moisture map on the same date. Detailed descriptions and complete equations for the model are provided by Coleman and Niemann (2013), Ranney et al. (2015), and Cowley et al. (2017).

The EMT+VS model's infiltration expression starts with a spatial average precipitation rate that includes both storm and inter-storm periods. The spatial average is downscaled based on orographic effects (Cowley et al., 2017) to produce a fine-resolution pattern of precipitation. The spatial average precipitation itself eventually cancels out of EMT+VS model equations and does not need to be specified. Interception by the canopy is then included to determine the throughfall pattern. In the pre-existing EMT+VS model, all throughfall is assumed to infiltrate.

Deep drainage is characterized using Darcy's Law and assuming flow is gravity driven. The Campbell (1974) equation is used to estimate vertical unsaturated hydraulic conductivity. Lateral flow is also described using Darcy's Law with horizontal unsaturated hydraulic conductivity from Campbell (1974) and including anisotropy. The hydraulic gradient in the horizontal direction is a power function of topographic slope, and the thickness of the hydrologically active layer can vary with topographic curvature (Heimsath et al., 1999). The ET expression first downscales the spatial average PET to account for elevation effects (Cowley et al., 2017). The resulting PET is then partitioned into radiation and aerodynamic terms according to the Priestley-Taylor assumption (Priestley and Taylor, 1972). The radiation term accounts for topographically induced variations in insolation. Actual ET is determined from the PET based on

the magnitude of soil moisture. Shading of the soil surface by vegetation and the portion of the roots in the hydrologically active layer are also considered.

Fine-resolution soil moisture is estimated using an analytical approach developed by Coleman and Niemann (2013). The modeled layer is assumed to be at equilibrium, and therefore the effects of hysteresis are neglected. Four explicit solutions are calculated under the assumption that each outflow term (deep drainage, lateral flow, radiation ET, aerodynamic ET) dominates the water balance. The final soil moisture estimate θ is calculated as a weighted average of the four solutions:

$$\theta = \frac{w_G\theta_G + w_L\theta_L + w_R\theta_R + w_A\theta_A}{w_G + w_L + w_R + w_A} \tag{2.1}$$

where θ_G, θ_L, θ_R, and θ_A are the soil moisture estimates if deep drainage, lateral flow, radiation ET, and aerodynamic ET dominate, respectively, and w_G, w_L, w_R, and w_A are the weights associated with each process. Each explicit solution is calculated as a function of the spatial average soil moisture and the fine resolution topographic, vegetation, and soil attributes. The weights are determined from the magnitude of each outflow term in the water balance and depend in part on the spatial average soil moisture.

2.2.2 EMT+VS Model with Runoff

Runoff occurs when throughfall exceeds the soil's infiltration capacity. Runoff can be represented in the EMT+VS model by estimating an infiltration capacity based on soil properties and inducing runoff when throughfall exceeds infiltration capacity. Green and Ampt (1911) introduced a soil-dependent infiltration model that is widely used in modern modeling tools such as the Hydrologic Engineering Center - Hydrologic Modeling System (HEC-HMS) (Scharffenberg, 2016) and Gridded Surface Subsurface Hydrologic Analysis (GSSHA) (Downer

and Ogden, 2006). The Green-Ampt model has also been shown to produce similar results to Richards equation (Hsu et al., 2002; Dussaillant et al., 2003). The Green-Ampt model relies on the assumption of an abrupt wetting front. Water is assumed to move downward into the soil column with a sharp distinction between the saturated soil and the soil at the uniform initial water content. If the infiltration capacity limits the infiltration rate, the Green-Ampt model can be used to estimate infiltration rate as:

$$f_P = K_{s,v}\left[1+\frac{\left|\psi_f\right|\left(\theta_s-\theta_i\right)}{F_P}\right] \tag{2.2}$$

where f_P is the infiltration rate during a storm, $K_{s,v}$ is saturated vertical hydraulic conductivity, ψ_f is suction head at the wetting front, θ_s is porosity, θ_i is initial soil moisture, and F_P is cumulative infiltration. Although time does not appear in the equation, f_P decreases as F_P increases during a storm. In the brackets of Eqn. [2.2], the first term represents the effects of gravity, while the second term represents the effects of the capillary gradient. The deep drainage and lateral flow expressions in the EMT+VS model assume that flow is gravity driven, so the capillary gradient is also neglected here. Equation [2.2] then simplifies to:

$$f_P = K_{s,v} \tag{2.3}$$

While this infiltration expression is simplistic, preliminary tests with the EMT+VS model showed that including the capillary term provided little improvement in performance while adding several parameters.

Infiltration during a storm can either be limited by the available throughfall or by the soil's infiltration capacity. Thus, a generalized infiltration expression can be written to account for both scenarios:

$$f_P = \min\begin{Bmatrix} \overline{P}_i O_F \left(1-\lambda V\right) \\ K_{s,v} \end{Bmatrix} \tag{2.4}$$

where $\overline{P_i}$ is spatial average rainfall intensity during a storm, O_F is a function that accounts for orographic effects on precipitation as described by Cowley et al. (2017), λ is the vegetation's interception efficiency, and V is the fractional vegetation cover. Rearranging variables, the infiltration equation can be rewritten as:

$$f_P = \overline{P_i} O_F \left(1-\lambda V\right) I_F \tag{2.5}$$

where I_F is an infiltration function that is defined as:

$$I_F = \min\begin{Bmatrix} 1 \\ \dfrac{K_{s,v}}{\overline{P_i} O_F \left(1-\lambda V\right)} \end{Bmatrix} \tag{2.6}$$

This infiltration function transitions abruptly from throughfall-limited infiltration to soil-limited infiltration when $K_{s,v} / \left[\overline{P_i} O_F \left(1-\lambda V\right)\right] = 1$. This sharp break is likely unrealistic due to sub-grid variations in soil properties, so a smooth function was selected to replace the segmented infiltration function. The selected function must have a lower bound for the input $K_{s,v} / \left[\overline{P_i} O_F \left(1-\lambda V\right)\right]$ at zero and no upper bound. Additionally, the function's output must begin at zero and increase monotonically to one. The cumulative distribution function for an exponential distribution meets these requirements. Using this function, I_F can be rewritten as:

$$I_F = 1 - \exp\left\{-\frac{\upsilon_r K_{s,v}}{\overline{P_i}(1-\lambda V)}\right\} \tag{2.7}$$

where υ_r describes the rate at which I_F transitions between zero and one. Figure 2.1 shows a comparison between the pre-existing EMT+VS model's infiltration function ($I_F = 1$), the

segmented infiltration function (Eqn. [2.6]), and the exponential infiltration function (Eqn. [2.7]). The exponential function closely approximates the segmented function when $\upsilon_r = 2$, so this value is used throughout this study. The average rainfall intensity $\overline{P_i}$ is a new model parameter, which is expected to vary date by date as different storms occur.

The EMT+VS model simulates equilibrium including both storm and inter-storm periods, so Eqn. [2.7] must be generalized to account for both types of periods. The original infiltration equation is therefore updated to be:

$$F = \overline{P} O_F (1 - \lambda V) I_F \tag{2.8}$$

where $\overline{P}$ is the average precipitation rate including both storm and inter-storm periods (which still eventually cancels out of the model). $\overline{P_i}$ remains present within the I_F function. Note the distinction between $\overline{P_i}$ and $\overline{P}$, where $\overline{P_i}$ represents spatial-average precipitation intensity while a storm is occurring, and $\overline{P}$ is the spatial average precipitation rate considering both storm and inter-storm periods. For simplicity, runoff generated at one location is assumed to be transported out of the region and does not get redistributed to downslope locations.

2.2.3 EMT+VS Model with Residual Water Content

Residual water content is defined as the soil moisture below which hydraulic conductivity is zero (Brooks and Corey, 1964; van Genuchten et al., 1991). At very low soil moisture, soil pore water is immobilized because all liquid water is adsorbed to soil particles and the water phase is discontinuous (Luckner et al., 1989; Vanapalli et al., 1998). Residual water content is included in the EMT+VS model by adjusting all flow processes so they cease when soil moisture reaches residual water content θ_r. A degree of saturation term $\left(\theta / \theta_s\right)$ appears in the pre-existing EMT+VS model to estimate unsaturated hydraulic conductivity and to account for soil moisture

limitations on ET. In the EMT+VS model with residual water content, that degree of saturation term is replaced with an effective saturation term $(\theta - \theta_r)/(\theta_s - \theta_r)$. Thus, deep drainage and lateral flow do not occur below the residual water content (for reasons of adsorption and discontinuous flow paths as described previously). ET is also zero below the residual water content. van Genuchten (1980) defined residual water content as the soil moisture at the permanent wilting point, which is typically assumed to be 1500 kPa. In practice, residual water content can represent the water content at a suction between 1500 kPa and $1*10^6$ kPa, depending on curve-fitting techniques, quantity of data, and capabilities of measurement equipment (Nitao and Bear, 1996; Vanapalli et al., 1998). Therefore, residual water content represents the soil moisture at the permanent wilting point or drier. At all water contents less than permanent wilting point, transpiration no longer occurs because plants cannot generate high enough suction to draw water out of the soil (Laio et al., 2001; Porporato et al., 2001). In a model by Laio et al. (2001) that determines evaporation as a function of soil moisture, evaporation is assumed to converge to zero at a soil's hygroscopic water content. The model estimates very low magnitudes of evaporation at soil moisture values between the hygroscopic state and permanent wilting point. Because residual water content likely falls between these two values, the very small ET that occurs below residual is neglected.

2.2.4 EMT+VS Equations with Runoff and Residual

Implementing both model updates produces the following generalized analytical soil moisture solutions:

$$\theta_G = \theta_r + \left(\overline{\theta} - \overline{\theta_r}\right)\frac{DDI}{\overline{DDI}} \tag{2.9}$$

$$\theta_L = \theta_r + \left(\overline{\theta} - \overline{\theta_r}\right)\frac{LFI}{\overline{LFI}} \tag{2.10}$$

$$\theta_R = \theta_r + \left(\overline{\theta} - \overline{\theta_r}\right)\frac{REI}{\overline{REI}} \tag{2.11}$$

$$\theta_A = \theta_r + \left(\overline{\theta} - \overline{\theta_r}\right)\frac{AEI}{\overline{AEI}} \tag{2.12}$$

where $\overline{\theta}$ is spatial average (or coarse resolution) soil moisture, $\overline{\theta_r}$ is spatial average residual water content, DDI is deep drainage index, LFI is lateral flow index, REI is radiation ET index, and AEI is aerodynamic ET index. $\overline{DDI}$, $\overline{LFI}$, $\overline{REI}$, $\overline{AEI}$ are the spatial averages of the indices. The indices are defined as:

$$DDI = \left(\theta_s - \theta_r\right)\left[\frac{O_F\left(1-\lambda V\right)I_F}{K_{s,v}}\right]^{1/\gamma_v} \tag{2.13}$$

$$LFI = \left(\theta_s - \theta_r\right)\left[\frac{O_F\left(1-\lambda V\right)I_F}{\delta_0 \iota K_{s,v}}\right]^{1/\gamma_h}\left(\frac{A}{cS^{\varepsilon}}\right)^{1/\gamma_h}\left(\frac{\kappa_{\min}}{\kappa_{\min}-\kappa}\right)^{1/\gamma_h} \tag{2.14}$$

$$REI = \left(\theta_s - \theta_r\right)\left\{\frac{1+\alpha}{\overline{E_p}\left[1+\omega\left(\overline{Z}-Z\right)\right]}\right\}^{1/\beta_r}\left(\frac{1}{I_p}\right)^{1/\beta_r}\left[\frac{O_F\left(1-\lambda V\right)I_F}{\eta V+\left(1-V\right)^{\mu}}\right]^{1/\beta_r} \tag{2.15}$$

$$AEI = \left(\theta_s - \theta_r\right)\left\{\frac{1+\alpha}{\alpha\overline{E_p}\left[1+\omega\left(\overline{Z}-Z\right)\right]}\right\}^{1/\beta_a}\left[\frac{O_F\left(1-\lambda V\right)I_F}{\eta V+\left(1-V\right)^{\mu}}\right]^{1/\beta_a} \tag{2.16}$$

where γ_v is vertical pore disconnectedness index, δ_0 is the thickness of the hydrologically active layer where topographic curvature is zero, ι is anisotropy of hydraulic conductivity, A is upslope contributing area, S is topographic slope, γ_h is horizontal pore disconnectedness index, c is the linear dimension of the fine-resolution grid cells, ε is a parameter that relates horizontal hydraulic gradient to slope, κ is topographic curvature, $\kappa_{\min}$ is the minimum topographic curvature for which the active layer is present, α is the Priestley-Taylor coefficient minus one, $\overline{E_p}$ is the spatial

average PET, ω controls the elevation dependence of PET, Z is elevation, $\overline{Z}$ is spatial average elevation, I_P is potential solar radiation index (PSRI) (Dingman, 2002), β_r controls the effect of soil moisture on radiation ET, η is the portion of transpiration that is derived from the modeled soil layer, μ controls the effect of shading on soil evaporation, and β_a controls the effect of soil moisture on aerodynamic ET. Finally, the weights are calculated as:

$$w_G = \left(\frac{\overline{\theta} - \overline{\theta_r}}{\overline{DDI}} \right)^{\gamma_v} \tag{2.17}$$

$$w_L = \left(\frac{\overline{\theta} - \overline{\theta_r}}{\overline{LFI}} \right)^{\gamma_h} \tag{2.18}$$

$$w_R = \left(\frac{\overline{\theta} - \overline{\theta_r}}{\overline{REI}} \right)^{\beta_r} \tag{2.19}$$

$$w_A = \left(\frac{\overline{\theta} - \overline{\theta_r}}{\overline{AEI}} \right)^{\beta_a} \tag{2.20}$$

The weights and explicit solutions are applied to Eqn. [2.1] to determine the final soil moisture estimate within each fine resolution grid cell.

Runoff production and residual water content can vary between fine resolution grid cells in the EMT+VS model, but spatial variations in runoff and residual rely entirely on spatially variable vegetation and soil data. One can show that if vegetation and soil properties are spatially constant, then the infiltration function cancels out of all EMT+VS model equations and therefore has no effect on the model results. For the same case, residual water content remains in a portion of the EMT+VS model, but it drops out of some calculations and has a lesser impact on EMT+VS model results.

2.2.5 Test Site Description and Available Datasets

The EMT+VS model was applied to Drake Farm, a former farm field in northeastern Colorado. Drake Farm has been the subject of various hydrologic studies (e.g., Green et al., 2009; Green and Erskine, 2011) but has not been used for soil moisture downscaling in the past. This region was selected because it has soil moisture data corresponding to multiple vegetation conditions, soil texture data at multiple locations, and runoff monitoring near the field's edge.

Drake Farm has an area of approximately 100 ha. The field was farmed in a wheat-fallow rotation (WFR) for multiple decades through 2012. In 2013 and 2014, the field was converted into a Conservation Reserve Program (CRP) site, and a blend of native grasses and alfalfa was planted. A transitional period occurred between the WFR period and the CRP period prior to the native grasses and alfalfa becoming fully mature. In 2015, the native grasses and alfalfa became mature and the CRP period began. Only the WFR and CRP periods are considered in this study. Vegetation at the site currently consists of native grasses, alfalfa, shrubs, and invasive weeds. The climate is semiarid with average annual precipitation and PET of 350 and 1200 mm, respectively (Green and Erskine, 2011). Soil moisture data from a portable time domain reflectometry (TDR) device are available for the WFR period (2012 and prior) and the CRP period (2015 to present). During the WFR period, soil moisture data are available for the top 30 cm of the soil on 10 dates ranging from 7 May 2003 to 1 July 2009. The measurement locations typically follow the orientation of the wheat-fallow crop strips, but the exact locations vary date by date. An example soil moisture sampling pattern from 24 June 2004 is shown in Fig. 2.2a. During the CRP period, soil moisture observations for the top 15 cm of the soil were collected in a star pattern consisting of 65 points on the northeastern side of the field (Fig. 2.2b). Adjacent points in each prong of the star are 25 m apart. For the CRP period, soil moisture data are available on 8 dates ranging from 18 April 2016

to 22 May 2018. A 17.4 ha rectangular region is defined around the star pattern and used as the EMT+VS application region (Fig. 2.2). Although some WFR observations extend beyond the rectangle, this region is used to allow a direct comparison between the WFR and CRP cases. A digital elevation model (DEM) is available for the site on a 5 m grid and is shown underlying the soil moisture measurement locations in Fig. 2.2a and 2.2b.

Soil texture data (sand, silt, and clay percentages) over the top 30 cm of soil are available at 215 points spanning the entire farm field (McCutcheon et al., 2006). We developed gridded maps for the sand and clay percentages in ArcGIS using tension spline interpolation (Fig. 2.2c and 2.2d). Tension spline interpolation (Mitas and Mitasova, 1988) was selected because it produced smoother, more natural interpolated patterns than other available methods (kriging, inverse distance weighting, and natural neighbor methods). Tension spline interpolation requires specification of a weight parameter, which determines the tension of the interpolated surface. Low tensions can produce maxima and minima that exceed the bounds of the measured data. At higher tensions, the surface becomes less smooth. As the weight value approaches infinity, the pattern approaches a spatial average except at points with measured data. The tension was set to 100 because this value avoids unrealistic overshoots that occur with lower weights and maintains smoothness that is lost as the weight approaches infinity.

Split sample testing was used to evaluate the predictive performance of the interpolated surfaces for various weight values. Five samples, each consisting of 50% of the soil dataset, were randomly selected and interpolated to produce maps of the sand and clay percentages using a range of weights. The spatial average of the randomly selected training dataset was also used as an estimate of the spatial pattern (this map is equivalent to using an infinite weight). The resulting soil texture maps were compared to the remaining 50% of data not used for training, and a root

mean square error (RMSE) was calculated for each of the five split samples. The average RMSE among the five split samples is shown in Fig. 2.3a and 2.3b for each interpolation method. Overall, the RMSE is larger for the sand percentage (Fig. 2.3a) than the clay percentage (Fig. 2.3b), but the range of sand percentages is also larger than the range of clay percentages in this field. In both cases, the RMSE decreases with increasing weight, and the spatial average provides the best predictive performance of any method considered. However, the spatial average includes no spatial variation beyond the observation points, so this method is not applicable for testing the effects of runoff and residual water content on downscaled soil moisture patterns. This exercise demonstrates that the inferred spatial variations in soil texture contain significant errors despite the seemingly large number of available observations.

For each vegetation pattern, soil adjusted vegetation index (SAVI) (Huete, 1988) was calculated from Landsat 7 or 8 multispectral imagery (depending on availability of data) to represent fractional vegetation cover. Table 2.1 provides the date that was used to calculate SAVI for each vegetation pattern. Soil moisture sampling from the CRP period was conducted after the native grasses had become well established, so only one vegetation pattern, obtained from June 2018, was used for the entire CRP period. A late spring date was selected because green vegetation provides the most reflectance and therefore allows for the most accurate characterization of fractional vegetation cover from SAVI. The 30 m Landsat imagery was interpolated to 5 m to match the DEM resolution. Spline interpolation was used for consistency with the soil texture interpolation. A weight of 25 was selected to avoid overshoots and maintain smoothness as described earlier. All fractional vegetation patterns are displayed in Fig. 2.4.

Precipitation and runoff were continuously monitored at Drake Farm over the entire soil moisture monitoring period. Precipitation was measured using two weighing rain gauges near the

eastern and western boundaries of the field. Runoff was measured using a flume near the eastern boundary of the field. The associated catchment is largely comprised of the eastern portion of the Drake Farm field (Fig. 2.1). Detailed descriptions of the catchment, rainfall gauges, and flume are provided by Green and Erskine (2011). In total, 46 runoff events were measured from 2002 to 2014 throughout the WFR and transitional periods. Although several large rainfall events have occurred since the CRP native grasses became fully mature around 2015, no runoff has been measured at Drake Farm since 2014.

2.2.6 Model Application

Raw soil moisture, elevation, and soil composition data were processed to obtain appropriate EMT+VS model inputs. The spatial average soil moisture $\overline{\theta}$ was calculated as the average of all soil moisture observations on a given date. Topographic inputs elevation Z, slope S, upstream contributing area A, curvature κ, and PSRI I_p were calculated from the DEM. Soil hydraulic parameters (θ_s, $K_{s,v}$, θ_r, and the calibration bounds for γ_v and γ_h) were estimated using pedotransfer functions. However, applicability of pedotransfer functions is hindered by compatibility with available inputs and desired outputs. For consistency with past EMT+VS research, θ_s, $K_{s,v}$, and the calibration bounds for γ_v and γ_h were estimated using pedotransfer functions from Cosby et al. (1984). The method from Rawls and Brakensiek (1985) was selected to obtain residual water content θ_r because it is the only available method that requires only porosity, percentage of sand, and percentage of clay as inputs. Soil properties were estimated from various other pedotransfer schemes including neural network predictions from ROSETTA (Schaap, 2001) by first estimating additional input properties from SSURGO (Soil Survey Staff, 2018) or other sparse data from Drake Farm. These pedotransfer outputs were used in preliminary

EMT+VS model calibrations, and the pedotransfer function was found to have only a small effect on the model results.

The pre-existing EMT+VS model, EMT+VS model with runoff, and EMT+VS model with residual were all applied separately to the WFR and CRP periods. In all cases, orographic precipitation was neglected due to low topographic relief over the test region (hence, $O_F = 1$). Similarly, $\kappa_{\min}$ was set equal to -999,999 because past research has shown that the EMT+VS model consistently performs better when the soil thickness is considered spatially constant (i.e. $\kappa_{\min}$ is a large negative number) (Coleman and Niemann, 2013; Ranney et al., 2015). δ_0 was set to 20 cm based on a soil survey conducted at Drake Farm, which shows a surface soil layer depth of 20 to 30 cm. α was set to 0.26 following previous EMT+VS model applications and studies of the Priestley-Taylor assumption (Eichinger et al., 1996; Coleman and Niemann, 2013). $\overline{E_p}$ was set to 3.29 mm/day based on the site description presented in Green et al. (2011).

The remaining parameters were calibrated to maximize average Nash-Sutcliffe coefficient of efficiency (NSCE) (Nash and Sutcliffe, 1970) among all soil moisture measurement dates. Remaining parameter bounds for calibration were selected based on theoretical bounds or locally available data. For the EMT+VS model with runoff, a distinct $\overline{P_i}$ value was calibrated for each soil moisture observation date. Bounds for $\overline{P_i}$ were determined from maximum and minimum measured hourly precipitation intensity at Drake Farm from 2016 to 2018. For the cases with residual water content, a calibrated residual adjustment factor d was multiplied with θ_r in the model to allow for flexibility in the magnitude of residual water content. This approach allows the model to calibrate residual water content to zero if a residual does not improve model performance.

Table 2.2 summarizes the calibration bounds for all relevant EMT+VS model parameters (the calibrated values are discussed later).

2.3 Results and Discussion

Figure 2.5 displays the soil moisture patterns from the pre-existing EMT+VS model, the EMT+VS model with runoff, and the EMT+VS model with residual for a dry and wet date during the WFR period. Overall, spatial patterns of soil moisture during the WFR period show little spatial variation. Figure 2.5a shows the pre-existing EMT+VS model output for the dry date. This soil moisture pattern has wetter and drier patches that closely resemble the interpolated soil textural patterns (see Fig. 2.2c and 2.2d). Specifically, regions of higher clay content and lower sand content are wetter due to their lower hydraulic conductivity, which requires a larger θ for the soil to drain. Also, regions with higher sand content and lower clay content have lower porosity. A lower porosity reduces θ because unsaturated hydraulic conductivity and ET depend on θ / θ_s. Thus, when θ_s is reduced, θ must be reduced so that the outflows from the soil balance the inflow. Figure 2.5b displays the pre-existing EMT+VS model output for a wet date during the WFR period. The primary feature of this soil moisture pattern is the wet valley bottom running west to east through the middle of the region. The valley bottom is wet because it has a large upslope area and thus receives the most lateral flow. Lateral flow is more important during wetter conditions. The wet date also shows secondary effects of the soil texture patterns for the same reasons discussed with Fig. 2.5a.

The results from the EMT+VS model with runoff are shown in Fig. 2.5c and 2.5d. For the dry date, a similar pattern to Fig. 2.5a is observed, but the spatial structure has changed somewhat. When runoff is included, $K_{s,v}$ affects both the infiltration and the outflows. Thus, regions with high clay content and low sand content have both less infiltration and less drainage, and the

resulting soil moisture pattern has a weaker resemblance to the soil texture pattern. The spatial average of the infiltration function $\overline{I_F}$ is 0.99 on this date, indicating that only a small amount of runoff occurs. For the wet date, the pattern in Fig. 2.5d is similar to the pre-existing case (Fig. 2.5b) with the wet valley bottom and secondary soil effects as discussed previously. As for the dry date, $\overline{I_F}$ is 0.99, which indicates that nearly all precipitation infiltrates. The $\overline{P_i}$ values vary for the dry (216 mm/d) and wet (125 mm/d) dates (Table 2.3), but the effect of $K_{s,v}$ dominates Eqn. [2.7] the effects of runoff are nearly identical in both cases.

Fig. 2.5e shows the soil moisture pattern from the EMT+VS model with residual on the dry date during the WFR period. Comparing Fig. 2.5a and 2.5e, some small changes have occurred in the spatial structure of the soil moisture pattern. The residual adjustment factor d was calibrated to 0.56, which produces a spatial average residual water content $\overline{\theta_r}$ of 0.056. When residual is included, the soil texture pattern affects both the upper and lower bounds of θ. Thus, the soil moisture pattern still resembles the soil texture pattern, but that dependence has changed somewhat from Fig. 2.5a. In general, a larger residual reduces the spatial variation in the soil moisture pattern, but in this case only a small change is observed due to the small residual and low spatial variation in the pre-existing EMT+VS model patterns. Figure 2.5f displays the soil moisture with residual water content on the wet date. The soil moisture pattern is very similar to the pre-existing case (Fig. 2.5b) but the dependence on the soil texture has changed slightly.

Figure 2.6 presents maps of soil moisture from the pre-existing EMT+VS model, the EMT+VS model with runoff, and the EMT+VS model with residual for a wet date and dry date during the CRP period. Soil moisture patterns during the CRP period display more spatial variation than the WFR period. Figure 2.6a displays the pre-existing EMT+VS model output on a dry date. The soil moisture pattern on the dry date resembles both the current vegetation pattern (Fig. 2.4f)

and the soil texture pattern (Fig. 2.2c and 2.2d). Regions with higher fractional vegetation cover are wetter mostly due to vegetation shading the soil surface. The shading reduces soil evaporation and produces wetter conditions. The southwestern corner of the region is significantly wetter than the rest of the region (Fig. 2.6a). This wetness is a combined effect of soil and vegetation. The southwestern corner has relatively high fractional vegetation cover and very low hydraulic conductivity due to high clay percentage. The shading and reduced drainage result in an especially wet region. Figure 2.6b shows the pre-existing EMT+VS model output on the wet date. As was observed in the WFR period, the most prominent feature is the wet valley bottom. Like the dry date, the southwestern corner is the wettest portion of the region.

The soil moisture from the EMT+VS model with runoff is shown in Fig. 2.6c and 2.6d. The dry date shows a similar behavior to the pre-existing model. The pattern once again resembles the pattern of fractional vegetation cover and the southwestern corner is particularly wet. Figure 2.6d shows the wet date, which is also similar to the pre-existing model output. The valley bottom and southwestern corner are the wettest portions of the region. The spatial average infiltration function $\overline{I_F}$ is equal to 0.98 for both the wet and dry dates, again indicating that little runoff occurs. The $\overline{P_i}$ value for the dry date is 259 mm/d and for the wet date is 255 mm/d (Table 2.3), so little temporal variation in runoff occurs between the two dates.

Figure 2.6e and 2.6f show the soil moisture from the EMT+VS model with residual water content. On both the wet (Fig. 2.6e) and dry date (Fig. 2.6f), the soil moisture maps are identical to the pre-existing EMT+VS model results because the residual adjustment factor d is calibrated to zero for the CRP period. Thus, residual water content has no effect on the EMT+VS model results during the CRP period.

Table 2.2 summarizes the calibrated parameter values for the WFR and CRP periods and provides some insights into the reasons the soil moisture patterns differ between the two periods. Because all model versions for a given period display similar behavior, the three models are compared as a group between the two periods. First, the aerodynamic ET exponent β_a decreases from the WFR period to the CRP period. This change reflects a change in the moisture limitation function that estimates ET from PET. The moisture limitation function is known to depend on vegetation type and condition, so this change likely reflects the change in vegetation type (Lowry, 1959). Another parameter that changes substantially is the portion of transpiration that is derived from the modeled soil layer η. This parameter decreases from the WFR period to the CRP period, which indicates the CRP vegetation extracts less of its water from the modeled soil layer (i.e. near the ground surface). The parameter that quantifies the effect of elevation on PET ω also shows a notable change. However, due to the small topographic relief over the region, this change has little effect on the soil moisture results. The change in the fractional vegetation cover (Fig. 2.4) also contributes to the differences in soil moisture patterns. The vegetation patterns in the WFR period range from bare soil, with a spatial average fractional vegetation cover $\overline{V} = 0.09$, to mature wheat in one set of crop strips ($\overline{V} = 0.22$). The CRP period has higher fractional vegetation cover than any WFR pattern ($\overline{V} = 0.25$). The higher vegetation cover affects evaporation (via shading), transpiration, and interception and therefore influences the spatial patterns of soil moisture.

Figure 2.7a and 2.7b summarize the NSCE calculated on each application date for each model version. For purposes of interpretation, if the spatial average was directly used as a predictor of the soil moisture pattern, the NSCE value would be zero. If a downscaled pattern exactly reproduced the measured soil moisture pattern, the NSCE value would be one. Downscaled soil moisture patterns typically have NSCE values below 0.4 due to substantial errors in the soil

moisture observations relative to spatial variance (Busch et al., 2012). For the WFR period, the pre-existing EMT+VS model produces a positive NSCE value for only two of ten dates with an average NSCE of -0.023 over all dates (Fig. 2.7a). The pre-existing EMT+VS model likely has low NSCE values during this period for multiple reasons. First, the larger measurement depth used during the WFR period (30 cm) shows less spatial variation and less correlation with site characteristics than the 15 cm measurement depth used during the CRP period. The average spatial standard deviation of the measured soil moisture is 0.026 in the WFR period and 0.030 in the CRP period. However, the CRP period has dates with much higher spatial variation in soil moisture (the range in spatial standard deviation values is 0.010 for the WFR period and 0.021 for the CRP period). Second, the EMT+VS model is forced to use the spatial patterns of soil texture to infer soil hydraulic properties and thus the soil moisture. Despite the large number of observations points, the spatial variations of soil texture were shown to contain significant errors in Fig. 2.3.

Including runoff in the EMT+VS model improves the NSCE values for all dates in the WFR period except one, which has a very small decrease (Fig. 2.7a). The runoff case also has positive NSCE values for all dates except one and an average NSCE value of 0.048 over all dates. The most notable improvements are for dates with higher $\overline{\theta}$, which also tend to have measured antecedent runoff (dates with antecedent runoff are denoted with stars in Fig. 2.7a). In this study, any measured runoff event that occurred less than one month prior to soil moisture sampling is considered an antecedent runoff event due to an observed lag time between precipitation and soil moisture response at Drake Farm. Thus, another reason for the poor performance of the pre-existing model that runoff is not considered. By allowing $\overline{P_i}$ to vary temporally (Table 2.3), the revised EMT+VS model can determine the optimal magnitude of runoff on each date. Finally, the

residual case shows small improvements in NSCE on most dates. However, NSCE is still negative on eight out of the ten sampling dates, and the average NSCE over all dates is -0.019 (Fig. 2.7a).

For the CRP period, the pre-existing EMT+VS model produces positive NSCE values for all eight dates (Fig. 2.7b). In contrast to previous EMT+VS model applications (Greico et al., 2018), the model performs best under especially dry and wet conditions. The average NSCE for all dates is 0.203, which is similar to downscaling the performance at other test regions (Coleman and Niemann, 2013; Ranney et al., 2015; Cowley et al., 2017; Greico et al., 2018). The four wettest dates show notable differences in their NSCE values. The pre-existing EMT+VS model assumes equilibrium and the only variable that changes in time is $\overline{\theta}$. Thus, it neglects any hysteresis and always produces the same soil moisture pattern for a given $\overline{\theta}$. While $\overline{\theta}$ is very similar on each of those four dates, each observed soil moisture pattern depends on its unique history of wetting and drying. When runoff is included, several dates show moderate increases in NSCE (Fig. 2.7b). The average NSCE increases to 0.220. The smaller change in performance for the CRP period is consistent with lack of runoff measured at the flume during this period. Localized runoff may have occurred at various points in the field, but widespread runoff did not occur for any considered date. The EMT+VS model with residual is identical to the pre-existing EMT+VS model during the CRP period, so the NSCE values remain unchanged.

Average RMSE for each model version is shown in Fig. 2.8a and 2.8b. For the WFR period, the pre-existing model produces an average RMSE value of 0.0268 (Fig. 2.8a). This value is close to the measurement error of a TDR device (Huisman et al., 2001) and indicates that the average error of the EMT+VS model is low despite the low NSCE values. The contrast between the NSCE and RMSE values is caused by the low spatial variation in measured soil moisture over the region. The NSCE value quantifies the model's error relative to the spatial variability. When spatial

variability is low, NSCE is sensitive to small differences between measured and modeled soil moisture. When runoff is included in the model, RMSE improves slightly to 0.0258. Including residual water content in the EMT+VS model also improves the RMSE slightly (from the pre-existing model) to 0.0267.

During the CRP period, pre-existing EMT+VS model produces a RMSE value of 0.0263 (Fig. 2.8b). Thus, despite the higher NSCE value observed for the CRP period, RMSE is only slightly smaller for the CRP period. When runoff is included in the model, RMSE again shows a slight decrease to 0.0261. Thus, the small improvement in NSCE values produces only a small improvement in the RMSE values. The EMT+VS model with residual water content is identical to the pre-existing EMT+VS model during the CRP period, so the RMSE is the same as the pre-existing model performance.

Performance of the EMT+VS model versions was also evaluated by calibrating the models with a subset of the soil moisture dataset and then evaluating performance using the data that was withheld from the calibration. For each land management period, one date was withheld from calibration and the model was evaluated for the withheld date. This process was repeated until each date was withheld from the calibration. When the model was applied to the withheld date, the average value of $\overline{P_i}$ from the calibration period was used.

For the WFR period, the pre-existing EMT+VS model, the EMT+VS model with runoff, and the EMT+VS model with residual produce average NSCE values of -0.054, -0.052, and -0.058, respectively, for the dates withheld from the calibration. These NSCE values are lower than when all dates were used for calibration, and a smaller improvement in performance is observed when runoff is included. The average RMSE value for the dates withheld from calibration is 0.041 for all three models, which is higher than the RMSE values when the full dataset is considered. For

the CRP period, the preexisting, runoff, and residual water content versions of the model produce average NSCE values of 0.184, 0.179, and 0.184, respectively, for the dates withheld from the calibration. The withheld date produces RMSE values of 0.030, 0.031, and 0.030 for the pre-existing EMT+VS model, the model with runoff, and the model with residual, respectively. Again, NSCE is lower and RMSE is higher than the previously discussed calibrations, and performance is relatively unchanged by model additions. However, these results indicate that including runoff in the EMT+VS model is only successful when a date-specific $\overline{P_i}$ is used. Additionally, residual water content was calibrated to be zero or close to zero in all cases and therefore also has a negligible impact on EMT+VS performance in these cases.

A full generalized model containing both runoff and residual water content was also considered. The WFR and CRP periods both show similar results to the separately-calibrated models. For the WFR period, daily values of $\overline{P_i}$ are more similar to one another than the separately-calibrated runoff model and most values are close to 100 mm/d. Residual adjustment factor d is calibrated to 0.60 and the full generalized model produces an average daily NSCE of 0.01. The full generalized model from the CRP period is identical to the EMT+VS model with runoff, because d is calibrated to zero. The average NSCE is again 0.220.

The three EMT+VS model version were also compared at multiple other application regions. The models were applied at the Tarrawarra (Western and Grayson, 1998), Nerrigundah (Walker et al., 2001), and Cache la Poudre (Ranney et al, 2015) catchments. All three catchment have been used for EMT+VS model downscaling in the past (Coleman and Niemann, 2013; Ranney et al., 2015). These additional catchments produce similar results to Drake Farm. The EMT+VS model with runoff causes slight improvements in model performance with respect to NSCE and RMSE at Tarrawarra and Nerrigundah as well as minor changes in spatial patterns of

soil moisture. At Cache la Poudre, I_F is equal to one over the entire region, so including runoff does not affect EMT+VS results. At all three regions, d is calibrated to zero and therefore residual water content has no impact on EMT+VS downscaling.

2.4 Conclusion

This study implemented runoff and residual water content into the EMT+VS soil moisture downscaling model. Runoff was included by allowing temporally varying precipitation intensity and estimating the soil's infiltration capacity using the vertical saturated hydraulic conductivity. This infiltration capacity can be derived from the Green-Ampt (1911) model if gravity dominates the vertical hydraulic gradient. Residual water content was included by assuming that all hydrologic fluxes cease when soil moisture is at or below residual water content. The EMT+VS model was applied to a new test region (Drake Farm), which was managed in a wheat-fallow rotation for many years and then placed in a Conservation Reserve Program. The impact of these model additions on the fine scale soil moisture patterns and model performance was examined.

Runoff was found to have only small effects on the calibrated model's soil moisture patterns for both the WFR and CRP periods. Including runoff decreases the soil moisture at locations with greater fine-grained content. Fine-grained soil has lower saturated hydraulic conductivity, which reduces the infiltration capacity. The lower infiltration capacity induces more runoff and produces drier soil after the storm. Including runoff produces only small increases in model performance as measured by NSCE and RMSE for both periods. A greater increase in model performance occurs for the WFR period when runoff was observed at a flume near the edge of the field.

Residual water content was also found to have small effects on the calibrated model's soil moisture patterns for both management periods. In general, increasing residual water content

decreases the spatial variation in the fine resolution soil moisture patterns. Residual water content reduces the range of soil moisture over which hydrologic processes occur in the soil. Thus, when residual is included, smaller variations in moisture are sufficient to balance the inflows and outflows in the soil. For the WFR period, the calibrated residual water content is non-zero, but the improvement in performance is very small. For the CRP period, residual water content was calibrated to zero and therefore had no effect on the soil moisture downscaling.

Runoff and residual water content provide small improvements in model performance partly because the soil moisture variations that they induce depend on soil texture variations. Soil texture observations at 215 locations were used in a spline interpolation method to determine the gridded soil texture patterns, but the spatial average sand and clay percentages were found to better estimate the soil texture than the interpolated patterns. Thus, the variations in soil moisture that runoff and residual water content produce in the model are likely poor estimates of the real soil moisture variations from those mechanisms.

The small improvements in performance may also occur because Drake Farm has relatively small spatial variations in soil moisture. Thus, much of the observed spatial variation is likely measurement error and cannot be reproduced by any model. The low spatial variation in moisture causes the NSCE values for the WFR period to be near zero even though RMSE values are similar to typical measurement errors.

Overall, the results support neglecting runoff and residual water content in soil moisture downscaling. However, the impacts of runoff and residual water content on the EMT+VS model results should be assessed at additional application regions that span a variety of topographic, vegetation, and soil conditions. Regions with frequent and substantial runoff would be of particular interest. Runoff could have a greater effect on soil moisture patterns and show greater

improvements in downscaling performance if runoff is more common. Additionally, regions where residual water content has been studied and is significant should be examined. Finally, the effects of runoff and residual water content on EMT+VS model downscaling should be assessed for a case in which more reliable soil data are available. A region with measured soil texture in every downscaling grid cell or where soil interpolation is shown to be more accurate should be examined. More accurate soil data may also result in improved performance when runoff and residual are considered. Although various other test sites considered in this study produced results similar to Drake Farm, none contain substantial runoff over the soil moisture sampling period or more reliable soil data than Drake Farm, and therefore these conditions are of interest to future EMT+VS model investigation.

2.5 Tables and Figures

Table 2.1. Vegetation patterns used in Drake Farm EMT+VS analyses. The east management strips begin on the eastern side of the field and alternate with the west management strips. Asterisks indicate dates for which antecedent runoff was measured at the field outlet within 1 month of the soil moisture observations.

Management Period	Vegetation Cover	Landsat Date	Associated Soil Moisture Dates
WFR	Failing wheat in east management strips	16 April 2003	7 May 2003*
	Wheat in west management strips	29 June 2004	24 June 2004
	Wheat in east management strips	24 June 2005	19 October 2004, 17 June 2005*, 24 May 2007
	Full site bare	27 August 2005	10 August 2005*, 31 July 2007*
	Barley on eastern side, corn on western side	27 June 2009	17 June 2009*, 26 June 2009*, 1 July 2009*
CRP	Native grasses and invasive weeds	4 June 2018	5 May 2016, 24 June 2016, 5 October 2016, 13 October 2016, 18 April 2017, 26 April 2017, 25 May 2017, 22 May 2018

Table 2.2. EMT+VS parameter bounds and calibrated values for Drake Farm. All parameters shown are dimensionless

Parameter	Lower Bound	Upper Bound	WFR			CRP		
			Pre-Existing EMT+VS	EMT+VS with Runoff	EMT+VS with Residual	Pre-Existing EMT+VS	EMT+VS with Runoff	EMT+VS with Residual
ω	0	0.01	0.001	0.0003	0.002	0.008	0.008	0.008
β_r	0.2	5	4.90	4.94	4.95	4.86	4.36	4.86
β_a	0.2	5	0.60	0.37	0.76	0.21	0.21	0.21
λ	0	1	0.70	0.64	0.78	0.79	0.73	0.79
η	0	1	0.78	0.58	0.82	0.36	0.16	0.36
μ	1	3	1.92	1.26	2.26	1.77	1.77	1.77
ι	0	100	30.5	12.2	32.2	48.7	8.39	48.7
γ_v	13.5	20.8	19.8	18.9	17.3	19.7	14.1	19.7
γ_h	1	20.8	4.00	2.95	4.24	3.99	2.97	3.99
ε	1	3	1.50	1.55	1.28	1.28	1.07	1.28
d	0	1	-	-	0.56	-	-	0

Table 2.3. Calibrated spatial-average storm intensities for each measurement date. Upper and lower calibration bounds are 6.10 mm/d and 793 mm/d, respectively.

WFR Period			CRP Period		
Date	$\overline{\theta}$	$\overline{P_i}$ (mm/d)	Date	$\overline{\theta}$	$\overline{P_i}$ (mm/d)
7 May 2003	0.210	235	5 May 2016	0.216	255
24 June 2004	0.236	254	24 June 2016	0.112	259
19 October 2004	0.217	251	5 October 2016	0.085	232
17 June 2005	0.242	132	13 October 2016	0.117	186
10 August 2005	0.154	125	18 April 2017	0.125	180
24 May 2007	0.146	216	26 April 2017	0.208	198
31 July 2007	0.219	159	25 May 2017	0.204	101
17 June 2009	0.226	234	22 May 2018	0.205	190
26 June 2009	0.235	247	-	-	-
1 July 2009	0.228	226	-	-	-

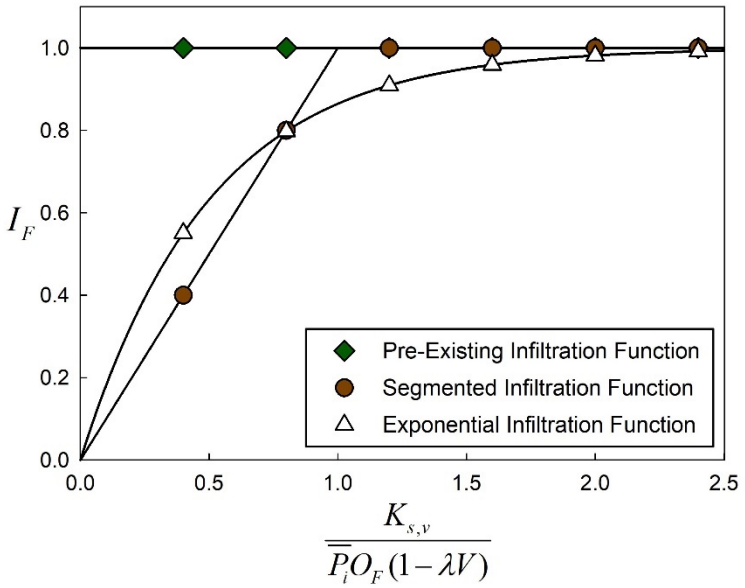

Fig. 2.1. Comparison of the pre-existing EMT+VS model's infiltration function, the segmented infiltration function, and the exponential infiltration function with $\upsilon_r = 2$

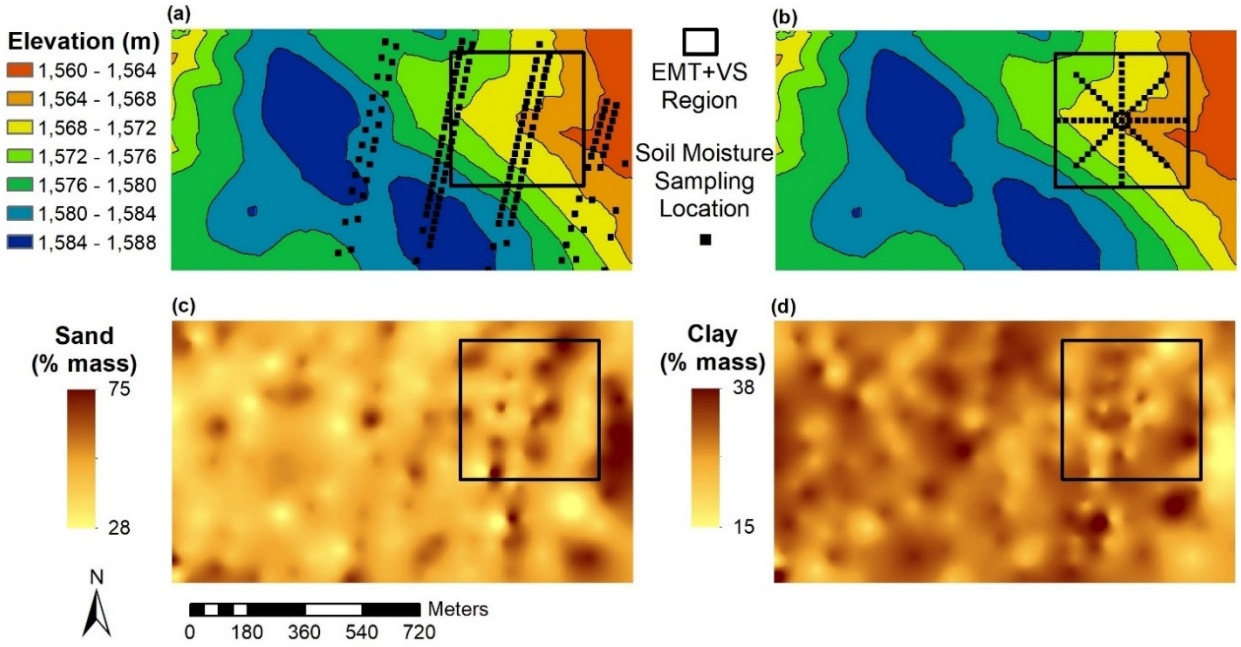

Fig. 2.2. Drake Farm topography, soil moisture observation locations, and soil composition including: (a) topography with WFR soil moisture measurement locations on 24 June 2004, (b) topography with CRP soil moisture measurement locations (consistent for all CRP dates), (c) interpolated pattern of sand percentage, and (d) interpolated pattern of clay percentage. Black squares denote the region of all EMT+VS analyses in this study.

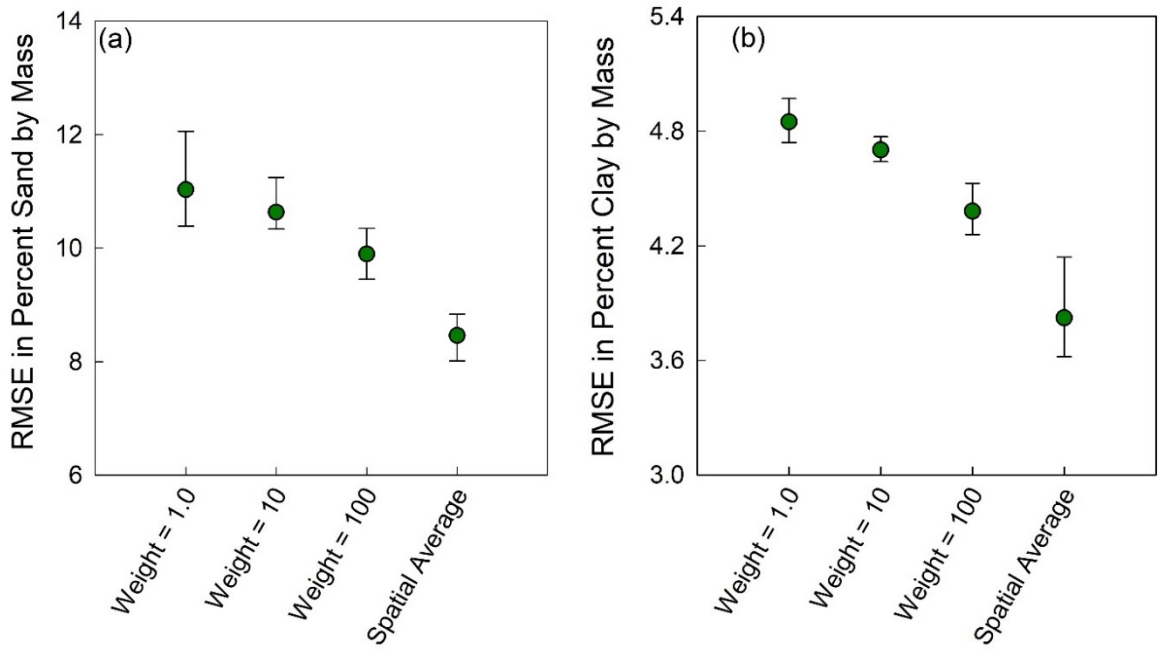

Fig. 2.3. Split sample evaluation of interpolated maps of (a) sand and (b) clay percentages. Dots represent average RMSE among five randomly selected split sample tests where 50% of data was used for training and 50% of data was used for evaluation. Error bars denote maximum and minimum RMSE among the five tests. The weight parameter is dimensionless.

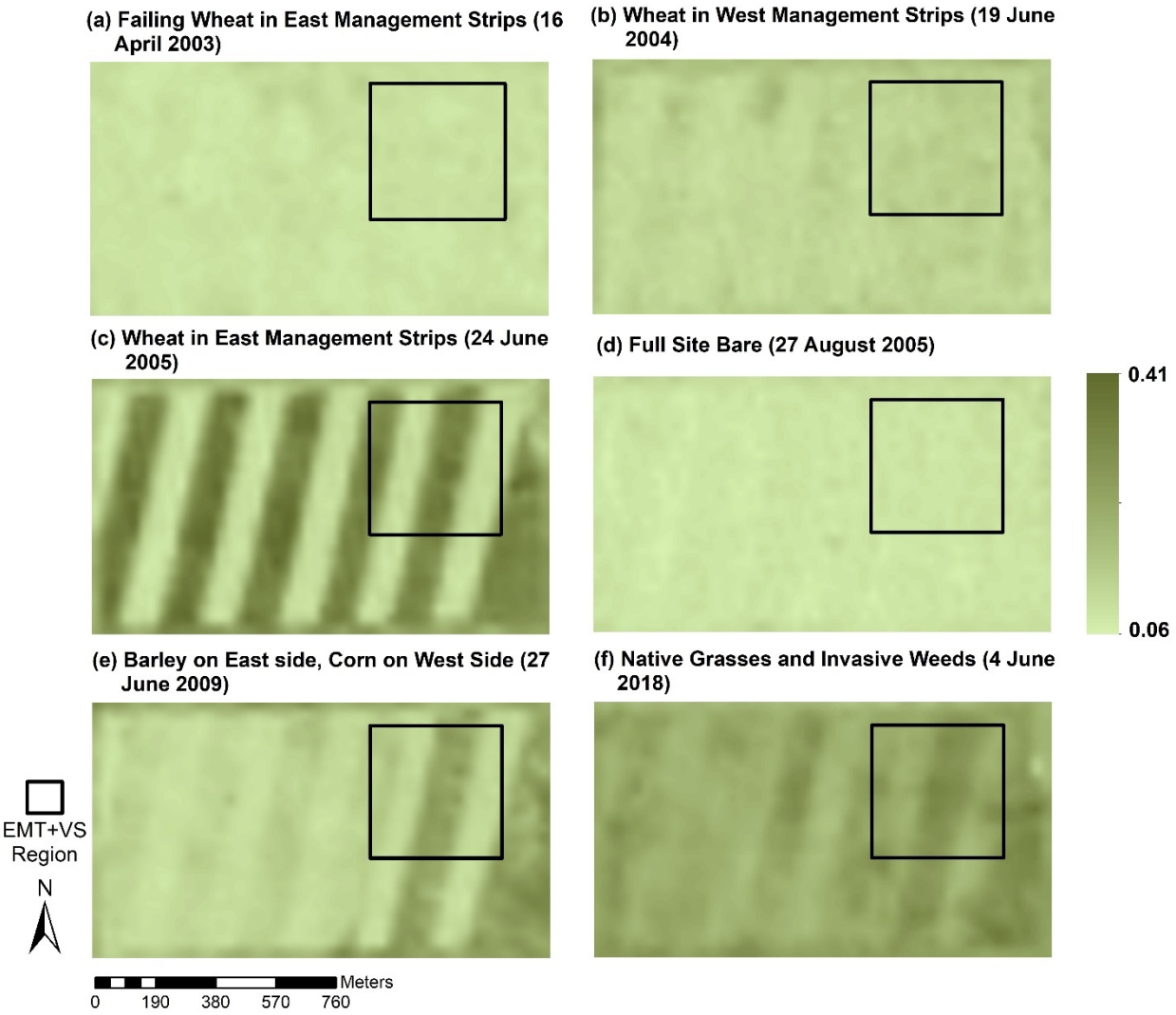

Fig. 2.4. Drake Farm fractional vegetation cover patterns estimated as SAVI from Landsat imagery including: (a) failing wheat in east management strips, (b) wheat in west management strips, (c) wheat in east management strips, (d) full site bare, (e) barley and corn, and (f) CRP with native grasses, shrubs, and invasive weeds. Note that the east management strips begin on the eastern edge of the site and alternate with west management strips. East management strips are strips with higher fractional vegetation cover in (c). Dates of Landsat imagery included in labels.

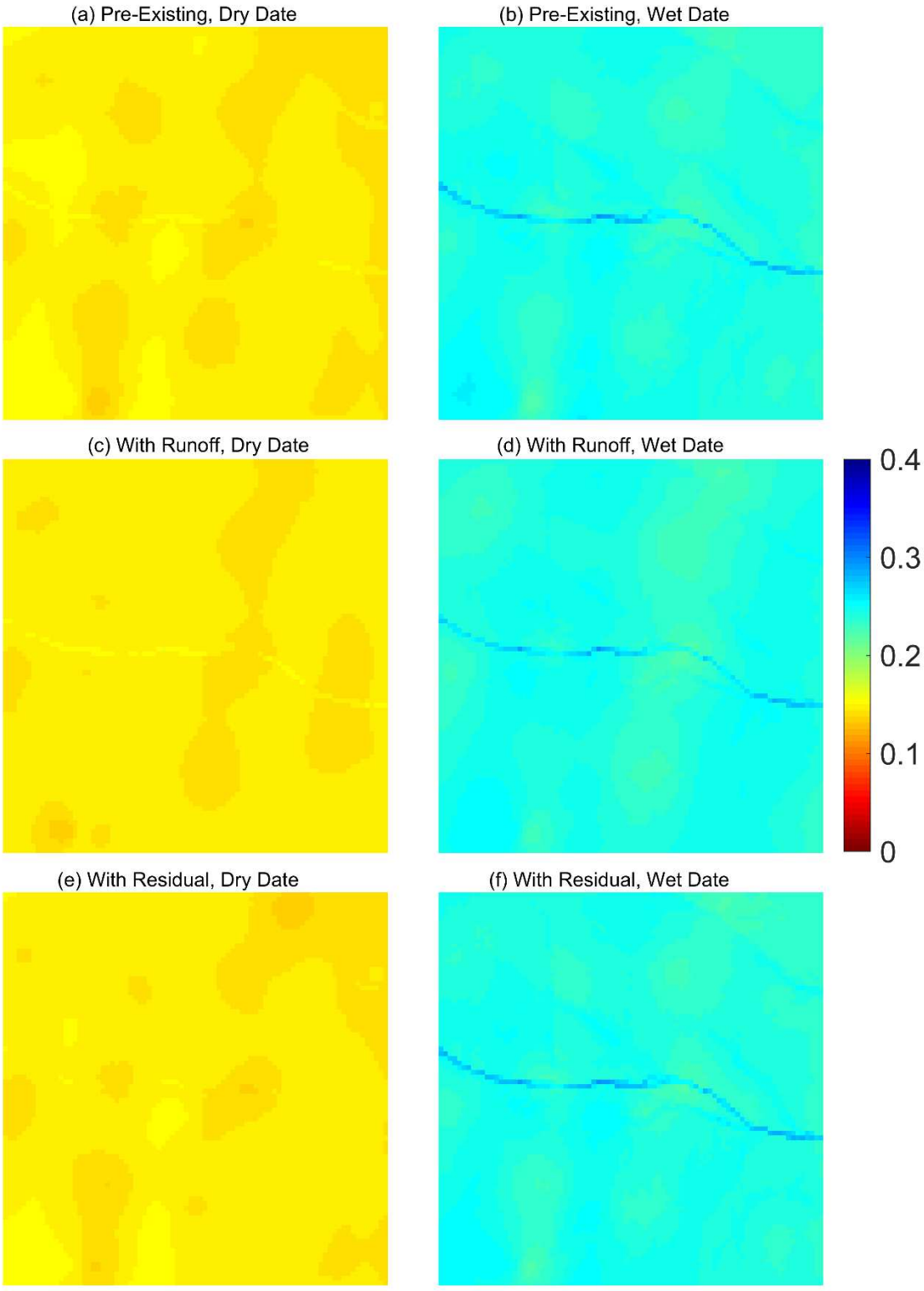

Fig. 2.5. Spatial patterns of soil moisture from the EMT+VS model for the WFR period. The dry date is 24 May 2007 ($\overline{\theta} = 0.146$) and the wet date is 17 June 2005 ($\overline{\theta} = 0.242$).

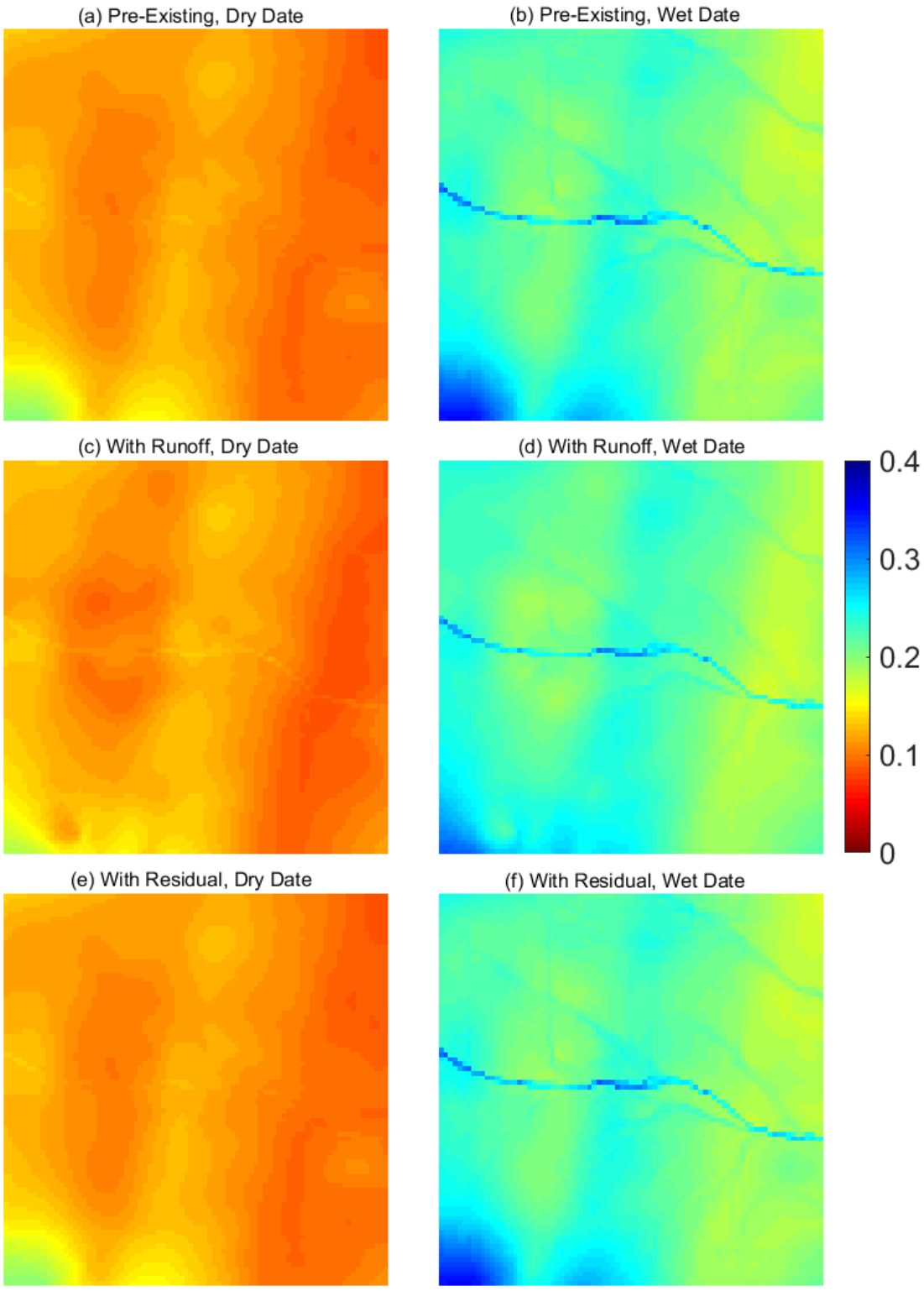

Fig. 2.6. Spatial patterns of soil moisture from the EMT+VS model for the CRP period. The dry date is 24 June 2016 ($\overline{\theta} = 0.112$) and the wet date is from 05 May 2016 ($\overline{\theta} = 0.216$)

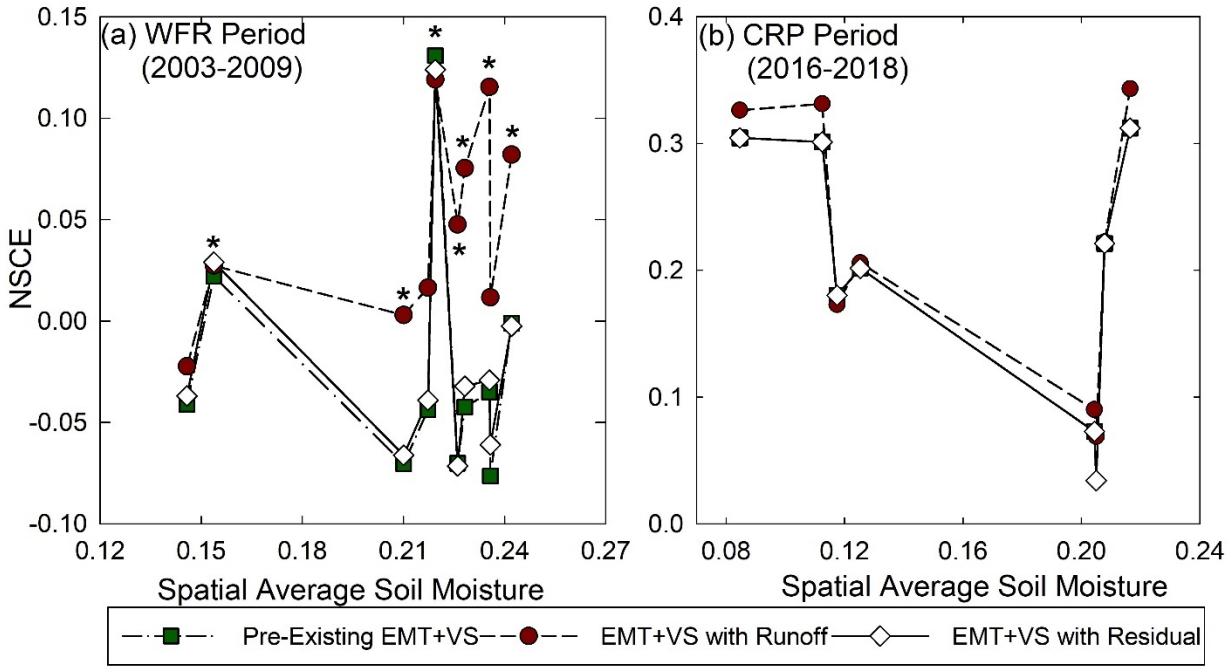

Fig. 2.7. EMT+VS model daily NSCE for (a) WFR period and (b) CRP period. Stars in (a) denote dates with observed runoff at the field outlet. No such stars are shown in (b) because no runoff was observed over the measurement period.

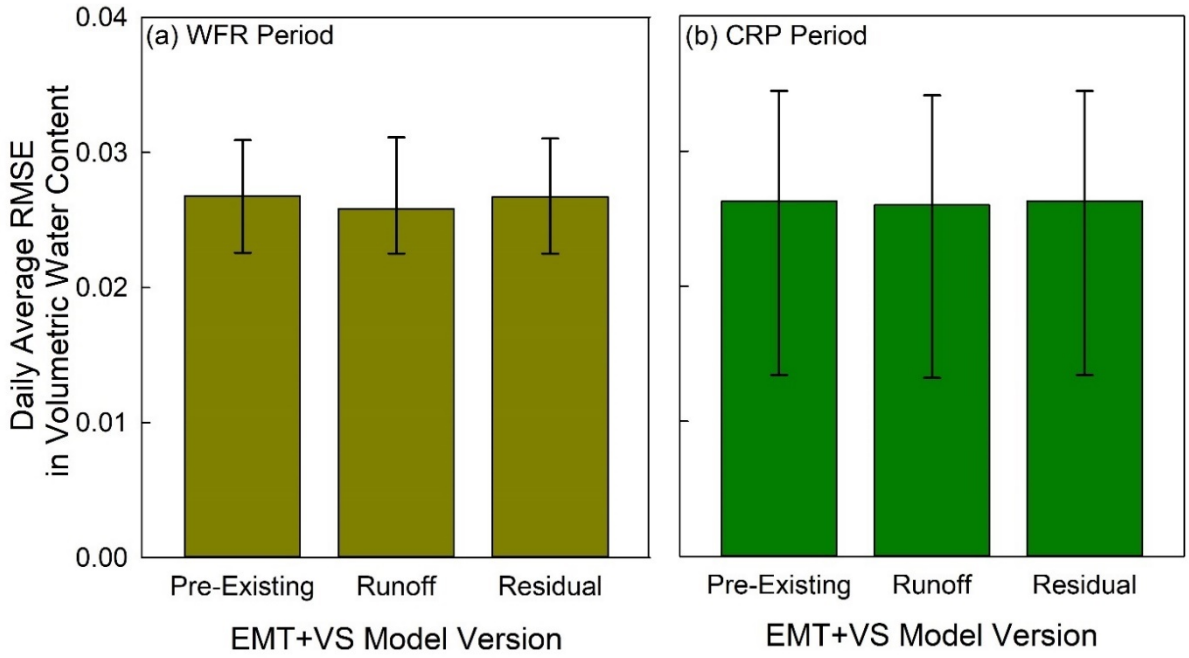

Fig. 2.8. EMT+VS model average RMSE over all sampling dates (see Fig. 2.7) for (a) WFR period and (b) CRP period. Error bars denote minimum and maximum daily RMSE for each model.

3. STRESS MODEL DEVELOPMENT

3.1 Introduction

Assessing vehicle mobility across natural terrain requires knowledge of the traversed soil strength. The strength of surficial soils is controlled by several constitutive properties, including texture (percentage of sand, silt, and clay), density, and water content. Water in soil pores can develop either positive or negative pressure depending on soil water content, external loading, and drainage conditions, and these pressures can either increase or decrease soil strength. The concept of effective stress is used to account for the effects of soil pore water on shear strength and deformation (Terzaghi, 1925; 1936). However, effective stress is generally neglected in terramechanics analyses based on simplifying assumptions (Reece, 1964), or empirical relationships are used to implicitly incorporate effective stress (e.g., Smith and Meyer, 1973). However, the contribution of soil pore water on the soil strength parameters of unsaturated soils (soils with water contents less than saturation) is critical to developing models to assess the effect of variation in soil moisture on soil strength (Bishop and Blight, 1963; Fredlund et al., 1978; Lu and Likos, 2004; Lu et al., 2010) in terramechanics mobility models.

In-situ testing methods are preferred in terramechanics to determine near-surface soil properties. The soil depth relevant to terramechanics applications (i.e. critical depth) can vary based on soil type, water content, density, and dimensions of the tire or track contacting the soil because the shear stress distribution below the tire or track depends on these variables. The critical depth can vary from the surficial layer (between 0 and 15 cm) to a depth of 60 cm. In most soils, the critical soil layer is the surficial layer, and terramechanics strength measurement methods are typically conducted on the surficial soils to classify the behavior of this critical layer (Wong, 2010).

Two in-situ methods are widely used to quantify surface soil strength: rating cone index (RCI) and the Bekker soil strength framework. Rating cone index (RCI) is measured by pushing a circular cone into the soil (Knight, 1956). Force required to insert the cone into soil is divided by the area of the cone to produce the cone index (CI) of the specific measured soil. Cone index is calculated in pounds-per-square-inch (psi) but presented as a dimensionless value. For fine-grained soils, a remolding index (RI) is multiplied by CI to produce RCI. For coarse-grained soils, no RI is necessary and the term RCI is used interchangeably with CI. The RCI is compared to an empirically determined vehicle cone index (VCI) for a specific vehicle to determine if soil is trafficable on a go/no-go basis. The RCI method provides a single quantity to characterize soil trafficability, which according to Bekker (1956) depends on two primary aspects of soil behavior: stability (shear strength) and elasticity (compressibility).

The RCI framework has been used in development of terramechanics databases for decades and therefore is the state-of-practice for the U.S. Army and NATO in mobility modeling. The RCI method is preferred to the Bekker method for simplicity and historic use in military applications (Rula and Nuttall, 1971). However, in many military mobility applications, even the simple RCI measurement method can be too expensive, labor-intensive, or dangerous for extensive field measurement. For scenarios in which soil strength cannot be directly measured, RCI must be estimated as a function of basic soil properties and soil moisture. The U.S. Army has developed several models to predict soil moisture and soil strength (Smith and Meyer, 1973; Sullivan et al., 1997; Mason et al., 2001; Frankenstein and Koenig., 2004). Each model relies on some variation of a simple water budget framework to estimate soil moisture. In each model, the water budget soil moisture estimates are applied to simple RCI predictive functions from Smith and Meyer

(1973) to calculate RCI as a function of soil moisture and Unified Soil Classification System (USCS) classification.

Although RCI has been the preferred soil strength framework of the U.S. Army and NATO over several decades, the Bekker soil strength framework has received increased interest in recent years (McCullough et al., 2017). Numerical models incorporating Bekker parameters as inputs (Choi et al., 2018) are increasingly used to predict speed-made-good and other trafficability metrics. Additionally, Williams et al. (2017) analyzed relationships between CI and several variables related to vehicle performance and showed poor correlations in many cases, indicating that CI is often not suitable for predicting soil strength for vehicle mobility.

The Bekker method characterizes shear strength and compressibility using a bevameter (Bekker, 1956; 1960), measuring compressibility using a pressure-sinkage test and shear strength with a torsional ring interpreted with a Mohr-Coulomb failure envelope (Coulomb, 1776; Mohr, 1900). This method lacks a simple metric to determine trafficability (such as the RCI-VCI comparison) but provides a more unique description of soil behavior for input into physics-based models (Choi et al., 2018) because shear strength and compressibility are considered separately. Shear strength is also further partitioned into frictional (exterior stress dependent) and cohesive (exterior stress independent) strength components. The two-fold parameterization of shear strength holds the advantage of incorporation into complex terramechanics numerical models. Despite the advantages of the Bekker method, no model framework exists to predict Bekker parameters from basic soil properties for scenarios in which direct sampling is not an option.

The objective of this study is to develop and evaluate a model framework for prediction of Bekker shear strength parameters as a function of soil moisture and soil texture. The resulting framework is termed the Strength of Surface Soils (STRESS) model. The STRESS model applies

soil moisture estimates from an existing soil moisture downscaling model, the Equilibrium Moisture from Topography, Vegetation, and Soil (EMT+VS) model (Coleman and Niemann, 2013; Ranney et al., 2015) and uses unsaturated soil mechanics to estimate surficial soil strength. The predictive performance of the STRESS model is evaluated using a bevameter shear device at a field site in northeastern Colorado.

3.2 Background

Bekker soil shear strength theory is based on the Mohr-Coulomb failure criterion (Coulomb, 1776; Mohr, 1900), illustrated in Fig. 3.1. The Mohr-Coulomb equation is typically presented as:

$$\tau_f = c + \sigma_f \tan\phi \tag{3.1}$$

where τ_f is shear stress at failure (i.e. shear strength), c is cohesion, σ_f is normal stress on the failure plane, and ϕ is friction angle. Shear strength of a soil is a function of applied normal stress and two soil properties: cohesion and friction angle. In soil, cohesion quantifies the shear strength effect of electrostatic interparticle forces and is independent of applied normal stress (y-intercept in Fig. 3.1). Friction angle describes shear resistance due to interparticle friction and is the arctangent of the slope of the linear-fit line in Fig. 3.1. Cohesion and friction angle are fit from experimental data by measuring shear strength at failure at multiple normal stresses and determining the optimal linear fit for Eqn. [3.1]. The true failure envelope of soils has been shown to be nonlinear, with considerable variation between friction angles measured near the origin and those measured at high normal stresses (Penman, 1953; Bishop et al., 1965; Atkinson and Farrar, 1985; Day and Axten, 1989). As shown in Fig. 3.1, the Mohr-Coulomb equation is generally fit to an intermediate portion of the nonlinear Mohr-Coulomb failure envelope and used assuming linear behavior for all relevant stress conditions. Note that Eqn. [3.1] defines the Mohr-Coulomb failure

envelope in terms of total stress σ, which is defined as the normal stress applied to soil via external loading and weight of overlying soil.

Effective stress (Terzaghi, 1925; 1936) accounts for the effects of pore water pressure on soil deformation and shear strength. Khalili et al. (2004) describe effective stress as a concept that "converts a multiphase, multistress porous medium to a mechanically equivalent, single-phase, single-stress state continuum", which allows for "application of the principles of continuum solid mechanics to fluid-filled deformable porous media". Effective stress σ' is calculated by adjusting total stress to account for pore water pressure u_w in saturated soil:

$$\sigma' = \sigma - u_w \tag{3.2}$$

Note that pore water pressure and pore air pressure discussed in this study are gage pressure. Effective stress is based on the concept that pore water pressure reduces or increases interparticle normal stress and therefore reduces or increases stress-dependent frictional shear resistance. The Mohr-Coulomb equation is updated to account for effective stress and an alternative pair of shear strength parameters are defined: effective cohesion c' and effective friction angle ϕ'. The effective stress shear strength parameters are measured in a saturated state taking into account soil pore water pressure and are assumed to be constant material properties for a given soil in geotechnical engineering practice (Terzaghi et al., 1996).

Effective stress is traditionally used in analysis of saturated soil (Terzaghi et al., 1996), and measurement of pore water pressure in saturated soil is relatively straightforward. Characterizing effective stress in unsaturated soil is more complex. Matric suction is the cumulative effect of capillarity, surface tension, and surface adsorption of pore water in an unsaturated soil and manifests as negative, or tensile, pressure in soil pore water. The effect of matric suction on effective stress and therefore soil strength must be characterized to conduct effective stress analysis

in unsaturated soil. In general, matric suction increases effective stress and soil strength, but this relationship is complex. Reece (1964) describes the decision to neglect effects of pore water pressure and matric suction in terramechanics, citing assumptions of fully drained behavior ($u_w = 0$) in coarse-grained soil or fully undrained behavior ($\sigma' = 0$) in fine-grained soil that remove the need for effective stress and simplify soil strength analysis. However, in neglecting effective stress, the soil-air-water system is grossly and unrealistically oversimplified in soils with water contents between saturation and dry. Therefore, Bekker shear strength parameters are total stress strength parameters that vary with respect to water content (Bekker, 1956; Dwyer et al., 1974; Wong, 1980) and must be treated as empirical (water content specific) parameters.

Multiple models have been introduced to incorporate effective stress in unsaturated soil and better conceptualize unsaturated strength and deformation. Bishop's method (Bishop, 1959; Bishop and Blight, 1963) calculates effective stress as a function of matric suction:

$$\sigma' = \left(\sigma - u_a\right) + \chi\left(u_a - u_w\right) \tag{3.3}$$

where u_a is pore air pressure and the difference between pore air pressure and pore water pressure $\left(u_a - u_w\right)$ is matric suction. The quantity $\left(\sigma - u_a\right)$ is net normal stress. Bishop's χ parameter defines the contribution of matric suction to effective stress. Application of Bishop's method has been shown to be problematic due to theoretical and experimental difficulties in determining Bishop's parameter (Jennings and Burland, 1962). The second method of incorporating effective stress into unsaturated soil analysis is suction stress. Suction stress was first introduced by Lu and Likos (2004) as "the net interparticle force generated within a matrix of unsaturated granular particles due to the combined effects of negative pore water pressure and surface tension". Lu and Likos (2006) later generalized the definition to also include van der Waals forces and double layer

forces. Lu et al. (2010) introduced the first closed form equation for effective stress in unsaturated soil with a method of estimating suction stress:

$$\sigma' = \left(\sigma - u_a\right) - \sigma^s \tag{3.4}$$

where σ^s is suction stress and is estimated as:

$$\sigma^s = -\frac{S_e}{\alpha}\left[S_e^{\frac{n}{1-n}} - 1\right]^{\frac{1}{n}} \tag{3.5}$$

The term S_e is effective saturation and is calculated as $S_e = \left(\theta - \theta_r\right)/\left(\theta_s - \theta_r\right)$. The variable θ is volumetric water content and the parameters α, n, θ_r, and θ_s, cumulatively referred to as van Genuchten water retention parameters (van Genuchten, 1980), are approximately the inverse of air entry pressure, pore size distribution index, residual water content, and porosity, respectively. Equation [3.5] can be rewritten as:

$$\sigma^s = -S_e\left(u_a - u_w\right) \tag{3.6}$$

The suction stress method (Eqn. [3.5] and [3.6]) is equivalent to Bishop's method if Bishop's parameter is assumed to be equal to effective saturation. The assumption $\chi = S_e$ is commonly used to estimate Bishop's parameter and was considered by Bishop and Blight (1963). Vanapalli and Fredlund (2000) showed that this estimate of Bishop's parameter performs well in the range of suction from 0 kPa to 1500 kPa but performs poorly over a greater range of suction. Various other methods have been introduced to estimate Bishop's parameter as a function of matric suction. Khalili and Khabbaz (1998) introduced a unique relationship between Bishop's parameter and the suction ratio $\left(u_a - u_w\right)/\left(u_a - u_w\right)_b$, where $\left(u_a - u_w\right)_b$ is the air entry suction of a soil. This method was found to perform well under the set of laboratory conditions used in the study.

Fredlund et al. (1978) developed a model for evaluating shear strength of unsaturated soil by altering the Mohr-Coulomb formula rather than extending the effective stress equation. The effects of net normal stress and matric suction on shear strength are considered separately and a friction angle with respect to matric suction ϕ^b is introduced in addition to the traditional effective stress friction angle:

$$\tau_f = c' + (\sigma - u_a)\tan\phi' + (u_a - u_w)\tan\phi^b \tag{3.7}$$

The Fredlund method is theoretically robust and evaluates shear strength with respect to two nonmaterial stress state variables (net normal stress and matric suction). In comparing the Bishop, Fredlund, and Lu methods, concerns arise with the Bishop or Lu methods described previously when the Bishop or Lu methods use degree of saturation to describe the stress state of the soil. Fredlund et al. (2012) argued that degree of saturation, a material variable, cannot be used to describe the stress state of a soil because stress state variables are traditionally independent of material properties. Lu and Likos (2004) offered a counterpoint to this argument, presenting the justification that state variables "are those that are required to completely describe a system for the phenomenon at hand", and in unsaturated soil, material variables that describe the relative quantity of each phase (soil, water, air) are necessary to completely define the system. While traditional application dictates that stress state variables should be independent of material variables, the fundamental definition of a stress state variable does not inherently preclude the use of material variables to describe stress state phenomena. Further, the Fredlund method does not avoid the complexities involved in accounting for the effects of matric suction on soil strength, as the new friction angle with respect to matric suction (a material variable) is defined to describe the relationship between matric suction and shear strength. The three methods, while distinct in their theoretical underpinnings and parameterizations, are numerically equivalent in quantitative

descriptions of unsaturated soil behavior when degree of saturation is used as a proxy for reduction in moisture derived soil strength with decreasing water content. However, while the Lu method relies on van Genuchten soil parameters for which pedotransfer functions from soil texture data are readily available, the Fredlund method introduces a new parameter that is difficult to estimate from soil compositional data and is not consistent with traditional Terzaghi effective stress. Therefore, only the Lu method is considered in this study.

3.3 Methods and Materials

3.3.1 STRESS Model Development

A conceptual diagram of the STRESS model procedure is shown in Fig. 3.2. The STRESS model is designed to output soil shear strength parameters as a function of soil moisture and texture. The shear strength parameters estimated by the model are equivalent to Bekker total stress strength parameters but are estimated by accounting for effects of variable soil moisture. The STRESS model is paired with the EMT+VS model, a soil moisture downscaling model (Coleman and Niemann, 2013; Ranney et al., 2015). The EMT+VS model downscales coarse-resolution (1-60 km grid cell) soil moisture using fine-resolution (10-30 m) topographic, vegetation, and soil data to produce fine-resolution (10-30m) estimates of soil moisture. The EMT+VS model simulates an equilibrium water balance over the hydrologically active soil layer, which is defined as the surface soil layer over which most lateral flow occurs. The STRESS model is developed to use EMT+VS soil moisture outputs as input for moisture-variable soil strength estimation, but the STRESS model can also be applied independently from the EMT+VS model with measured soil moisture data. Soil textural data (percentage by mass of sand and clay) are obtained from international or local soil databases such as ISRIC-WISE (Batjes, 2016) or SSURGO (Soil Survey Staff, 2018). If available, soil texture can also be input from local measured values.

The STRESS model applies the Lu method (Lu et al., 2010) to estimate terramechanics strength parameters. Effective friction angle is constant over the full range of water content from zero to saturation (Fredlund et al., 1978). Therefore, STRESS estimates a constant friction angle for all moisture conditions. The cohesion value for an unsaturated soil measured by a bevameter captures soil strength contributions from electrostatic forces between soil particles (effective cohesion) and effects of pore water (apparent cohesion). The STRESS model reproduces Bekker cohesion by combining effective and apparent cohesion to produce a parameter termed moisture-variable cohesion c_θ.

The STRESS model outputs use empirical relationships to first estimate effective stress strength parameters and van Genuchten's water retention parameters (van Genuchten, 1980). Existing data relating effective stress strength parameters to soil texture are limited, particularly in a terramechanics (near surface) setting. In the STRESS model procedure, United States Department of Agriculture (USDA) soil classification is determined from percentages of sand and clay and an empirical conversion from USDA to USCS classification from Garcia-Gaines and Frankenstein (2015) is used to estimate USCS classification. Effective stress strength parameters are estimated as USCS class average values from the United States Naval Facilities Engineering Command (NAVFAC) Foundations and Earth Structures Design Manual (1986) and the USDA Transportation Engineering Manual (1981). Table 3.1 summarizes various class average effective strength parameters and those selected for use in the STRESS model. The justification for class-average parameter used in the STRESS model is also provided in Table 3.1.

The predictive performance of the STRESS model is limited by the generality of these binned parameters. However, the STRESS model is designed to be improved as data is compiled to better characterize texture-moisture-strength relationships in soil and allow for better prediction

of effective shear strength parameters using basic soil data. As a dataset is compiled to relate soil texture to effective shear strength parameters, continuous relationships may be developed to overcome these binning errors, and the predictive capabilities of the STRESS model will likely improve.

Many pedotransfer schemes exist to predict van Genuchten soil water retention parameters as a function of basic soil data. However, applicability of pedotransfer functions is hindered by compatibility with available inputs and desired outputs. For consistency with EMT+VS model development (Ranney et al., 2015), the pedotransfer function from Cosby et al. (1984) is used to estimate porosity using percentage of sand and clay as input. Then, sand and clay percentages are used along with Cosby et al. (1984) porosity as input into the pedotransfer scheme from Rawls and Brakensiek (1984) to estimate the remaining parameters: θ_r, α, and n. Note that the van Genuchten pedotransfer functions used in this study were developed for agriculture applications. Additionally, a site-specific residual adjustment factor d may be calibrated within the EMT+VS model to adjust the magnitude of residual water content to best fit measured soil moisture data; when available, this parameter is also incorporated in the STRESS model.

The STRESS model outputs are determined by combining the estimated effective stress strength parameters with unsaturated soil strength theory. Because effective friction angle is constant with respect to soil moisture (Fredlund et al., 1978), output effective friction angle from STRESS is equal to the class-average effective friction angle from Table 3.1. Moisture-variable cohesion combines effective cohesion from Table 3.1 with a contribution of matric suction to suction stress based on Lu et al. (2010). Applying the closed-form equation for effective stress from Lu et al. (2010) to the effective stress Mohr-Coulomb formulation yields:

$$\tau_f = c' + \left[\left(\sigma - u_a \right) - \sigma^s \right] \tan \phi' \tag{3.8}$$

Pore air pressure is assumed to be atmospheric in surficial soils relevant to terramechanics applications. Setting pore air pressure equal to zero and rearranging the equation produces:

$$\tau_f = \left(c' - \sigma^s \tan\phi'\right) + \sigma \tan\phi' \tag{3.9}$$

The equation now resembles a total stress shear strength envelope consistent with the Bekker framework:

$$\tau_f = c_\theta + \sigma \tan\phi \tag{3.10}$$

where the Bekker friction angle ϕ is equal to effective stress friction angle and moisture-variable cohesion is calculated by combining effective cohesion and effects of matric suction on soil strength:

$$c_\theta = c' - \sigma^s \tan\phi' \tag{3.11}$$

Apparent cohesion is defined by Oh et al. (2012) as the "shear stress resulting from the mobilization of the isotropic tensile stress [i.e. suction stress] by the internal friction". This definition is directly represented in the second term of Eqn. [3.13], which describes the portion of suction stress that is mobilized by interparticle soil friction. Note that suction stress is a negative quantity and therefore moisture-variable cohesion will be greater than or equal to effective cohesion.

Figure 3.3 displays class-average STRESS model estimates for moisture-variable cohesion versus soil moisture for various soil types. These graphs are based on Eqn. [3.13] and are determined from class-average soil properties and the suction stress equation in Eqn. [3.5] and [3.6] (Lu et al., 2010). Currently, moisture-variable cohesion is artificially capped at the value of moisture-variable cohesion when matric suction equals 1500 kPa, which varies based on soil type. In the current suction stress framework (Lu et al., 2010), suction stress (and therefore moisture-variable cohesion) approaches infinity as soil moisture approaches residual water content. This

behavior is unrealistic and exists due to shortcomings in characterizing soil water retention behavior in the adsorbed regime, which Zhang and Lu (2019) aim to address in their updated suction stress formulation. At low water contents, most or all water is adsorbed to soil particles and does not contribute to suction stress in the same way as capillary water. An upper bound on matric suction is imposed at 1500 kPa because Vanapalli and Fredlund (2000) showed the generalization for Bishop's equation $\sigma' = (\sigma - u_a) + S_e(u_a - u_w)$ to perform well within the range of suction from 0 to 1500 kPa. High moisture variable cohesion is anticipated to yield favorable mobility calculations, and the specific magnitude of moisture-variable cohesion for a dry silt, clay, loam, or sandy clay loam are anticipated to be unimportant. Note than in Fig. 3.3, residual water content is assumed to be zero because the residual adjustment factor was calibrated to zero in EMT+VS model calibrations at the test site used in this study, as shown in Chapter 2.

3.3.2 Data Collection and Model Evaluation

The STRESS model was applied at a field site in northeastern Colorado to evaluate model performance. Drake Farm is a former farm with an area of approximately 100 ha. The elevation of the region ranges from 1559 m to 1588 m and slopes range from 0% to over 13% (Fig. 3.4a). Drake Farm was farmed in a wheat-fallow crop rotation for multiple decades until 2012 when the field was transitioned to a Conservation Reserve Program (CRP) site. A native grass blend was planted in 2013 and 2014, but the former strip-cropping pattern is still apparent in the vegetation at the site (Fig 3.4b). Soils at the site are aeolian silt and sand deposits, but the field has been tilled extensively and therefore spatial soil patterns are not representative of natural deposition. 215 points of measured soil textural data are available over the top 30 cm of soil (McCutcheon et al., 2006). Point soil data is interpolated using tension spline interpolation with a weight parameter of 100 as discussed in Chapter 2 to produce a smooth, best-approximation spatial soil pattern (Fig.

3.4c, 3.4d). A complete description of the field site is found in Green et al. (2009) and Green and Erskine (2011).

The EMT+VS and STRESS models were conducted to produce spatial plots of moisture and soil strength parameters over a subsection of the Drake Farm region for three dates. The region of interest, referred to in Fig. 3.4 as "Analysis Region", was selected for EMT+VS and STRESS analysis because of availability of measured soil moisture data for model calibration (as seen in Chapter 2), and proximity to Fort Collins, CO, USA for field measurements of soil strength. All analyses in this study are conducted over this region. The EMT+VS model parameters were calibrated to maximize Nash-Sutcliffe coefficient of efficiency (NSCE) (Nash and Sutcliffe, 1970) using eight dates of measured soil moisture from a portable time domain reflectometry (TDR) device, which measures depth-integrated soil moisture over the top 15 cm of soil. The soil moisture dataset used for calibration consists of eight dates of measured soil moisture with 65 measurements each. Spatial average soil moisture of the calibration dataset ranges from 0.086 on the driest date to 0.216 on the wettest date. All EMT+VS model calibration details, including calibrated parameters, correspond to the CRP period described in Chapter 2. Calibrated model parameters are then used to downscale soil moisture on all soil strength measurement dates using a spatial average of measured soil moisture data on the date of interest (analogous to the input from a coarse resolution soil moisture remote sensing data source). Downscaled soil moisture from the EMT+VS model and interpolated soil textural patterns are input into the STRESS model to estimate friction angle and moisture-variable cohesion.

Soil moisture, cohesion, and friction angle were measured with a bevameter (described in Chapter 4) at 21 locations within the analysis region (Fig. 3.5). Seven 30- by 30-m regions were defined at various locations throughout the region to encompass a variety of topographic,

vegetation, and soil attributes. Green et al. (2009) selected several similar regions over the entirety of the Drake Farm field for measurement of steady state infiltration rates. The regions from Green et al. (2009) that fall within the analysis region were used in this study and three additional regions were defined to encompass regions of extreme soil texture (high interpolated sand percentage or clay percentage). The 30- by 30-m regions were drawn to encompass a grid of 36 digital elevation model (DEM) cells. Three DEM cells were selected in a triangle pattern within each 30- by 30-m region to achieve a target dataset of 21 total measurement locations over the Analysis Region. At these locations, measured effective friction angle and moisture-variable cohesion were compared to parameter estimates from the STRESS model using both input soil moisture from the EMT+VS model. Soil strength and soil moisture data were collected on three dates: a dry date (13 June 2019), a moderate/wet date (25 April 2019), and a wet date (2 May 2019).

The bevameter is an in-situ soil strength measurement device that was introduced by Bekker (1960) and has been recreated in various forms over several decades (Wong, 1980; Apfelbeck, 2011). A human-powered shear strength bevameter was designed and constructed to conduct field testing for this study (Fig. 3.6). The apparatus details and calibration of the shear-strength bevameter are provided Chapter 4. Normal force is applied by dead weight and shear stress is induced in the soil using a moment arm at the top of the device that is rotated manually. For each sampling location, the soil must be sheared three separate times at different normal stresses to calculate shear strength parameters. Because each individual shear test at a given normal stress causes soil deformation, each of the three shear tests corresponding to one sampling location must be conducted at distinct points near the sampling location (Fig. 3.7). The distinct sampling points were selected to encompass similar vegetation and surface characteristics, with no more than one meter between the specified sampling location and the three distinct sampling points.

Soils at Drake Farm typically did not exhibit a peak and ultimate shear strength, and many soils exhibited an increase in shear stress with increasing deformation and continuous shear plate sinkage throughout the test. For consistency between tests, shear stress at failure was defined as the shear stress at 60 degrees of angular displacement. This point was selected based on the results of preliminary laboratory bevameter tests (as shown in Chapter 4), in which 60 degrees marked the approximate transition from elastic to plastic behavior (i.e. the shear stress-displacement curve changes slope).

Bevameter field testing procedure was developed based on an extensive review of bevameter design and testing literature. Based on the literature, normal stresses of 19.2 kPa, 38.9 kPa, and 58.7 kPa were selected. At each testing location, depth-integrated soil moisture was measured over the top 5 cm using a POGO Hydraprobe portable soil moisture measurement device (Stevens Water Monitoring Systems, Inc., Portland, OR, USA) device. For each of the three testing points for each sampling location, vegetation was removed with electric gardening shears to trim grass and weeds and remaining litter was removed by hand (Fig. 3.7). Normal stress was applied to the bare soil surface and the shear annulus was rotated at a rate of 1 rpm until shear failure. Data were processed using a laptop computer. Torque was recorded and converted to shear stress using the equation:

$$\tau = \frac{3T}{2\pi\left(r_o^3 - r_i^3\right)} \tag{3.12}$$

where T is measured torque and r_o and r_i are outer and inner radii of the shear annulus, respectively. The procedure to transform shear strengths to strength parameters is described in Chapter 4. An equation to account for grouser height from Reece (1964) is used in conjunction with the Mohr-Coulomb equation to determine cohesion and friction angle. The equation is fit

using linear least squares regression. Of note, this interpretation of the shear plane may be biased by development of oblique failure planes during shearing (Karafiath and Nowatzki 1978); additional research into prevention of oblique failure planes via a surcharge plate, or interpretation following the procedure outlined by Liston (1973) is needed.

3.4 Results and Discussion

Patterns of soil moisture from the EMT+VS model and soil strength parameters from the STRESS model were prepared for all three dates of soil strength sampling. Figure 3.8 displays modeled patterns of soil moisture. The dry date of data collection has a measured spatial average soil moisture $\overline{\theta} = 0.063$ (used as input for the EMT+VS model), which is drier than any date used for EMT+VS model calibration. The soil moisture pattern on the dry date contains very little spatial variation (Fig. 3.8a). Slight soil effects are observed in the northeast corner, and the southwest corner is slightly wetter as observed in all CRP plots in Chapter 2. Comparing EMT+VS model output to measured soil moisture on this date produces an RMSE value of 0.017. This value is lower than the typical measurement error of a TDR device (Huisman et al., 2001) and indicates that the predictive error of the model is low. The moderate/wet sampling date has a measured $\overline{\theta} = 0.192$. This date shows topographic effects in the soil moisture pattern, as the topographic low (valley bottom) is wetter than the rest of the site (Fig. 3.8b). Additionally, vegetation and soil effects combine to produce a soil moisture pattern that mimics the strip-cropping pattern that is still apparent in the vegetation pattern. Comparing downscaled soil moisture to measured data at the 21 sampling locations produces an RMSE value of 0.035. The wettest date of sampling was measured to have $\overline{\theta} = 0.264$ and is shown in Fig. 3.8c. The wet date again displays the wet valley bottom as well as impacts from the interpolated soil pattern. The soil pattern is apparent on the western half of the region, illustrating the effect of soil composition on soil moisture at this site

under relatively wet conditions (Green and Erskine, 2011). A RMSE of 0.038 is calculated for the wet date, again suggesting low predictive error of the EMT+VS model.

Spatial patterns of soil strength from the STRESS model are shown in Fig. 3.9. Plots in Fig. 3.9 show dependence on both soil texture and soil moisture. The predicted pattern of effective friction angle from the STRESS model (Fig. 3.9a) is independent of soil moisture and is determined based on class-average values from estimated USCS classification based on values reported in Table 3.1. The Drake Farm analysis region shows relatively low spatial variation in soil type (from clay loam to sandy loam), and therefore the pattern of effective friction angle consists of only three discrete values distributed over various portions of the region. Spatial patterns of moisture-variable cohesion were produced using spatial patterns of soil moisture from the EMT+VS model as input. The dry date (Fig. 3.9b) contains high moisture-variable cohesion values for most of the region. Under drier conditions, the soil develops high magnitudes of suction stress, which lead to high apparent cohesion and moisture-variable cohesion values. Lower moisture-variable cohesion is observed over regions with higher sand content, because moisture-variable soil strength in sands is minimal compared to finer-grained soils (Fig. 3.3; Lu et al., 2010). The sandy regions develop moisture-variable cohesion ranging from 12 kPa to 58 kPa, whereas the regions with higher clay content are generally capped at maximum moisture-variable cohesion, which is equal to the moisture-variable cohesion at 1500 kPa of matric suction and varies from 95 kPa to 189 kPa. Under dry conditions shown in Fig. 3.9b, the spatial pattern of moisture-variable cohesion mimics the pattern of soil moisture, but because soil moisture contains little spatial variability and magnitudes of moisture-variable cohesion are high, the effect of soil moisture on moisture-variable cohesion is not visually apparent. The moderate/wet sampling date (Fig. 3.9c) shows combined effects of soil textural and soil moisture patterns. Regions with high clay content

estimated to have higher moisture-variable cohesion (21 to 47 kPa) than regions with higher sand content (1.3 kPa to 14 kPa) due to higher suction stress generated in fine-grained soils. Moderate soil moisture effects on moisture-variable cohesion are apparent in Fig. 3.9c, as drier regions develop higher suction stress and higher moisture-variable cohesion. The wet condition (Fig. 3.9d) contains almost no moisture variability. Under wet conditions, moisture-variable cohesion values are near zero (<10 kPa) and the cohesive strength (independent of external stress) of the soil originates dominantly from effective cohesion. The spatial pattern of moisture-variable cohesion closely resembles the spatial pattern of effective cohesion, which is determined from class average values (Table 3.1).

Measured soil strength parameters at Drake Farm were compared to estimated values from the STRESS model to determine the predictive performance of the model. Effective friction angle (Fig. 3.10) is independent of soil moisture and therefore is predicted to be constant on all measurement dates. The STRESS model consistently underestimates effective friction angle at Drake Farm with an RMSE of 11.3 degrees. Because the estimates are class-averages, they do not vary significantly over the range of soil types present (Table 3.1) and therefore do not capture local variability based on subtle variations in soil texture. A continuous pedotransfer function to predict effective friction angle using sand and clay percentages and other ancillary variables such as density could allow for variation within a given soil type and improve the predictive performance of the EMT+VS model.

Comparisons of measured and predicted moisture-variable cohesion for the three dates at Drake Farm are shown in Fig. 3.11. This plot illustrates that for spatial average soil moisture between 0.063 and 0.264, the STRESS model overestimates moisture-variable cohesion at some locations and underestimates at others. Cohesion from all dates produce an RMSE value of 58.2

kPa with measured moisture-variable cohesion ranging from 0 to 9.59 kPa and predicted moisture-variable cohesion ranging from 1.0 to 189 kPa. The source of most of the observed error is the dry date, which has an RMSE of 110 kPa. As shown in Fig. 3.11, the STRESS model predicts high moisture-variable cohesion for most of the Drake Farm analysis region. Under dry conditions, a surficial soil layer consisting of less than 2-3 cm of dry, loose, sandy soil was observed during field sampling. The grousers on the underside of the bevameter shear plate only penetrate to a depth of 1.59 cm, therefore the measured soil strength parameters correspond to this loose, sandy layer. No moisture-variable cohesion is measured for a loose, sandy soil because suction stress depends on soil pore structure, suction stress is higher for denser soils with smaller pores. Therefore, the discrepancy between measured moisture-variable cohesion and the high predicted moisture-variable cohesion is substantial. A stiffer, higher-strength soil layer was observed to exist directly below the loose superficial layer, which became apparent in taking soil moisture measurements on the dry date. The prongs of the Hydraprobe device were difficult to manually insert to a depth of 5 cm due to the strength of the underlying soil layer. This strength behavior is due to the same moisture-variable cohesion that the STRESS model aims to reproduce but was not captured in surficial bevameter testing. For future field testing, the loose surficial layer should be removed prior to sampling to capture the moisture-variable strength behavior relevant to vehicle mobility.

The moderate/wet and wet dates contain more moderate overestimates and underestimates of moisture-variable cohesion. In general, moisture-variable cohesion is overestimated more frequently than underestimated. These overestimates are hypothesized to occur for multiple reasons. First, the class-average values for effective cohesion are overestimated for the few soils (MH, CL, CH) for which effective cohesion is not estimated to be zero in the STRESS model.

Although these soils are fine-grained and are expected to have some nonzero effective cohesion, class-average values in Table 3.1 relevant to geotechnical engineering applications are not representative of class average conditions in surficial soils. Geotechnical laboratory test specimens are carefully prepared and compacted to a specified density, which is typically greater than the natural density of a surficial soil. The effective cohesion parameter represents electrostatic interparticle forces such as van der Waals forces and the strength of these forces depends on the distance between soil particles. Thus, effective cohesion of a natural surficial soil will be lower than that of a compacted fill or soil deeper below the ground surface if all other variables are equal. The substantial overprediction of moisture-variable cohesion that occurs at several points on the moderate/wet date and wet date is a result of overpredicting effective cohesion in fine-grained soils, specifically CL. Additionally, the STRESS model predicts USCS classification, which depends on both particle size and plasticity, using an empirical conversion from USDA classification (Garcia-Gaines and Frankenstein, 2015), which depends only on particle size. This conversion likely introduces error in predicting class-average parameters because no direct relationship exists between USCS and USDA. For example, the STRESS model predicts clay loam in USDA to be a low plasticity clay (CL) in USCS, which may not be accurate and may lead to an overestimate of effective cohesion and an underestimate of effective friction angle based on class-average values. Another potential source of error is uncertainty in interpolated soil texture patterns, as shown Chapter 2. Interpolated spatial patterns of sand and clay percentage at Drake Farm were shown to have relatively high error despite 215 points of measured soil texture. This predictive error exists because of the repetitive tilling that occurred at Drake Farm for multiple decades in addition to the inherent variability and uncertainty that exists in spatial interpolation of soil data.

Underestimates of moisture-variable cohesion shown on the wet date are likely caused by uncertainty in soil data that leads to inaccurate estimates of suction stress.

In general, the results for all three dates indicate that terramechanics-specific pedotransfer functions are necessary to accurately predict effective stress strength parameters and van Genuchten parameters. Natural surficial soils exhibit different behavior than the geotechnical and compacted agricultural soils for which the class-averages and pedotransfer functions used in the STRESS model were prepared. All relevant soil properties are dependent on density, and the STRESS model currently neglects all density effects. Creating pedotransfer functions specific to terramechanics applications would partially address the issue of density-specific soil properties, but density should also be considered as a pedotransfer input to completely characterize the effect of density on various soil properties.

3.5 Summary and Conclusion

This study introduces the STRESS model to predict strength parameters of unsaturated surficial soils for vehicle mobility. The STRESS model is paired with the EMT+VS soil moisture downscaling model to predict soil moisture and soil strength as a function of basic topographic, vegetation, and soil data, and coarse resolution soil moisture. The STRESS model uses pedotransfer functions and unsaturated soil mechanics to predict soil shear strength parameters (cohesion and friction angle) that may be input into numerical terramechanics models. The model was applied to a test region in northeastern Colorado and bevameter measurements were collected to evaluate predictive performance. The following conclusions can be made from this study:

1. In general, the STRESS model captures the approximate magnitude of Bekker strength parameters when compared to field-measured values. Although high moisture-variable cohesion values predicted by the STRESS model are not currently captured in field testing, the

effect of suction stress on soil strength is known to occur at lower water contents. The bevameter field testing methodology should be amended to capture the true strength behavior relevant to terramechanics.

2. Friction angle estimates from the STRESS model are limited by existing class average soil strength databases. The class-average values of effective friction angle do not capture natural variability and are incapable of representing soils that are stronger or weaker than the average soil within a given soil textural class. Results at Drake Farm show values that are generally underestimated.
3. Cohesion estimates from the STRESS model are limited by class average cohesion estimates from soil strength databases. The effective cohesion values of fine-grained soils are overestimated by the model. The model can also overestimate suction stress and therefore moisture variable cohesion due to uncertainty in soil input data.
4. More data are required to improve the predictive performance of the STRESS model. A dataset relating effective shear strength parameters to soil texture percentages for surficial soils relevant to terramechanics is required to develop continuous predictive relationships.

The STRESS model should be applied to other test regions to gain a better understanding of the model's predictive capability. Additional test regions should be selected based on varying topography and soil conditions. Measured soil moisture data must be available or should be collected as part of STRESS model verification. Measured data can be compared to predicted data following the process outlined herein.

3.6 Tables and Figures

Table 3.1 Comparison of class average effective stress strength parameters. The columns corresponding to USBR are derived from a dataset of 17 soils from the western United States. The third set of values is from the United States Department of Agriculture Forest Service Slope Stability Reference Guide (1994), which compiles values from the USDA Transportation Engineering Handbook (1981) and only provides class-average friction angles for coarse-grained soils.

USCS Classification	NAVFAC (1986)		USBR (1998)		USDA (1981) (via USDA, 1994)				STRESS Model Parameters			
					Loose		Dense		c' (kPa)		ϕ' (°)	
	c' (kPa)	ϕ' (°)	c' (kPa)	ϕ' (°)	c' (kPa)	ϕ' (°)	c' (kPa)	ϕ' (°)	Value	Reasoning	Value	Reasoning
GW	0	>38			-	35	-	45	0	Gravel and sand (GW through SC) are coarse-grained materials and are considered cohesionless in soil mechanics practice (Terzaghi, 1943). These soils do not develop interparticle cohesive forces. Low plasticity silt is a fine-grained soil but has been shown to exhibit cohesionless behavior (Vanapalli et al., 1996; Vanaut et al., 2002). In the loose condition expected in natural surficial soils (Hunt and Gilkes, 2002; Goldsmith et al., 2001), zero cohesion is predicted as a conservative estimate.	35	Friction angles for loose soil from USDA (1981) via USDA (1994) due to applicability to surficial soils. Low density soils are consistent with effective plant growth (Hunt and Gilkes, 1992; Goldsmith et al., 2001). Therefore, natural surficial soils are anticipated to be low density. For soils with a range of friction angles, the median value is chosen.
GP	0	>37	8.1	42.2	-	33	-	43	0		33	
GM	-	>34			-	33	-	43	0		33	
GC	-	>31			-	33	-	43	0		33	
SW	0	38			-	31	-	41	0		31	
SP	0	37			-	31	-	41	0		31	
SM	20	34	20.7	34		29-31	-	39-41	0		30	
SC	11	31	19.3	32.7					0		31	See below justification for CL through CH
ML	9	32	4.80	35.2		26		36	0		26	See above justification for GW through SM
CL	13	28	15.2	28.1					13	Cohesion is often considered the primary source of shear strength of high plasticity soils (Terzaghi, 1943). Even in a loose state, the nonzero values from NAVFAC (1986) provide a realistic estimate.	28	Friction angles from NAVFAC (1986) are used for SC, ML, MH, and CH because no values are provided by USDA (1981). Although NAVFAC (1986) does not contain a density-related component, these values are typically used in US government applications.
MH	20	25							20		25	
CH	22	19	32.4	20.5					22		19	

USCS Classifications are defined as follows: GW = well-graded gravel, GP = poorly-graded gravel, GM = silty gravel, GC = clayey gravel, SW = well-graded sand, SP = poorly-graded sand, SM = silty sand, SC = clayey sand, ML = low plasticity silt, CL = low plasticity clay, MH = high plasticity silt, CH = high plasticity clay

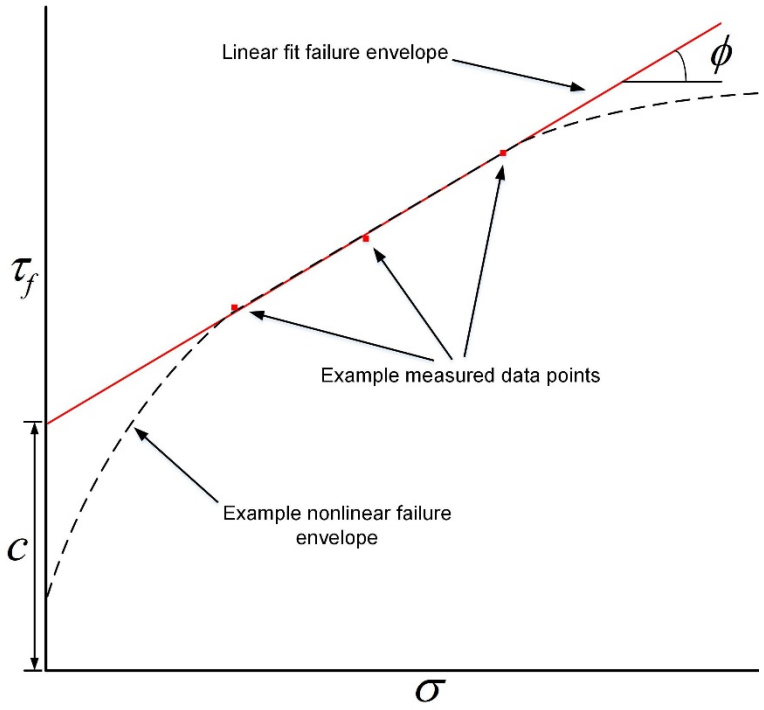

Fig. 3.1 Schematic illustration of linear fit failure envelope and true nonlinear failure envelope. τ_f is shear stress at failure, σ is normal stress (in terms of total applied stress), ϕ is friction angle, and c is cohesion.

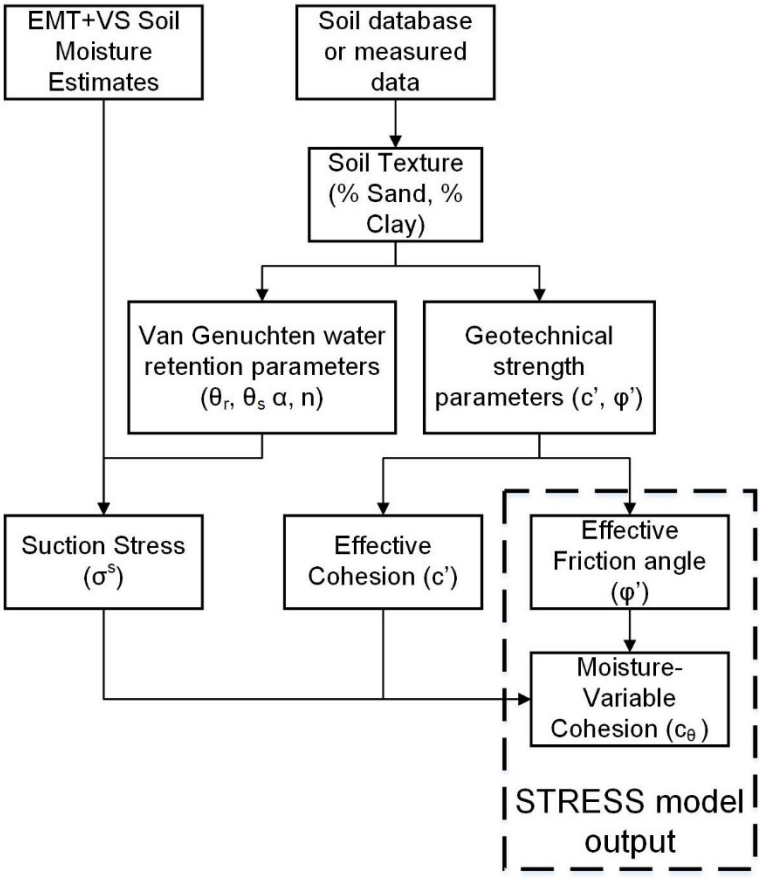

Fig. 3.2. Diagram of STRESS model framework

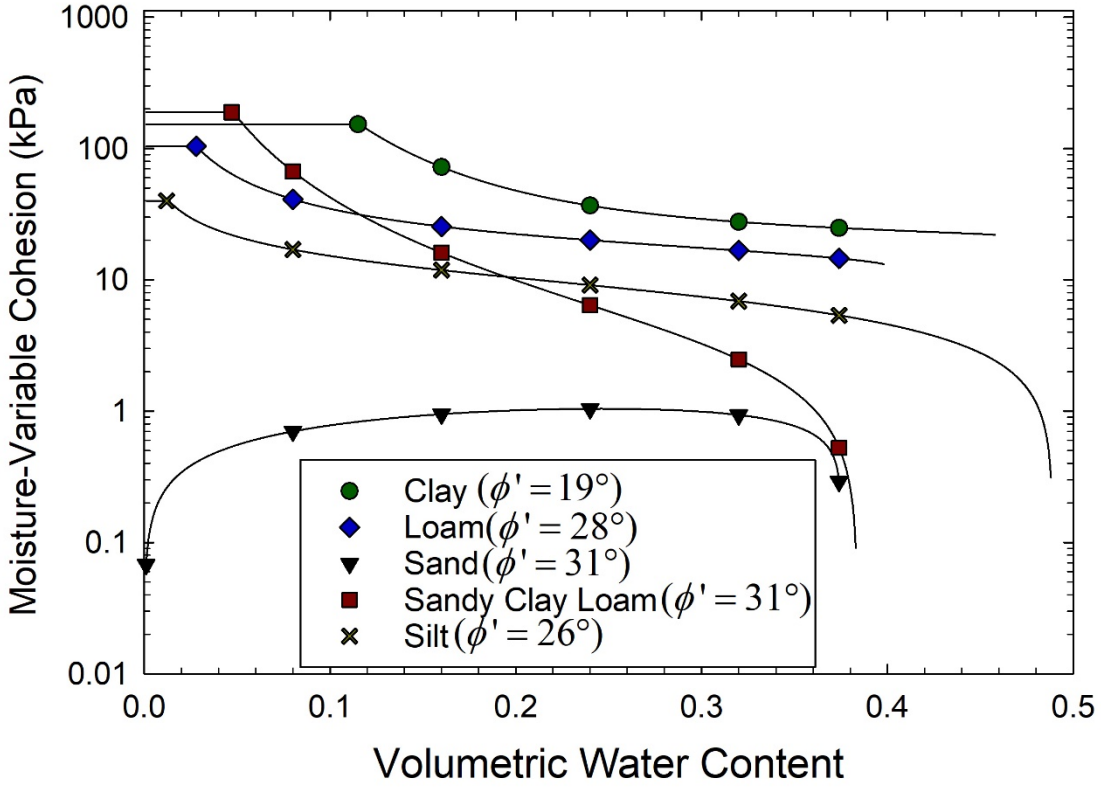

Fig. 3.3. Class-average STRESS model estimates for moisture variable cohesion (c_θ) for various USCS soil types. Effective stress friction angles (ϕ') of each soil class are also included in the legend.

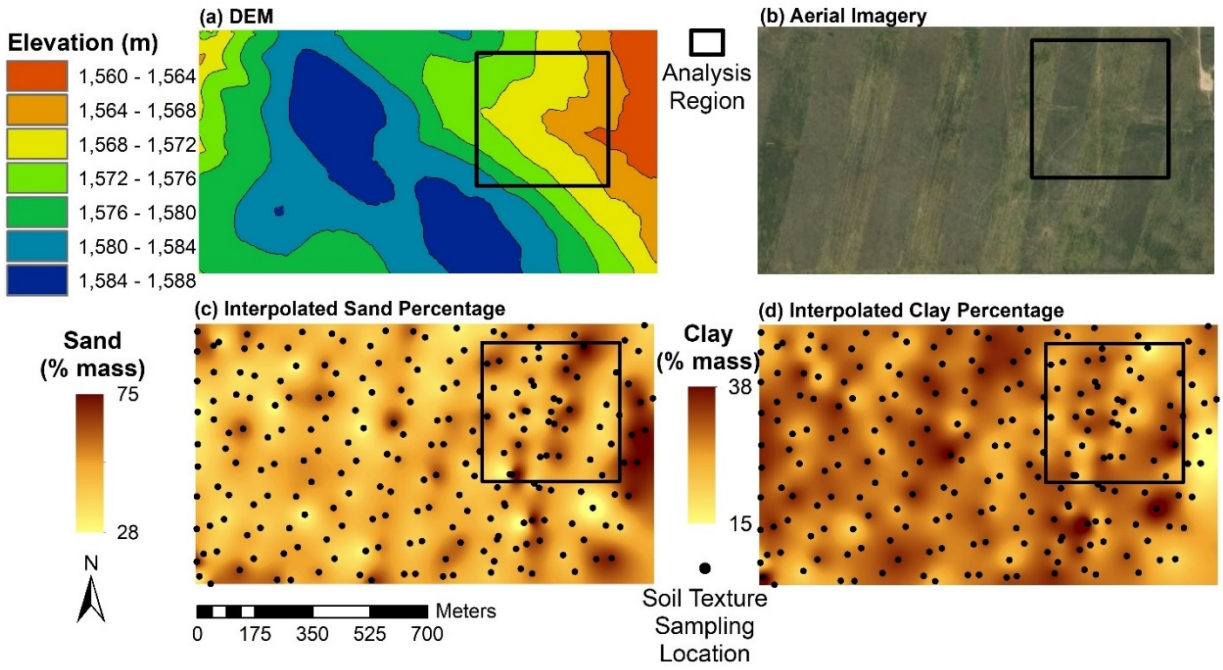

Fig. 3.4. Drake Farm field site description, including region of analysis of this study denoted with a black rectangle, including (a) digital elevation map (DEM), (b) aerial photograph, (c) interpolated percentage of sand by mass with soil sampling locations, (d) interpolated percentage of clay by mass with soil sampling locations

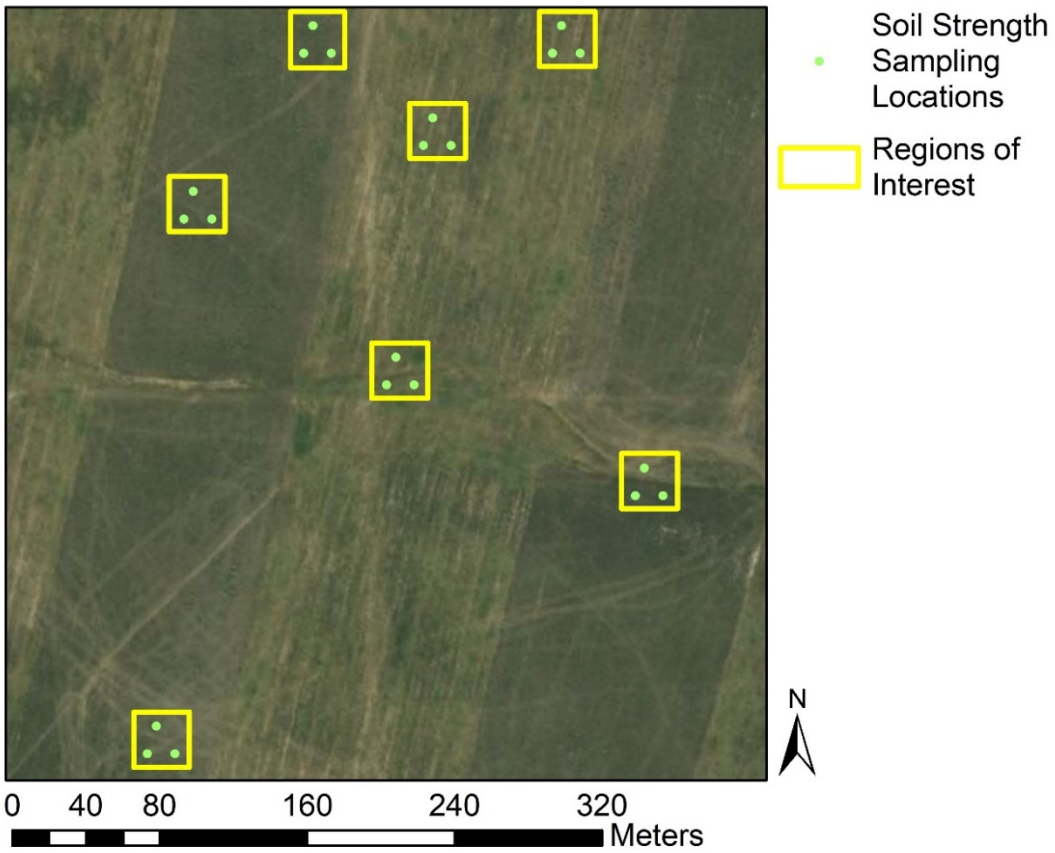

Fig. 3.5. Soil strength sampling locations (21 locations) over the analysis region, with underlying aerial photograph from September 2017

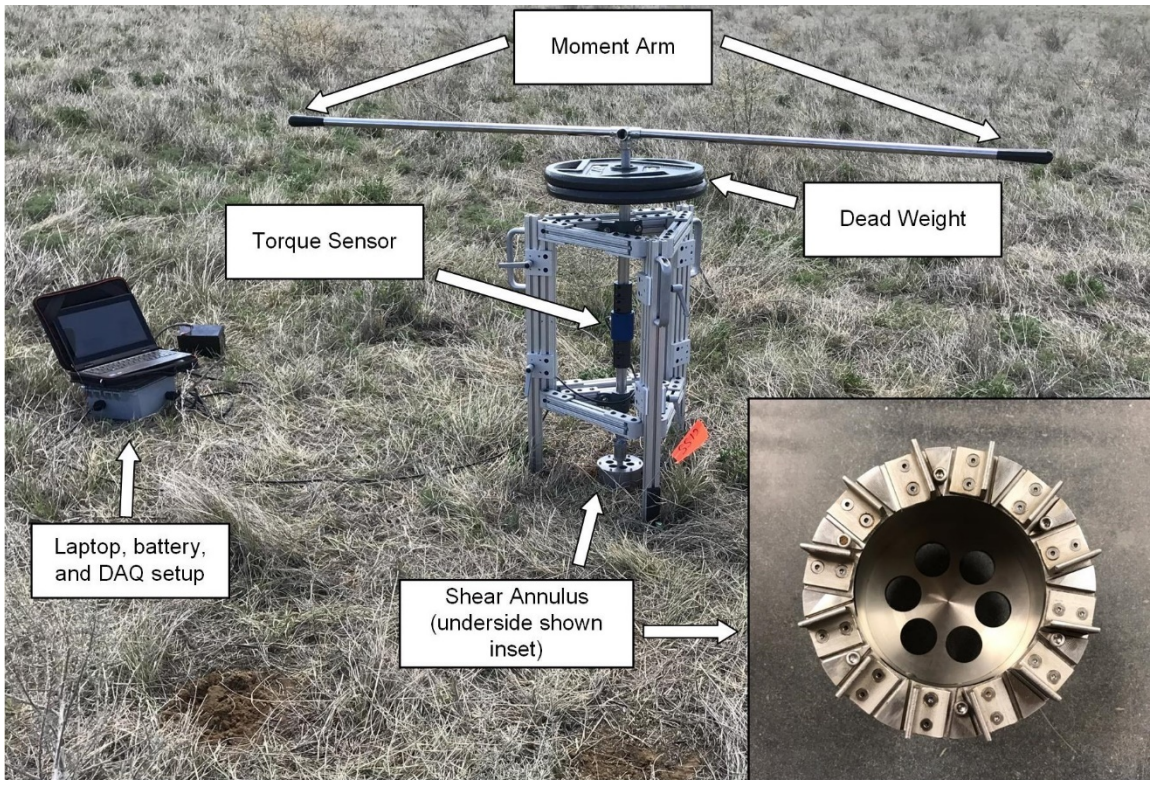

Fig. 3.6. Human-powered shear strength bevameter applied at Drake Farm

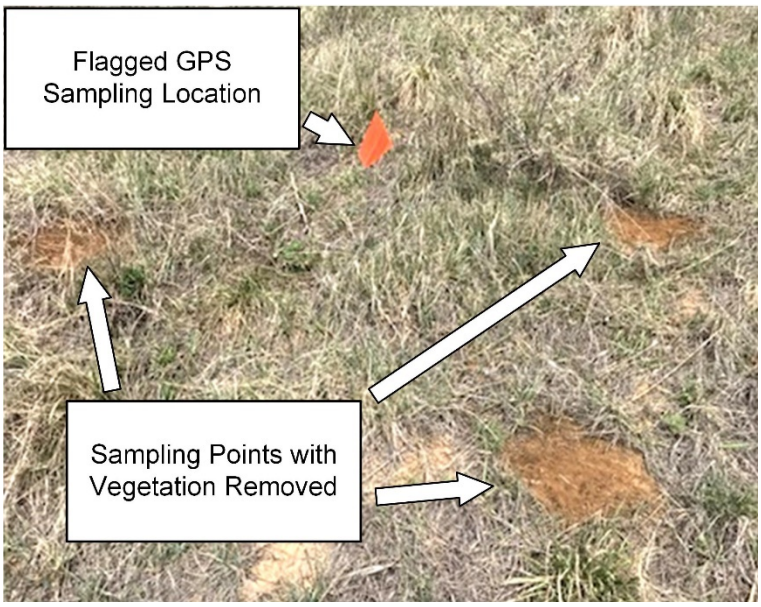

Fig. 3.7. Drake Farm soil strength sampling location with three testing points. Flag denotes GPS-specified sampling location.

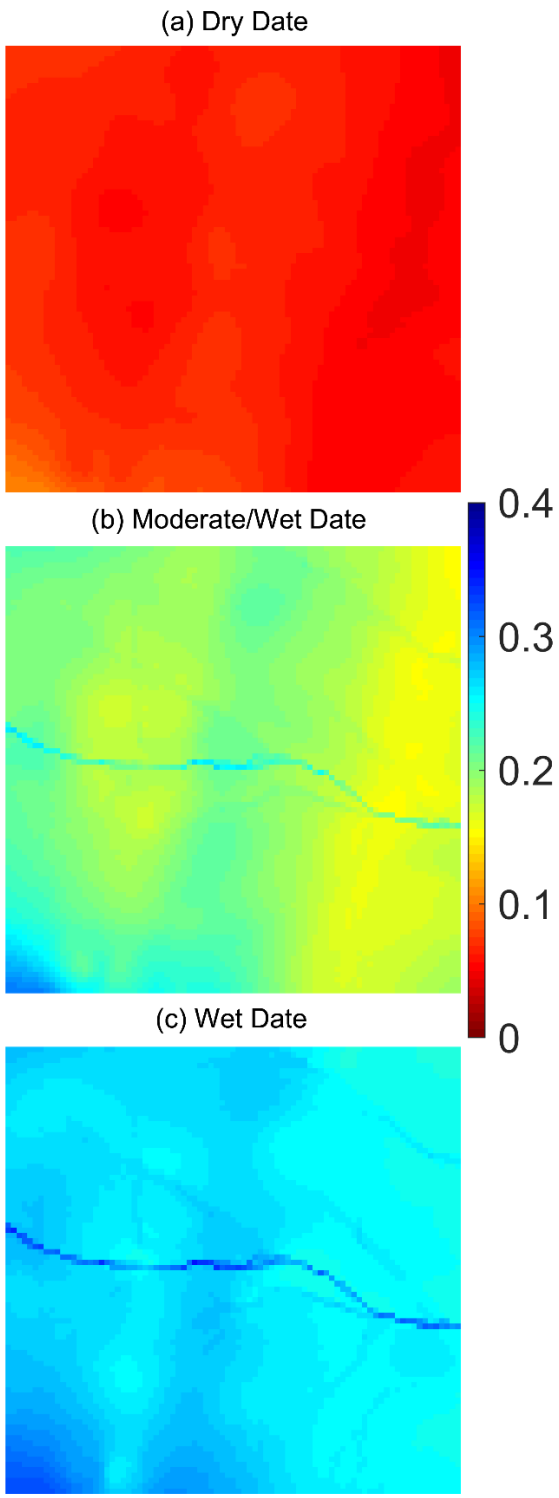

Fig. 3.8. Spatial soil moisture patterns from EMT+VS model on soil strength sampling dates. (a) dry date, 13 June 2019 ($\overline{\theta} = 0.063$), (b) moderate/wet date, 25 April 2019 ($\overline{\theta} = 0.192$), (c) wet date, 2 May 2019 ($\overline{\theta} = 0.264$)

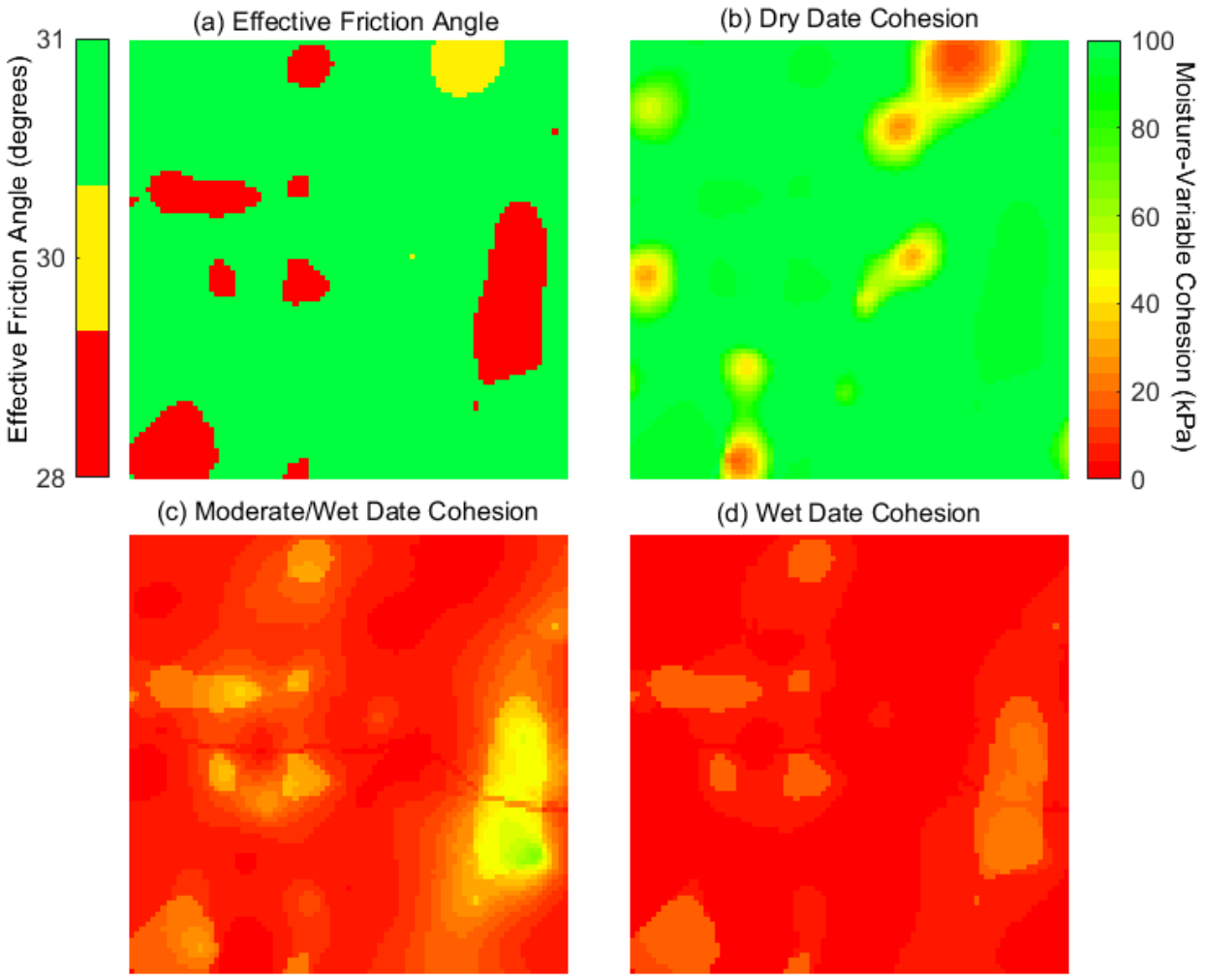

Fig. 3.9 STRESS model soil strength patterns for (a) friction angle (degrees), (b) moisture-variable cohesion on dry date (13 June 2019) (kPa), (c) moisture-variable cohesion on moderate/wet date (24 April 2019) (kPa), (d) moisture-variable cohesion on wet date (2 May 2019). Soil moisture input for moisture-variable cohesion from EMT+VS model output for same dates.

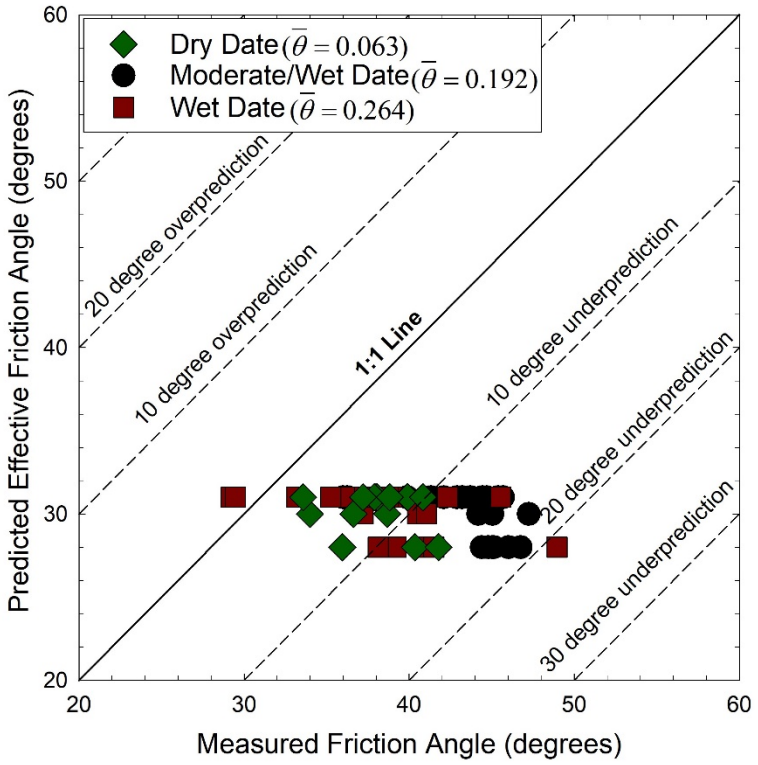

Fig. 3.10. Comparison of measured to predicted friction angle values at Drake Farm

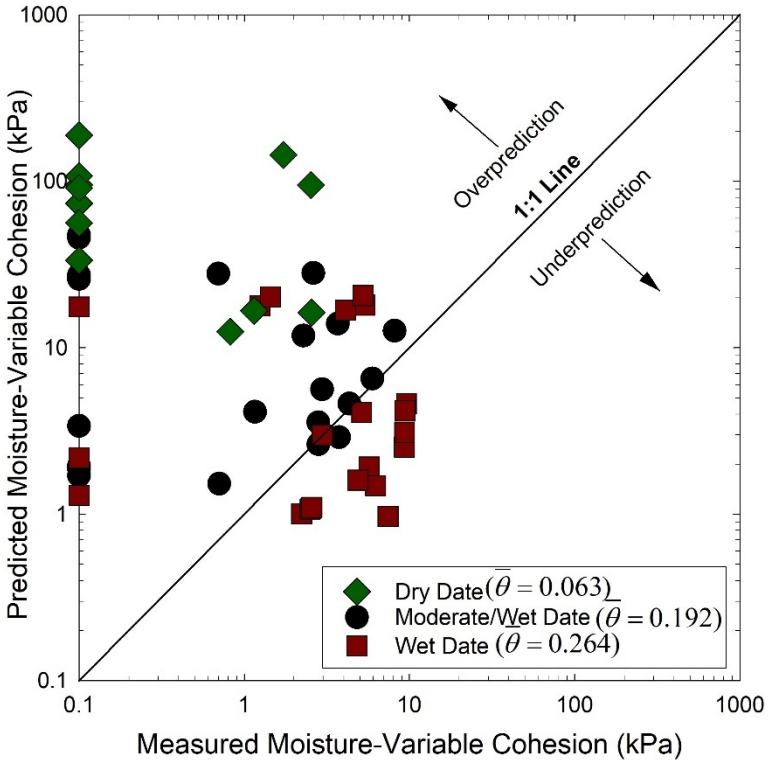

Fig. 3.11. Comparison of measured to predicted moisture-variable cohesion values at Drake Farm

4. BEVAMETER DESIGN

4.1 Introduction

The bevameter is a device used to measure near surface soil strength in terramechanics. Bekker (1956) states that shear resistance and deformation are the two key soil properties for assessing vehicle mobility. Thus, parameters that represent the shear strength and compressibility of a soil are necessary to adequately characterize soil for vehicle mobility modeling. The bevameter measures these properties in a natural, in-situ condition using two tests. The pressure-sinkage test is used to measure compressibility. A flat circular or rectangular steel plate is pressed into the soil at a constant rate, and force and vertical displacement are measured. Bekker-Wong pressure-sinkage parameters are fit to the data to characterize compressibility. The shear test is conducted using an annular shear ring with grousers on the underside. A constant normal force is applied to the soil surface by the annular plate and the shear plate is rotated at a constant rate, inducing a horizontal shear plane in the soil. The torque generated is then recorded as a function of angular displacement. Bekker shear strength parameters are calculated to quantify resistance to shear.

Despite approximately six decades of bevameter research, a paucity of bevameter data exists in the field of terramechanics. Additionally, the bevameter design and measurement procedures lack standardization. Each bevameter design has been unique (Dwyer et al., 1974; Wong, 1980; Apfelbeck et al., 2011) because each device has been designed for specific research purposes. The objective of this study is to design, construct, and calibrate multiple bevameter devices for field and laboratory testing based on previous designs. The first device is a laboratory-focused bevameter with automated electrical controls and capability to complete both pressure-

sinkage and shear tests. This device is designed to enable field operation but requires several people for transportation and testing. The second device is a simpler, human-powered bevameter shear strength device. This device relies on human-applied force to induce shear stress in the soil and dead weights to apply normal stress. The shear-strength bevameter is designed for efficient field testing and easy transportation. Bevameter design parameters were identified from a review of operational parameters in the literature. The designs of both bevameters are provided. A laboratory testing campaign is summarized for the shear-strength bevameter device. Test results from the field-focused shear strength bevameter are compared to traditional geotechnical shear strength testing results on specimens prepared under identical conditions to validate the bevameter design and testing procedure. Laboratory validation for the laboratory-focused bevameter is not included as part of this study.

4.2 Background

Rating cone index (RCI) has been the preferred method of quantifying soil strength in terramechanics vehicle mobility applications due to ease of measurement and simplicity of application (Rula and Nuttall, 1971). However, the need for mechanical strength parameters for complex terramechanics models has reinvigorated interest in the bevameter (McCullough et al., 2017). The bevameter offers a more robust method of estimating soil properties and allows for a better understanding of individual processes that govern soil vehicle interaction. The pressure-sinkage test is one of the two bevameter tests and is used to measure soil compression behavior (Fig. 4.1a). The laboratory-focused bevameter contains pressure-sinkage capabilities, although no pressure-sinkage laboratory validation occurred as part of this study. A flat circular or rectangular plate is pushed into the soil at a constant rate and force and vertical displacement are measured. Bekker-Wong pressure-sinkage parameters are fit to the data to characterize soil compressibility.

The second test procedure is used to measure soil shear strength (Fig. 4.1b). The bevameter shear test is based on traditional Mohr-Coulomb strength theory (Coulomb 1776; Mohr 1900). A circular shear annulus with grousers on the underside (Fig. 4.1b) is fully pressed into the soil to achieve a constant normal stress. The shear ring is then rotated at a constant rate until the soil fails in shear along a horizontal failure plane that is induced in the soil at the bottom of the grousers. In this way, the bevameter shear test is analogous to a torsional ring shear test. Applied torque is converted to shear stress using the following equation:

$$\tau = \frac{3T}{2\pi\left(r_o^3 - r_i^3\right)} \tag{4.1}$$

where τ is soil shear stress, T is applied torque, and r_o and r_i are outer and inner radii of the shear annulus, respectively. Depending on the application of bevameter testing, the maximum or ultimate shear stress is recorded as shear stress at failure (τ_f) for a given constant normal stress. The bevameter shear procedure is repeated at a minimum of three normal stresses to characterize the relationship between shear stress at failure at a corresponding applied normal stress (σ). Shear strength parameters cohesion (c) and friction angle (ϕ) are fit from a linear Mohr-Coulomb failure envelope fit to the data:

$$\tau_f = c + \sigma_f \tan\phi \tag{4.2}$$

The bevameter was originally introduced in 1960 by the terramechanics community and the ensuing decade contained substantial research with the device (Janosi and Hanamoto, 1961; Wills, 1964; Liston et al., 1966; Hegedus and Liston, 1966; Spanski, 1966). However, interest in the bevameter was sparse from the 1970s through the early 2010s (Dwyer et al., 1974; Wong, 1980; Wong, 1984; Apfelbeck et al., 2011). Over the past decade, bevameter research has once again increased in the context of extraterrestrial exploration as NASA and similar organizations

use the device to examine strength of planetary soil simulants or Martian and Lunar soils (Edwards et al., 2017). Available literature was examined to develop a generalized bevameter design and operation procedure. A list of operational parameters compiled from the literature and used to define desired parameters for the bevameter devices in this study is provided in Table 4.1.

Bevameter design parameters vary substantially throughout the literature. Many devices are vehicle-mounted, hydraulic-powered systems. The majority of bevameters described in the literature perform pressure-sinkage and shear strength testing separately using different systems, primarily due to limitations in control system capabilities. More recent devices (Apfelbeck et al., 2011) conduct both bevameter tests with a single, compact machine and rely on electrical power and feedback controls for all application and measurement of force and torque.

Bevameter pressure-sinkage devices in the literature use a hand crank (Spanski, 1966; Dwyer et al., 1974) or piston (Wong, 1980; Apfelbeck et al, 2011; Edwards et al., 2017) to apply vertical downward force in pressure-sinkage testing. Vertical motion considerations include maximum applied force, maximum stroke (length of extension), and extension (sinkage) rate. If a piston is used for force application, the device must be capable of applying a dynamic load for pressure-sinkage testing. Multiple sinkage plates should also be used and should contain a range of sizes that are representative of vehicle loading. Table 4.1 summarizes literature values for all relevant pressure-sinkage parameters.

In shear strength testing, normal force is applied to the soil surface using dead weight (Spanski, 1966; Dwyer et al., 1974; Wong, 1980) or using a piston (Apfelbeck et al., 2011; Edwards et al., 2017). If a piston is used, a single device can be used for pressure-sinkage and shear strength testing. However, this method requires programming an electrical control system to maintain a constant normal force on the soil surface. Normal forces applied during pressure

sinkage testing are typically greater than the forces applied during shear strength testing, so the design parameters discussed in the previous paragraph dictate piston considerations for a bevameter design that uses a single piston for both bevameter tests. Torque can be applied during a shear strength test by manually turning a mechanism attached to the bevameter shaft (Spanski, 1966; Dwyer et al., 1974) or using a motor (Wong, 1980; Apfelbeck et al., 2011; Edwards et al., 2017). Considerations for shearing the soil are maximum applied torque and rate of rotation (i.e. shearing rate). Shear plate properties should be representative of a vehicle tire or tank track, but small enough to be practical for field and laboratory testing. Shear plate considerations are inner and outer radii of the shear annulus, grouser depth, and number of grousers. Table 4.2 contains all literature values for relevant shear testing parameters.

4.3 Bevameter Design

Target operational parameters were selected based on the range of reported literature values (Tables 4.1 and 4.2). For the laboratory-focused device, maximum normal force was selected to remain low enough to be counterweighted by the weight of the machine and a modest quantity of additional dead weight (3600 N). The maximum normal stress corresponding to the smallest pressure-sinkage plate (diameter=5.08 cm) is 1776 kPa and the maximum normal stress corresponding to the largest pressure-sinkage plate (diameter=15.2cm) is 198 kPa. The maximum normal stress applied in shear testing is 355 kPa based on the selected shear plate dimensions ($r_o = 15.2\text{cm}, r_i = 10.2\text{cm}$). Maximum torque was selected using a similar reasoning as normal force, by limiting torque to minimize likelihood of tripod feet slipping on soil surface in reaction to soil shearing. The maximum normal load and torque of the field-focused shear strength bevameter were selected to mimic the design parameters for the laboratory-focused device, while accounting for limitations of dead weight and human effort.

4.3.1 Laboratory Bevameter Device

Hydraulic, pneumatic, and electrical systems were considered to power the laboratory-focused bevameter. Hydraulic systems require a hydraulic motor and reservoir and were deemed too cumbersome for efficient operation under manual transport. Pneumatic systems have the potential to rupture under field use and require a compressed air source (e.g., air compressor). Therefore, an electrical system was selected to provide adequate force and torque while remaining easy to transport. A tripod design was selected for field-capable structural efficiency.

Figure 4.2a shows the laboratory-focused bevameter with parts labeled. Figure 4.2b shows the pressure sinkage testing plates and Fig. 4.2c and 4.2d show the side and bottom of the shear testing plate, respectively. Additionally, Table 4.3 summarizes the mechanical and electrical components with force and torque application and measurement capacities for comparison with target design properties. Linear force is provided by a Parker ETH032M05 mechanical linear actuator with parallel BE233 motor (Parker Hannifin, Cleveland, OH, USA). Torque is supplied by a Parker BE343J electric motor with integrated encoder paired with a Carson Eliminator 70:1 planetary gearbox to increase torque output and decrease rate of rotation (Carson Manufacturing, Carson City, NV, USA). Force and torque are measured using an Interface 2816 2-axis Torsion Load Cell (Interface, Inc., Scottsdale, AZ, USA). Vertical deformation is measured using Omega LDI-128 LVIT sensor (Omega Engineering, Inc., Norwalk, CT, USA). All tripod legs and structural members are constructed from commercially available aluminum T-slotted framing. Aluminum mounting plates, stainless-steel load cell mounts, and stainless-steel testing plates were custom machined in Fort Collins, CO, USA; design drawings for these components are provided in the Appendix. Force, torque, and deformation rate controls are provided using a Copley XE2 digital servo drive (Copley Controls, Canton, MA, USA). The electrical design allows for the use

of analog outputs from the multi-axis load cell (force, torque), motor encoder (shear rate), and LVIT sensor (sinkage rate) to control the various testing parameters involved in pressure-sinkage and shear testing.

4.3.2 Field-Focused Shear Strength Bevameter

Figure 4.3 is a photograph of the field-focused shear strength bevameter with labeled components. The only electrical component, an Interface TS12 Shaft Style Reaction Torque Transducer (Interface Inc., Scottsdale, AZ, USA), is shown in Table 4.3 to compare the torque sensor capacity to target bevameter design torque. The field-focused shear strength bevameter is powered by human-applied force and dead weight is used to apply normal stress. Therefore, the need for hydraulic, pneumatic, or electronic force application and control is eliminated. A tripod design was also selected for the field-focused shear strength bevameter for stability. A moment arm at the top of the device is rotated by users to generate shear stress in the soil. The moment arm is connected to the torque transducer via a steel shaft. Another steel shaft connects the torque transducer down to the shear annulus at the soil surface. The shaft passes through two sleeve bearings, which are connected to a structural frame and are incorporated to ensure proper shaft alignment. The frame is constructed from commercially available T-slotted framing. The field-focused shear strength bevameter uses the same shear annulus as the laboratory bevameter (Fig. 4.2c, 4.2d).

4.4 Materials and Methods

A soil referred to as “Filter Sand” was used for bevameter laboratory validation. Sieve, hydrometer, Atterberg limit, specific gravity by pycnometer method, and standard Proctor compaction testing were conducted to classify and characterize the soil. Results of laboratory classification are summarized in Table 4.4. Bevameter laboratory testing was conducted in a 90

cm diameter galvanized steel tank with a height of 58 cm. The target density for laboratory testing was set to 85% of standard Proctor maximum dry density (Table 4.3) to simulate natural in situ soil density (Goldsmith et al., 2001; Albright et al., 2010). The typical standard Proctor curve is approximately parabolic, but several factors such as grain size distribution have been shown to influence the shape of the curve and produce atypical behavior (Johnson and Sallberg, 1962). The Filter Sand displayed a flat compaction curve with little variation in dry density with varying water content. Thus, the sand was loosely deposited into the testing tank to achieve the target density. The testing set-up was configured to elevate the laboratory bevameter above the steel tank and vertically align testing plates with the soil surface (Fig. 4.4a). The field-focused shear strength bevameter was placed atop the soil within the testing tank (Fig. 4.4b).

Geotechnical shear strength testing was conducted on both soils for comparison with bevameter laboratory measurements. Direct shear testing (ASTM D 3080/D 3080M-11) was conducted at 25% of saturation and at a fully saturated state. Direct shear testing was conducted at normal stresses increments of 17.6 kPa, 33.4 kPa, and 49.2 kPa. Table 4.5 summarizes the volumetric and gravimetric water contents for the Filter Sand at the target density and level of saturation. Additionally, consolidated-undrained (CU) triaxial testing was conducted (ASTM D 4767-95) at a confining stress of 41.4 kPa. Each test was prepared to the same target density used in bevameter testing.

The bevameter shear plate has an outer diameter of 15 cm and an inner diameter of 10 cm (Fig. 4.2c, 4.2d). The plate contains 12 grousers at a depth of 1.6 cm (Fig. 4.2c, 4.2d). For laboratory testing of the field-focused shear strength bevameter, the three legs were set on the soil surface and were adjusted to align the bottom of the shear plate with the soil surface. The legs were fixed to the soil surface using stakes (8 mm diameter, 248 mm length). Three shear tests must be

conducted at different normal stresses for each set of shear strength parameters. The first normal load increment applied by the field-focused shear strength bevameter corresponds to the weight of the shear plate, shaft, torque sensor, and moment arm and results in a normal stress of 19.2 kPa based on the dimensions of the shear plate. The second load increment is applied by adding a plate weight with a mass of 20.4 kg, resulting in a normal stress of 38.9 kPa. Another identical plate is added for the final load increment, corresponding to a normal stress of 58.7 kPa. For each normal load, the user shears the soil by pushing horizontally on the moment arm to induce rotation at a constant rate of 1 rpm. Torque sensor data are recorded on a laptop computer and processed to produce plots of shear stress (τ) versus angular displacement (δ) for each normal stress (σ). An example plot is shown in Fig. 4.5a. For each plot, shear stress at failure τ_f is determined at 60 degrees of angular displacement. As shown in Fig. 4.5a, 60 degrees is the approximate angular displacement at which the soil transitions from elastic to plastic behavior (i.e. the plot of τ_f vs. δ changes slope). Finally, τ_f is plotted versus σ and a linear function is fit to the data using linear least squares regression (Fig. 4.5b). Friction angle and cohesion are determined from the slope and intercept of the linear fit, respectively. An equation from Reece (1964) is used to consider the effects of grouser depth (h) on measured cohesive strength:

$$\tau = c\left(1 + \frac{2h(r_o - r_i)}{r_o^{\,2} - r_i^{\,2}}\right) + \sigma \tan\phi \tag{4.3}$$

To ensure repeatability of measurements, a set of nine measurements was conducted at each normal stress on the Filter Sand at $S = 25\%$. These tests were used to ensure that repeated measurements with the field-focused shear strength bevameter on the same soil produce similar results. Shear strength parameters were fit from the nine replicate measurements to ensure repeatability as well as for comparison with geotechnical strength data. Three replicate

measurements were conducted at each normal stress in the saturated state for comparison with geotechnical data. For the saturated case, three sets of measurements were conducted. Note that in the unsaturated state ($S = 25\%$), measured cohesion is moisture-variable cohesion (c_θ), combining capillary and effective cohesion. In the saturated state, measured cohesion is equal to effective cohesion (c').

4.5 Results and Discussion

Figure 4.6 summarizes the repeatability investigation conducted on the Filter Sand at $S = 25\%$. The nine curves of shear stress versus angular displacement corresponding to each normal stress increment are shown in Fig. 4.6a. The curves for each normal stress display general agreement, as similar shear stresses are measured in each set of tests. Shear stress at failure ranges from 13.7 kPa to 16.8 kPa for the first normal load increment (19.1 kPa), 21.2 kPa to 26.8 kPa for the second normal load increment (38.9 kPa), and 28.8 kPa to 34.9 kPa for the third normal load increment (58.7 kPa). No outliers or unusual curves exist to indicate that the field-focused shear strength bevameter measurements are not repeatable. The linear fits for each of the nine measurement iterations are shown in Fig. 4.6b. The linear fits also show acceptable agreement. Cohesion ranges from 3.98 kPa to 8.02 kPa with a mean of 5.93 kPa, and friction angle ranges from 18.2 degrees to 25.6 degrees with a mean of 22.8 kPa. Bareither et al. (2008) showed that direct shear testing on identical sands could yield variability in cohesion up to 40 kPa and up to 18 degrees in friction angle when conducted using the same procedure at different laboratories. Based on this documented variability in geotechnical testing, repeated tests by the field-focused shear strength bevameter were deemed to provide acceptable bounds of variability between tests.

A comparison between bevameter and geotechnical measurements is presented in Table 4.6. Presented in Table 4.6 are minimum, mean, and maximum shear strength parameters measured

in the multiple test replicates. Bevameter-measured friction angle and cohesion are compared to companion values measured by direct shear and CU triaxial testing. Note that triaxial testing is conducted in a saturated state, so no values are available for direct comparison to the unsaturated ($S = 25\%$) case. Additionally, only one CU triaxial test was completed so the single set of shear strength parameters are presented as the mean values. Filter Sand shows agreement between friction angle measured using direct shear, CU triaxial, and bevameter methods with mean friction angle ranging from 25.6 degrees to 35.2 degrees. As discussed previously, Bareither et al. (2008) showed that shear strength parameters of identical sands can vary by as much as 18 degrees between direct shear tests conducted using the same procedure at different laboratories. Additionally, effective friction angles measured by triaxial and direct shear testing on the same soil with identical preparation have been shown to vary by approximately 5 degrees on average, with variation in excess of 9 degrees (Superfesky and Williams, 1978; Maccarini, 1993). This inherent variation between testing methods indicates that some variation between bevameter shear strength parameters and geotechnical loboratory testing shear strength parameters is anticipated. Further testing is required to analyze the relationship between friction angle measured using traditional geotechnical methods and the field-focused shear strength bevemeter, but the general agreement is observed in this study validates the field-focused shear strength bevameter for field testing. The lack of direct agreement between bevameter and geotechnical laboratory values is also the reason that field-focused methods such as the bevameter, and not geotechnical laboratory testing, are used in terramechanics.

Filter Sand also show similar cohesion between bevameter and geotechnical measurements (Table 4.6). Like friction angle, Bareither et al. (2008) showed that cohesion in sand can vary substantially (nearly 40 kPa) depending on individual laboratory testing. Similarly, Maccarini

(1993) measured cohesion values varying by up to 20 kPa between direct shear and consolidated drained (CD) triaxial testing. The slight variations observed between direct shear, CU triaxial, and bevameter testing are interpreted to demonstrate the ability of the field-focused shear strength bevameter to measure near-surface soil strengths in the field. Mean moisture-variable cohesion in unsaturated Filter Sand ranges from 5.93 kPa to 7.03 kPa and mean effective cohesion in the saturated condition ranges from zero to 4.81 kPa. Additionally, cohesion is measured to increase with decreasing soil moisture, as is observed in direct shear testing. These measurements capture the phenomenon of moisture-variable cohesion, which combines effects of capillary cohesion and effective cohesion. The change in measured cohesion from the saturated to unsaturated state is small because coarse-grained soils are known to develop low suction stress (Lu et al., 2010) and therefore low moisture-variable cohesion. These data illustrate the potential of the field-focused shear strength bevameter to measure moisture-variable cohesion.

4.6 Summary and Conclusion

An automated laboratory-focused bevameter and a manually powered field-focused shear strength bevameter were introduced. Both devices were designed and constructed based on a comprehensive review of existing bevameter literature. The automated laboratory bevameter can conduct both bevameter tests (pressure-sinkage and shear strength) in a controlled manner and the field-focused shear strength bevameter is designed for field shear strength sampling. The field-focused shear strength bevameter was first tested in the laboratory for repeatability. Nine replicate measurements of shear stress versus angular displacement showed general agreement, as did the cohesion and friction angle values fit from the corresponding shear stress at failure versus normal stress data. Results from the field-focused shear strength bevameter were also compared to traditional geotechnical shear strength tests for validation. Friction angle and cohesion values were

shown to agree with values measured in direct shear and CU triaxial testing in an unsaturated and saturated state.

The bevameter devices should be further tested and evaluated in the laboratory. First, the laboratory bevameter should be validated in a similar manner to the evaluation of the field-focused shear strength bevameter in this study. Repeatability should be examined, and shear testing should be compared to geotechnical strength parameters. Pressure-sinkage test results should also be compared to traditional geotechnical compressibility measurements. Various testing variables and their respective effects on bevameter shear testing should also be examined, including shearing rate, grouser depth, applied normal stresses, and number of grousers. The effects of sinkage rate and plate diameter on pressure-sinkage results should also be examined. As part of the laboratory evaluation of these devices, a comprehensive database of soil strength parameters paired with soil texture, Atterberg limits, water retention parameters, and other relevant soil properties should be developed. Finally, a field-focused pressure-sinkage bevameter should also be designed, constructed, and validated.

4.7 Tables and Figures

Table 4.1. Pressure-sinkage literature values and CSU bevameter design parameters. Note that the minimum, mean, and maximum corresponding to the plate diameter/side length column considers both side length of rectangular plates and diameter of circular plates. Either dimension can be used as the "characteristic dimension" in the Bekker-Wong pressure-sinkage equation.

Data Source	Plate Shape	Plate Diameter/Side Length (cm)	Max Applied Load (N)	Cylinder Stroke/ Allowable Sinkage (cm)	Penetration Rate (cm/s)
Wills 1964	nr	nr	4450	nr	0.151
Liston et al. 1966	Circular	5.08	489	15.2	2.54
Hegedus and Liston 1966	Rectangular	2.54 x 11.4, 5.0 x 22.9	nr	nr	nr
Spanksi 1966	nr	nr	2220	15.2	nr
Dwyer et al. 1974	Circular	20.0, 25.0	14700	nr	nr
Wong 1980	Circular	5.00, 7.50, 10.0	8000	30	nr
Wong et al. 1984	Circular	5.00, 7.50	600	nr	nr
Apfelbeck et al. 2011	Circular	2.54, 5.08, 7.62	nr	nr	0.048, 0.240, 0.480
Apfelbeck et al. 2011	Rectangular	1:1, 1:3, 1:5, 1:7	nr	nr	0.48
Edwards et al. 2017	Circular	7.62, 12.6	500	nr	0.1
Minimum	-	2.54	500	15.2	0.048
Mean	-	9.25	4423	20.1	0.58
Maximum	-	25.0	14700	30.0	2.54
Lab.-Focused Device Parameters	**Circular**	**5.08, 7.62, 10.2, 15.2**	**3600**	**20**	**Max - 33.3**

nr = not reported

Table 4.2. Shear testing literature values and CSU bevameter design parameters

Data Source	Outer Radius (cm)	Inner Radius (cm)	Grouser Depth (mm)	Number of Grousers	Shearing Rate (rpm)	Max Applied Normal Load (N)	Max Applied Torque (Nm)
Wills 1964	nr	nr	nr	nr	1.20	nr	288
Janosi and Hanamoto 1961	8.90	7.00	nr	nr	10.0	nr	nr
Liston et al. 1966	9.30	6.40	nr	nr	nr	nr	nr
Dwyer et al. 1974	30.0	20.0	25	25	nr	10000	600
Wong 1980	34.0	27.0	2.50, 10.0	12, 24	nr	1100	822
Apfelbeck et al. 2011	15.0	5.00, 10.0	2.00, 5.00, 7.50, 10.0	6, 8, 12	0.10, 0.20, 0.30	30	1.7
Edwards et al. 2017	34.0	27.0	15.0	24	0.5	500	nr
Minimum	8.90	6.40	2.50	6	0.10	30	1.7
Mean	21.9	14.6	9.62	16	2.05	2908	428
Maximum	34.0	27.0	25.0	25	10.0	10000	822
Lab.-Focused Device Parameters	**15.2**	**10.2**	**19**	**12**	**Max - 70.9**	**3600**	**280**
Field-Focused Device Parameters	**15.2**	**10.2**	**19**	**12**	**Max - 15**	**3600**	**200**

nr = not reported

Table 4.3. Mechanical and electrical laboratory-focused bevameter components with comparison to target parameters

Device	Bevameter Component	Function	Capacity	Desired Capacity
Laboratory-focused bevameter	Parker ETH032M05 Linear Actuator	Vertical force application	3600 N	3600 N
		Stroke	20 cm	20 cm
	Parker BE343J Electric Motor	Torque application	12.05 Nm	280 Nm
	Carson Eliminator 70:1 Planetary Gearbox	Increase torque of motor by a factor 70	Increases maximum motor output to 844 Nm	280 Nm
	Interface 2816 2-axis Torsion Load Cell	Vertical force measurement	22240 N	3600 N
		Torque measurement	339 Nm	280 Nm
	Omega LDI-128 LVIT	Vertical displacement measurement	25 cm	20 cm
Field-focused shear strength bevameter	Interface TS12 Shaft Style Reaction Torque Transducer	Torque measurement	200 Nm	200 Nm

Table 4.4. Laboratory soil properties

Soil Property	ASTM Method	Filter Sand
USCS Classification	D 2487 – 17	SM
USDA Classification	N/A	Sand
Liquid Limit	D 4318 – 17e1	N/A
Plastic Limit	D 4318 – 17e1	N/A
Specific Gravity	D 854 – 14	2.73
Max. dry unit weight (kN/m^3)	D 689 – 12e2	16.3
Target dry unit weight (kN/m^3)	N/A	13.8

N/A = Not Applicable

Table 4.5. Target volumetric water content (θ) and gravimetric water content (w) for Filter Sand shear strength testing at corresponding values of saturation (S)

$S = 25\%$		$S = 100\%$	
θ	w	θ	w
12%	8.6%	48%	34%

Table 4.6 Bevameter and geotechnical shear strength comparison for Filter Sand

	$S = 25\%$						$S = 100\%$					
	c (kPa)			ϕ (°)			c (kPa)			ϕ (°)		
	Min.	Mean	Max.	Min.	Mean	Max.	Min.	Mean	Max.	Min.	Mean	Max.
Direct Shear	5.96	7.03	8.14	30.5	31.8	33.6	1.84	2.61	3.38	34.9	35.2	35.6
CU Triaxial	N/A						N/A	0	N/A	N/A	27.1	N/A
Bevameter	3.98	5.93	8.02	18.2	22.8	25.6	3.80	4.81	6.19	21.8	26.5	28.9

N/A = Not Applicable

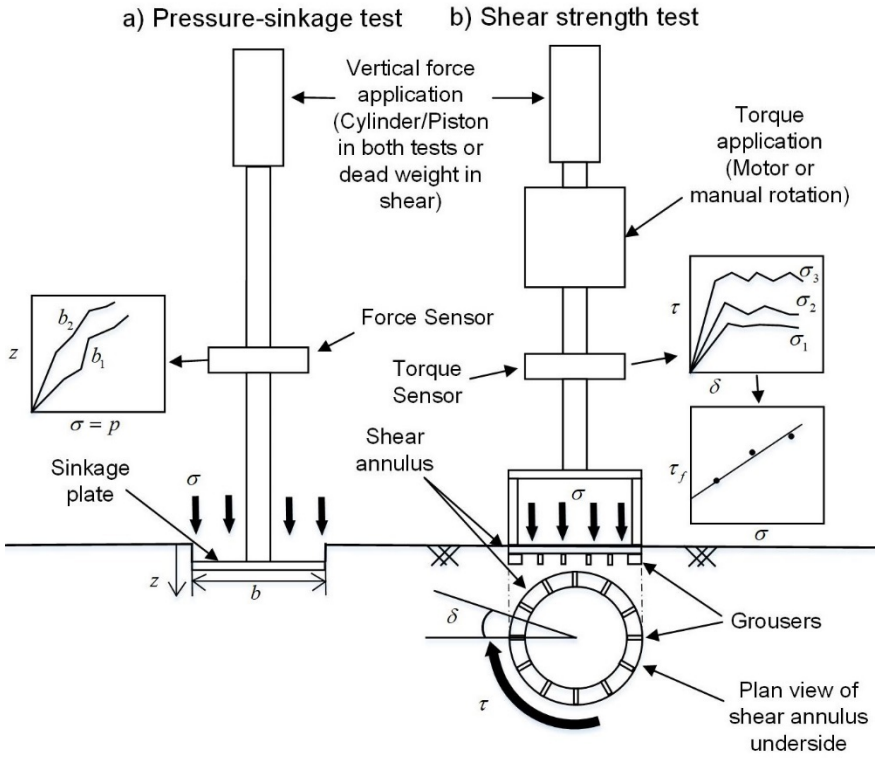

Fig. 4.1. Bevameter operational schematic including (a) profile view of pressure-sinkage test procedure, (b) profile view of shear strength test procedure

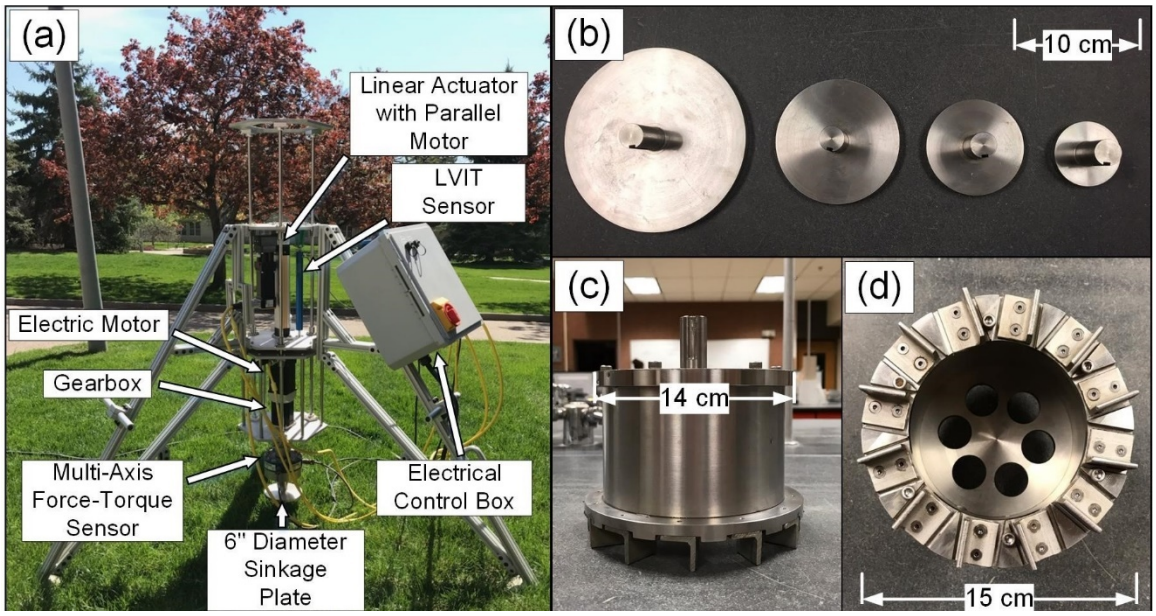

Fig. 4.2. Laboratory bevameter device and testing plates including (a) laboratory bevameter device (b) pressure sinkage plates, (c) shear annulus side view, (d) shear annulus bottom with grousers

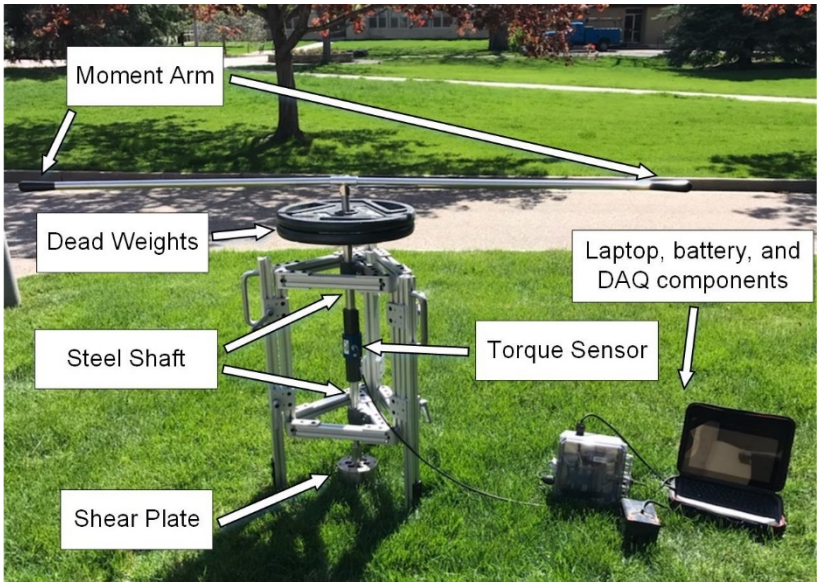

Fig. 4.3. Field-focused shear strength bevameter with laptop and data acquisition (DAQ) components

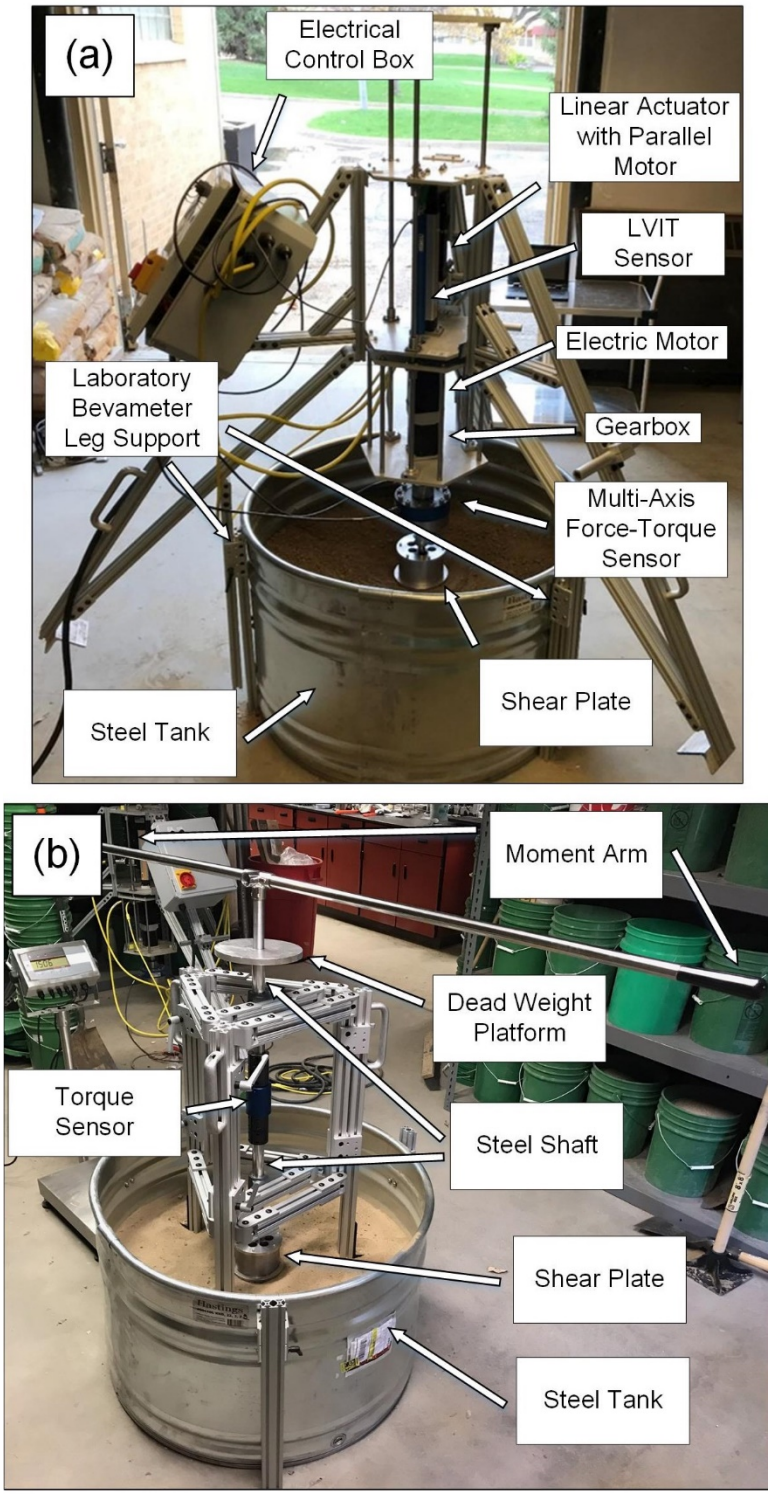

Fig. 4.4. Bevameter laboratory testing setup including (a) laboratory-focused bevameter elevated above the testing tank to align testing plate with soil surface, and (b) field-focused shear strength bevameter shear device placed atop soil surface

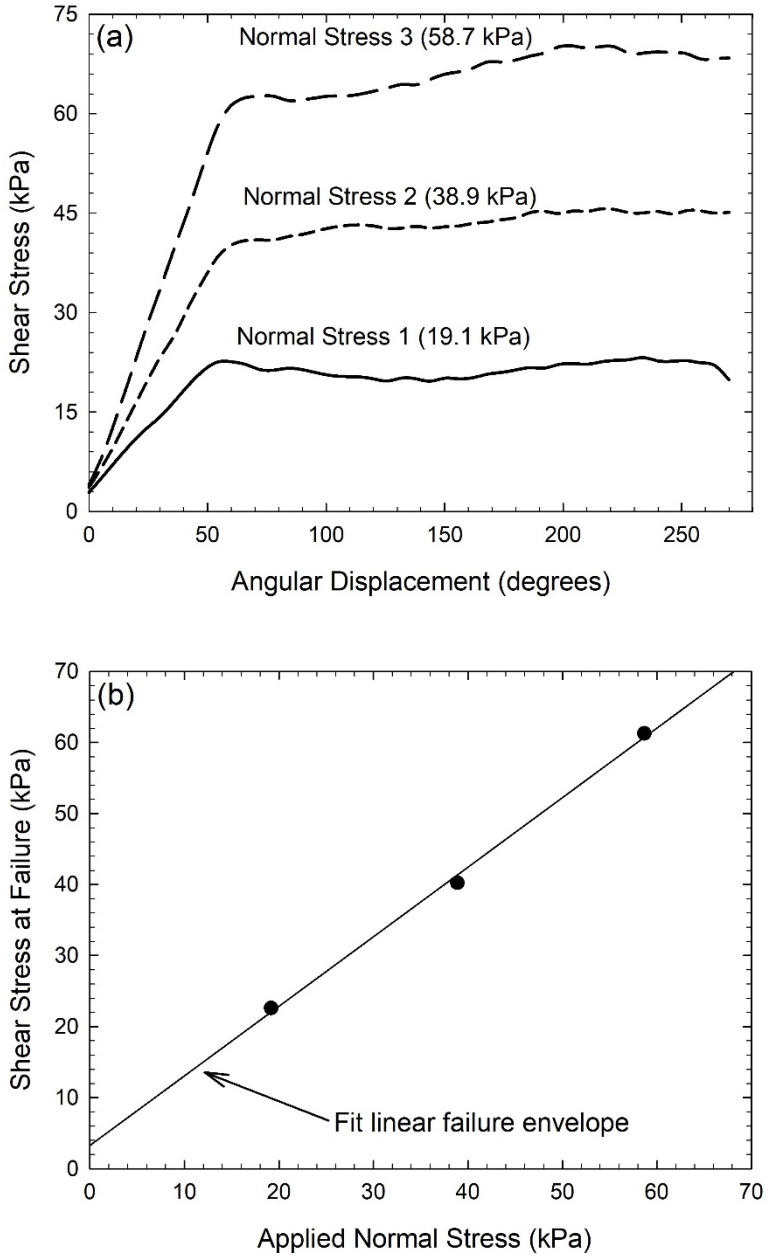

Fig. 4.5. Example bevameter shear data for (a) shear stress versus angular displacement at three normal stresses, and (b) shear stress at failure versus applied normal stress with linear fit (Mohr-Coulomb failure envelope)

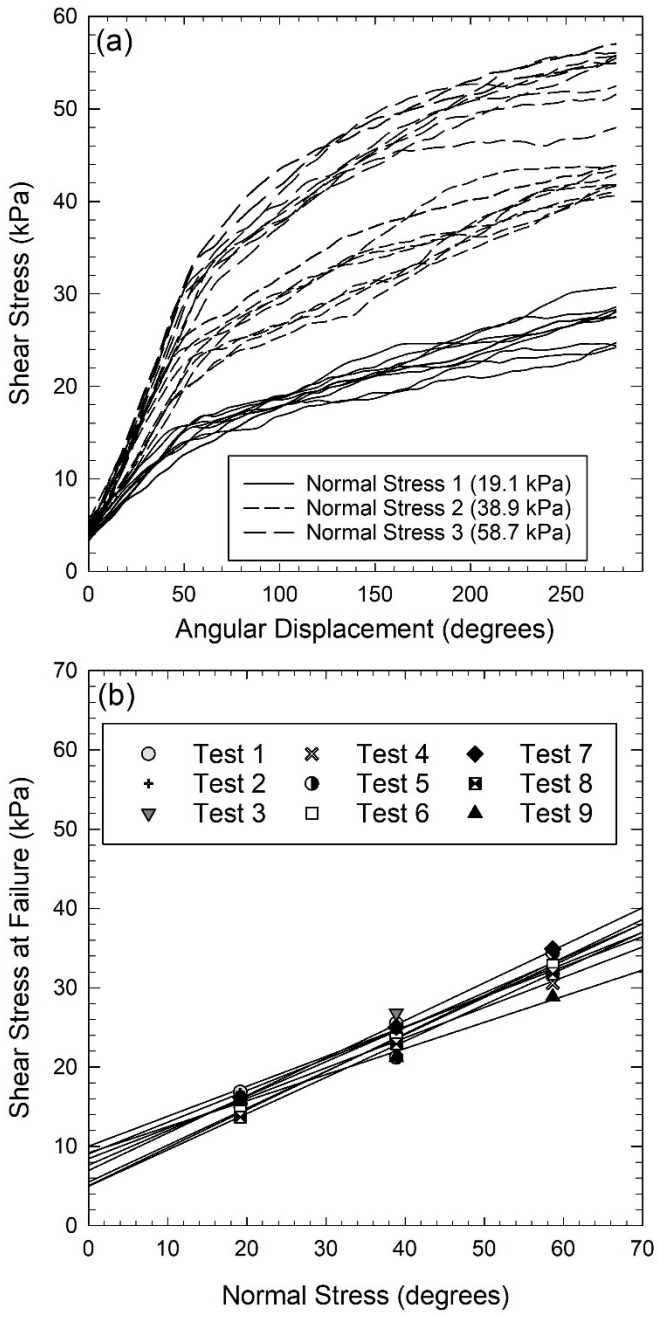

Fig. 4.6. Field-focused shear strength bevameter repeatability results. Plots of (a) shear stress versus angular displacement and (b) shear stress at failure versus normal stress are shown for nine replicate measurements on Filter Sand at $S = 25\%$. Linear Mohr-Coulomb fits are shown in (b).

REFERENCES

Ahlvin, R.B., P.W. Haley. 1992. NATO Reference Mobility Model, Edition II user's guide. Technical Report GL-92-19, US Army Engineer Waterways Experiment Station, Vicksburg, MS.

Apfelbeck, M., S. Kuss, B. Rebele, B. Schaefer. 2011. A systematic approach to reliably characterize soils based on bevameter testing. J. Terramechanics. 45(5): 360-371. doi:10.1016/j.jterra.2011.04.001

ASTM International. 2011. Standard Test Methods for Consolidated Undrained Triaxial Compression Test for Cohesive Soils. ASTM D4767-11. West Conshohocken, PA: ASTM International, 2011. doi:10.1520/ D4767-11

ASTM International. 2011. Standard Test Methods for Direct Shear Test of Soils Under Consolidated Drained Conditions. ASTM D3080/D3080M-11. West Conshohocken, PA: ASTM International, 2011. doi:10.1520/ D3080_D3080M-11

ASTM International. 2012. Standard Test Methods for Laboratory Compaction Characteristics of Soil Using Standard Effort (12,400 ftlbf/ft^3 (600 kN-m/m^3)). ASTM D698-12e2. West Conshohocken, PA: ASTM International, 2012. doi:10.1520/D0698-12e2

ASTM International. 2014. Standard Test Methods for Specific Gravity of Soil Solids by Water Pycnometer. ASTM D854-14. West Conshohocken, PA: ASTM International, 2014. doi:10.1520/D0854-14

ASTM International. 2017. Standard Practice for Classification of Soils for Engineering Purposes (Unified Soil Classification System). ASTM D2487-17. West Conshohocken, PA: ASTM International, 2017. doi:10.1520/D2487-17

ASTM International. 2017. Standard Test Methods for Liquid Limit, Plastic Limit, and Plasticity Index of Soils. ASTM D4318-17e1. West Conshohocken, PA: ASTM International, 2017. doi:10.1520/D4318-17e1

Atkinson, J.H., D.M. Farrar. 1985. Stress path tests to measure soil strength parameters for shallow landslips. Proc., 11th Inf. Conf. on Soil Mechanics and Foundation Engineering, San Francisco, CA, 983-986.

Bandara, R., J.P. Walker, C. Ruediger. 2014. Towards soil property retrieval from space: Proof of concept using in situ observations. J. Hydrology. 512: 27-38. doi: 10.1016/j.hydrol.2014.02.031.

Bareither, C.A., C.H. Benson, T.B Edil. 2008. Reproducability of direct shear tests conducted on granular backfill materials". Geotech Test J. 31(1): 1-11. doi:10.1520/GTJ100878

Bartsch, A., H. Balzter, and C. George. 2009. The influence of regional surface soil moisture anomalies on forest fires in Siberia observed from satellites. Environ. Res. Lett. 4(4). doi: 10.1088/1748-9326/4/4/045021

Batjes, N.H. 2016. Harmonized soil property values for broad-scale modeling (WISE30sec) with estimates of global soil carbon stocks. Geoderma. 269: 61-68. doi: 10.1016/j.geoderma.2016.01.034

Bekker, M.G. 1956. Theory of land locomotion: The mechanics of vehicle mobility. The University of Michigan Press, Ann Arbor, Michigan.

Bekker, M.G. 1960. Off-the-road locomotion: Research and development in terramechanics. The University of Michigan Press, Ann Arbor, Michigan.

Bishop, A.W., 1959. The principle of effective stress. Teknisk Ukeblad. 106 (39): 859-863

Bishop, A.W., G.E. Blight. 1963. Some aspects of effective stress in saturated and partly saturated soils. Geotechnique. 13(3): 177-197. doi: 10.1680/geot.1963.13.3.177

Bishop, A.W., D.L. Webb, P.I. Lewin. 1965. Undisturbed samples of London Clay from the Ashford Common Shaft: Strength-effective stress relationships. Geotechnique. 15(1): 1-31. doi: 10.1680/geot.1965.15.1.1

Brocca, L., F. Melone, T. Moramarco, M. Stelluti. 2004. Soil water content monitoring in an experimental basin in Central Italy. In: Proceedings of the International Conference ERB2004 Euromediterranean Conference, Torino, 18-21.

Brooks, R.H, and A.T. Corey. 1964. Hydraulic properties of porous media. Hydrology Papers. Colorado State University, Ft. Collins, CO.

Busch, F.A., J.D. Niemann, and M. Coleman. 2012. Evaluation of an empirical orthogonal function-based method to downscale soil moisture patterns based on topographical attributes. Hydrol. Process. 26(18): 2696-2709. doi: 10.1002/hyp.8363

Campbell, G.S. 1974. A simple method for determining unsaturated conductivity from moisture retention data. Soil Sci. 117(6): 311-314.

Chandler, D.G., M.S. Seyfried, J.P. McNamara, K. Hwang. 2017. Inference of soil hydrologic parameters from electronic soil moisture records. Frontiers in Earth Science. 5: 1-17. doi: 10.3389/feart.2017.00025.

Chauhan, N.S., S. Miller, P. Ardanuy. 2003. Spaceborne soil moisture estimation at high resolution: a microwave-optical/IR synergistic approach. Int. J. Remote Sens. 24(22): 4599-4622. doi: 10.1080/0143116031000156837

Choi, K.K., N. Gaul, P. Jayakumar, T.M. Wasfy. 2018. Framework of reliability-based stochastic mobility map for Next Generation NATO Reference Mobility Model. Proceedings of the 2018 Ground Vehicle Systems Engineering and Technology Symposium, Novi, MI.

Coleman, M.L., and J.D. Niemann. 2013. Controls on topographic dependence and temporal instability in catchment-scale soil moisture patterns. Water Resour. Res. 49(3): 1625-1642. doi: 10.1002/wrcr.20159

Cosby, B.J., G.M. Hornberger, R.B. Clapp, T.R. Ginn. 1984. A statistical exploration of the relationships of soil-moisture characteristics to the physical properties of soils. Water Resour. Res. 20: 682-690. doi:10.1029/WR020i006p00682

Coulomb, C.A. 1776. Essai sur une application des regles des maximis et minimis a quelquels problemesde statique relatifs, a la architecture. Mem. Acad. Roy. Div. Sav. 7, 343-387.

Cowley, G.S., J.D. Niemann, T.R. Green, M.S. Seyfried, A.S. Jones, P.J. Grazaitis. 2017. Impacts of precipitation and potential evapotranspiration patterns on downscaling soil moisture in regions with large topographic relief. Water Resour. Res. 53(2): 1553-1574. doi:10.1002/2016WR019907

Crow, W.T., E.F. Wood, R. Dubayah. 2000. Potential for downscaling soil moisture maps derived from spaceborne imaging radar data. J. Geophys. Res.-Atmos. 105(D2): 2203-2212. doi: 10.1029/1999JD901010

Das, N.N., D. Entekhabi, E.G. Njoku. 2011. An algorithm for merging SMAP radiometer and radar data for high-resolution soil-moisture retrieval. IEEE Trans Geosci. Remote Sens. 49(5): 1504-1512. doi: 10.1109/TGRS.2010.2089526

Day, R.W., G.W. Axten. 1989. Surficial stability of compacted clay slopes. J. Geotech. Eng., 115(4): 577-580. doi: 10.1061/(ASCE)0733-9410(1989)115:4(577)

Deshon, J.P. 2018. Stochastic analysis and probabilistic downscaling of soil moisture. Master's Thesis, Colorado State University, Fort Collins, CO

Dingman, S.L. 2002. Physical Hydrology. 2nd ed. Prentice Hall, Upper Saddle River, N.J.

Dirmeyer, P.A. 1999. Assessing GCM sensitivity to soil wetness using GSWP data. J. Meteorol. Soc. Jpn. 77(1B): 367-385. doi: 10.2151/jmsj1965.77.1B_367

Downer, C.W., and F.L. Ogden. 2006. Gridded Surface Subsuface Hydrologic Analysis (GSSHA) User's Manual. US Army ERDC/CHL SR-06-1.

Dussaillant, A., K. Cozzetto, K. Brander, K. Potter. 2003. Green-Ampt model of a rain garden and comparison to Richards equation model. WIT Transactions on Ecology and the Environment. 67: 891-900. doi: 10.2495/SPD030841

Dwyer, M.J., D.R. Comely, D.W. Evernden. 1974. The field performance of some tractor tyres related to soil mechanical properties. J. Agric. Engng. Res. 19: 35-50. doi:10.1016/0021-8634(74)90005-5

Edwards, M.B., M.M. Dewoolkar, D.R. Huston, C. Creager. 2017. Bevameter testing on similant fillite for planetary rover mobility applications. J. Terramechanics, 70: 13-26. doi: 10.1016/j.jterra.2016.10.004

Eichinger, W.E., M.B. Parlange, H Stricker. 1996. On the concept of equilibrium evaporation and the value of the Priestley-Taylor coefficient. Water Resour. Res. 32(1): 161-164. doi: 10.1029/95WR02920

Entekhabi, D., E.G. Njoku, P.E. O'Neill, K.H. Kellogg, W.T. Crow, et al. 2010. The Soil Moisture Active Passive (SMAP) Mission. Proc. IEEE. 98(5): 704-716. doi: 10.1109/Jproc.2010.2043918

Fitzjohn, C., J.L. Ternan, A.G. Williams. 1998. Soil moisture variability in a semi-arid gully catchment: implications for runoff and erosion control. Catena. 32(1): 55-70. doi: 10.1016/S0341-8162(97)00045-3

Frankenstein, S., G.G. Koenig. 2004. Fast All-season Soil Strength (FASST). SR-04-1, US Army Corps of Engineers, Washington, D.C.

Fredlund, D.G., N.R. Morgenstern, R.A. Widger. 1978. The shear strength of unsaturated soils. Can. Geotech. J. 15(3): 313-321. doi:10.1139/t78-029

Fredlund, D.G., H. Rahardjo, M.D. Fredlund. 2012. Unsaturated Soil Mechanics in Engineering Practice. John Wiley and Sons, Inc. Hoboken, New Jersey

Garcia-Gaines, R.A., S. Frankenstein, 2015. USCS and the USDA Soil Classification System. TR-15-4, US Army Corps of Engineers Engineer Research and Development Center/Cold Regions Research and Engineering Laboratory, Vicksburg, MS.

Goldsmith, W., M. Silva, C. Fischenich. 2001. Determining optical degree of soil compaction for balancing mechanical stability and plant growth capacity. Technical Report TN-EMRRP-SR-26, US Army Corps of Engineers Engineer Research and Development Center, Vicksburg, MS.

Grayson, R.B., A.W. Western, J.P. Walker, J.P. Kandel, D.G. Costelloe, D.J. Wilson. 2006. Controls on patterns of soil moisture in arid and semi-arid systems. In: P. D'Odorico, A. Porporato, editors, Dryland Ecohydrology. Springer, Dordrecht, Netherlands. p. 109-127

Green, W.H., and G. Ampt. 1911. Studies of soil physics, part I – the flow of air and water through soils. J. of Agric. Sci. 4(1): 1-24. doi:10.1017/S0021859600001441

Green, T.R., G.H. Dunn, R.H. Erskine, J.D. Salas, and L.R. Ahuja. 2009. Fractal analysis of steady infiltrtion and terrain on an undulating agricultural field. Vadose Zone J. 8(2): 310-320. doi: 10.2136/vzj2008.0021

Green, T.R., and R.H. Erskine. 2011. Measurement and inference of profile soil-water dynamics at different hillslope positions in a semiarid agricultural watershed. Water Resour. Res. 47(12). doi: 10.1029/2010WR010074

Greico, N.R., J.D. Niemann, T.R. Green, A.S. Jones, P.J. Grazaitis. 2018. Hydrologic downscaling of soil moisture using global data sets without site-specific calibration. J. Hydrol. Eng. 23(11). doi: 10.1061/(ASCE)HE.1943-5584.0001702

Haley, P.W., M.P. Jurkat, P.M. Brady, 1979. NATO Reference Mobility Model, Edition I user's guide. Technical Report 12503, US Army Tank-Automotive Command, Warren, MI.

Hegedus, E., R.A. Liston. 1966. Recent investigations of vertical load-deformation characteristics of soils. U.S. Army Tank Automotive Center, Technical Report no. 9560, pp. 2-20.

Heimsath, A.M, W.E. Dietrich, K. Nishiizumi, R.C. Finkel. 1999. Geomorphology. 27(1-2): 151-172. doi: 10.1016/S0169-555x(98)00095-6

Huete, A.R. 1988. A soil adjusted vegetation index (SAVI). Remote Sens. Environ. 25(3): 295-309. doi:10.1016/0034-4257(88)90106-X

Hoehn, D.C., J.D. Niemann, T.R. Green, A.S. Jones, P.J. Grazaitis. 2017. Downscaling soil moisture over regions that include multiple coarse-resolution grid cells. Remote Sens. Environ. 199: 187-200. doi: 10.1016/j.rse.2017.07.021

Holzman, M.E., R. Rivas, M.C. Piccolo. 2014. Estimating soil moisture and the relationship with corp yield using surface temperature and vegetation index. Int. J. Appl. Earth Obs. Geoinf. 28: 181-192. doi: 10.1016/j.jag.2013.12.006

Horn, R., and H. Fleige. 2003. A method for assessing the impact of load on mechanical stability and physical properties of soil. Soil Till. Res. 73(1-2): 89-99. doi: 10.1016/S0167-1987(03)00102-8

Hsu, S.M., C.F. Ni, P.F. Hung. 2002. Assessment of three infiltration formulas based on model fitting on Richards equation. J. Hydrol. Eng. 7(5): 373-379. doi: 10.1061/(ASCE)10840699(2002)7:5(373)

Huisman, J.A., C. Sperl, W. Bouten, J.M. Verstraten. 2001. Soil water content measurements at different scales: accuracy of time domain reflectometry and ground-penetratig radar. J Hydrology. 245: 48-58. doi: 10.1016/S0022-1694(01)00336-5

Hunt, H., R. Gilkes. 1992. Farm Monitoring Handbook. The University of Western Australia, Nedlands, Western Australia.

Janosi, Z., B. Hanamoto. 1961. The analytical determination of drawbar pull as a function of slip lot tracked vehicles in deformable soils. 1st Int Conf. on Mechanics of Soil-Vehicle Systems 44: 708-736.

Jennings, J.E.B., J.B. Burland, 1962. Limitations to the use of effective stress in partly saturated soils. Geotechnique. 12(2): 125-144. doi:10.1680/geot.1962.12.2.125

Johnson, A.W., J.R. Sallberg. 1962. Factors influencing compaction test results. Highway Research Board Bulletin 319, National Academy of Sciences – National Research Council, Washington, D.C.

Jurkat, M.P., C.J. Nuttall, P.W. Haley. 1975. The U.S. Army Mobility Model (AMM-75), in: Siorek, R.W. (Ed.), Proceedings of the U.S. Army/FRG Army Mobility Symposium. US Army Tank-Automotive Command, Warren, MI. pp. 2-50.

Karafiath, L. L., E. A. Nowatzki,. 1978. Soil Mechanics for Off-Road Vehicle Engineering. Series on Rock and Soil Mechanics, Vol. 2 (1974/77) No. 5, Trans Tech Publications, Clausthal, Germany.

Kerr, Y.H., P. Waldteufel, J. Wigneron, S. Delwart, F. Cabot, et al. 2010. The SMOS mission: New tool for monitoring key elements of the global water cycle. P. IEEE. 98(5): 666-687. doi: 10.1109/Jproc.2010.2043032

Khalili, N, F. Geiser, G.E. Blight. 2004. Effective stress in unsaturated soils: review with new evidence. Int. J. Geomech. 4(2), 115-126. doi: 10.1061/(ASCE)1532-3641(2004)4:2(115)

Khalili, N., M.H. Khabbaz. 1998. A unique relationship for χ for the determination of the shear strength of unsaturated soils. Geotechnique. 48(5): 681-687. doi: 10.1680/geot.1998.48.5.681

Kim, G., A.P. Barros. 2002. Downscaling of remotely sensed soil moisture with a modified fractal interpolation method using contraction mapping and ancillary data. Remote Sens. Environ. 83(3): 400-413. doi: 10.1016/S0034-4257(02)00044-5

Knight, S.J. 1956. A summary of trafficability studies through 1955. Technical Memorandum No. 3-240, 14th supplement. U.S. Army Engineer Waterways Experiment Station, Vicksburg, MS.

Laio, F., A. Porporato, L. Ridolfi, I. Rodriguez-Iturbe. 2001. Plants in water-controlled ecosystems: active role in hydrologic processes and response to water stress II. Probabilistic soil moisture dynamics. Adv. Water Resour. 24(7): 707-723. doi: 10.1016/S0309-1708(01)00004-5

Liston, R.A., T. Czako, P. Haley, W.L. Harrison, Jr., B. Hanamoto, L. Martin. 1966. Mobility Environmental Research Study Mobility Testing Procedures. U.S. Army Materiel

Command for U.S. Army Waterways Experiment Station, Land Locomotion Laboratory, U.S. Army Tank-Automotive Center, Vicksburg, MS:

Liston, R. A. 1973. The Combined Normal and Tangential Loading of Soil. Ph.D. Thesis, Michigan Technical University

Lowry, W.D. 1959. The falling rate phase of evaporative soil-moisture loss – A critical evaluation. Bull. Am. Meteorol. Soc. 40(12): 605-608. doi: 10.1175/1520-0477-40.12.605

Lu, N., J.W. Godt, D.T. Wu, 2010. A closed-form equation for effective stress in unsaturated soil. Water Resour. Res. 46(5): W05515. doi:10.1029/2009WR008646

Lu, N., W.J. Likos. 2004. Unsaturated soil mechanics. John Wiley and Sons, Inc., Hoboken, New Jersey.

Lu, N., W.J. Likos. 2006. Suction stress characteristic curve for unsaturated soil. J. Geotech. Geonviron. 132(2): 131-142. doi:10.1061/(ASCE)1090-0241(2006)132:2(131)

Luckner, L., M.Th. van Genuchten, D.R. Nielsen. 1989. A consistent set of parametric models for the two-phase flow of immiscible fluids in the subsurface. Water Resour. Res. 25(10): 2187-2193.

Maccarini, M. 1993. A comparison of direct shear box tests with triaxial compression tests for a residual soil. Geotechnical and Geological Engineering. 11(2): 69-80. doi:10.1007/BF00423336

Mascaro, G., E.R. Vivoni, R. Deidda. 2011. Soil moisture downscaling across climate regions and its emergent properties. J. Geophys. Res.-Atmos. 116. doi: 10.1029/2011JD016231

Mason, G.T., R.B. Ahlvin, J. Green, 2001. Short-Term Operational Forecasts of Trafficability (SOFT). Technical Report-01-022, US Army Corps of Engineers Engineering Research and Development Center/Geotechnical and Structures Laboratory, Vicksburg, MS.

McCullough, M., P. Jayakumar, J. Dasch, D. Gorsich. 2017. The Next Generation NATO Reference mobility model development. J. Terramechanics. 73: 49-60. doi:10.1016/j.jterra.2017.06.002

McCutcheon, M.C., H.J. Farahani, J.D. Stednick, G.W. Buchleter, T.R. Green. 2006. Effect of soil water on apparent soil electrical conductivity and texture relationships in a dryland field. Biosys. Eng. 94(1): 19-32. doi:10.1016/j.biosystemseng.2006.01.002

Merlin, O., A.G. Chehbouni, Y.H. Kerr, E.G. Njoku, D. Entekhabi. 2005. A combined modeling and multispectral/multiresolution remote sensing approach for disaggregation of surface soil moisture: application to SMOS configuration. IEEE Trans. Geosci. Remote Sens. 43(9): 2036-2050. doi: 10.1109/TGRS.2005.853192

Merlin, O., A.G. Chebouni, Y.H. Kerr, D.C. Goodrich. 2006. A downcaling method for distributing surface soil moisture within a microwave pixel: application to the Monsoon '90 data. Remote Sens Environ. 101(3): 379-389. doi: 10.1016/j.rse.2006.01.004

Mitas, L., H. Mitasova. 1988. General variation approach to the interpolation problem. Computers and Mathematics with Applications. 16(12): 983-992. doi: 10.1016/0898-1221(88)90255-6

Mohr, O., 1900. Welche Umstaende bedingen die Elistizitaetsgrenze und den Bruch eines Materiales? Zeitschrift des Vereines Deutscher Ingenieure. 44: 1524-1530, 1572-1577

Nash, J.E., J.V. Sutcliffe. 1970. River flow forecasting through conceptual models part I – A discussion of principles. J. Hydrol. 10(3): 282-290. doi:10.1016/0022-1694(70)90255-6

Nitao, J.J., J. Bear. 1996. Potentials and their role in transport in porous media. Water Resour. Res. 32(2): 225-250. doi: 10.1029/95WR02715.

Njoku, E.G., T.J. Jackson, V. Lakshmi, T.K. Chan, S.V. Nghiem. 2003. Soil moisture retrieval from AMSR-E. IEEE T. Geosci. Remote. 41(2): 215-229. doi: 10.1109/Tgrs.2002.808243

Oh, S., N. Lu, Y.K. Kim, S.J. Lee, S.R. Lee. 2012. Relationship between the soil-water characteristic curve and the suction stress characteristic curve: experimental evidence from residual soils. J. Geotech. Geoenviron. 138(1), 47-57. doi:10.1061/(ASCE)GT.1943-5606.0000564

Pellenq, J., J. Kalma, G. Boulet, G.M. Saulnier, S. Wooldridge, et al. 2003. A disaggregation scheme for soil moisture based on topography and soil depth. J. Hydrol. 276(1-4): 112-127. doi: 10.1016/S0022-1694(03)00066-0

Peng, J., A. Loew, S. Zhang, J. Wang, J. Niesel. 2016. Spatial downscaling of satellite soil moisture data using a vegetation temperature condition index. IEEE Trans. Geosci. Remote Sens. 54(1): 558-566. doi: 10.1109/TGRS.2015.2462074

Penman, A.D.M, 1953. Shear characteristics of a saturated silt, measured in triaxial compression. Geotechnique. 3(8): 312-328. doi:10.1680/geot.1953.3.8.312

Phillips, A.J., N.K. Newlands, S.H.L. Liang, B.H. Ellert. 2014. Integrated sensing of soil moisture at the field-scale: Measuring, modeling, and sharing for improved agricultural decision support. Comput. Electron. Agr. 107:73-88. doi: 10.1016/j.compag.2014.02.011

Porporato, A., F. Laio, L. Ridolfi, I. Rodriguez-Iturbe. 2001. Plants in water-controlled ecosystems: active role in hydrologic processes and response to water stress III. Vegetation water stress. Adv. Water Resour. 24(7): 725-744. doi: 10.1016/S0309-1708(01)00006-9

Priestley, C.H.B., R.J. Taylor. 1972. Assessment of surface heat-flux and evaporation using large-scale parameters. Mon. Weather Rev. 100(2): 81-92. doi:10.1175/1520-0493(1972)100<0081:OTAOSH>2.3.CO;2

Ranney, K.J., J.D. Niemann, B.M. Lehman, T.R. Green, A.S. Jones. 2015. A method to downscale soil moisture to fine resolutions using topographic, vegetation and soil data. Adv. Water Resour. 76: 81-96. doi: 10.1016/j.advwatres.2014.12.003

Rawls, W.J., and D.L. Brakensiek. 1985. Prediction of soil water properties for hydrologic modeling. In: Watershed Management in the Eighties, Denver, CO. p. 293-299

Reece, A.R. 1964. Problems of soil vehicle mechanics. Technical Report 8479, US Army Land Locomotion Laboratory, US Army Tank-Automotive Command, Warren, MI.

Rula, A.A., C.J. Nuttall Jr., 1971. An analysis of ground mobility models (ANAMOB). Technical Report M-71-4, U.S. Army Engineer Waterways Experiment Station, Vicksburg, MS

Reichle, R.H., G.J.M. De Lannoy, Q. Liu, R.D. Koster, J.S. Kimball, et al. 2017. Global assessment of the SMAP level-4 surface and root-zone soil moisture product using assimilation diagnostics. J. Hydrometerol. 18(12): 3217-3237. doi:10.1175/JHM-D-17-0130.1

Schaap, M.G., F.J. Leij, M.Th. van Genuchten. 2001. ROSETTA: a computer program for estimating soil hydraulic parameters with hierarchical pedotransfer functions. J. Hydrol. 251(3-4): 163-176. doi:10.1016/S0022-1694(01)00466-8

Scharffenberg, W. 2016. Hydrologic Modeling System HEC-HMS User's Manual. US Army Corps of Engineers Hydrologic Engineering Center Computer Program Document-74A

Schoener, G., M.C. Stone. 2019. Impact of antecedent soil moisture on runoff from a semiarid catchment. J. Hydrology. 569: 627-636. doi:10.1016/j.jhydrol.2018.12.025.

Seuffert, G., P. Gross, C. Simmer, E.F. Wood. 2002. The influence of hydrologic modeling on the predicted local weather: Two-way coupling of a mesoscale weather prediction model and a land surface hydrologic model. J. Hydrometerol. 3(5): 505-523. doi:10.1175/1525-7541(2002)003<0505:TIOHMO>2.0.CO;2

Smith, M.H., M.P. Meyer. 1973. Automation of a model for predicting soil moisture and soil strength (SMSP Model). Technical Report AD-755-092, US Army Engineer Waterways Experiment Station, Vicksburg, MS.

Soil Survey Staff. 2018. Soil Survey Geographic (SSURGO) Database for Weld County, CO. USDA-NRCS. http://websoilsurvey.nrcs.usda.gov (accessed 17 June 2018).

Spanski, P. 1966. Portable soil test devices". U.S. Army Tank Automotive Center, Technical Report no. 9560, pp. 242-253.

Song, C.Y., L. Jia, M. Menenti. 2014. Retrieving high-resolution surface soil moisture by downscaling AMSR-E brightness temperature using MODIS LST and NDVI data. IEEE J Sel Top Appl Earth Obs Remote Sens. 7(3): 935-942. doi: 10.1109/JSTARS.2013.2272053

Sullivan, P.M., C.D. Bullock, N.A. Renfroe, M.R. Albert, G.G. Koenig, K. O'Neill. 1997. Soil Moisture Strength Prediction Model version II (SMSP II). Technical Report GL-97-15, US Army Engineer Waterways Experiment Station, Vicksburg, MS.

Superfesky, M.J., G.P Williams, Jr. 1978. Shear strength of surface-mine spoils measured by triaxial and direct shear methods". General Technical Report NE-39*,* U.S. Department of Agriculture, Forest Service, Broomall, PA

Terzaghi, K. 1925. Erdbaummechanik auf bodenphysikalischer grundlage. Deuticke, Leipzig, Germany.

Terzaghi, K. 1936. The shearing resistance of saturated soils and the angle between the planes of shear. Proc. 1st Int. Conf. Soil Mech. 1, 54-56.

Terzaghi, K. 1943. Theoretical Soil Mechanics. John Wiley and Sons, Inc. New York, New York

Terzaghi, K. R.B. Peck, G. Mesri, 1996. Soil Mechanics in Engineering Practice. John Wiley and Sons, Inc. New York, New York

United States Bureau of Reclamation, 1998. Earth Manual Part I. US Bureau of Reclamation Earth Sciences and Research Laboratory, Denver, CO.

United States Department of Agriculture, 1981. Transportation Engineering Handbook, Region 1 Supplement 11. U.S. Department of Agriculture, Forest Service, Northern Region, Missoula, MT.

United States Department of Agriculture, 1994. Slope Stability Reference Guide for National Forests in the United States, Volume II. U.S. Department of Agriculture, Forest Service EM-7170-13, Washington, D.C.

United States Naval Facilities Engineering Command (NAVFAC), 1986. Foundations and earth structures design manual 7.02. US NAVFAC, Alexandria, VA.

van Genuchten, M.Th. 1980. A closed-form equation for predicting the hydraulic conductivity of unsaturatedsoils. Soil Sci. Soc. Am. J. 44: 892-898.doi:10.2136/sssaj1980.03615995004400050002x

van Genuchten, M.Th., F.J. Leij, and S.R. Yates. 1991. The RETC code for quantifying the hydraulic functions of unsaturated soils. U.S. Salinity Lab, U.S. Dept. of Agriculture, Agricultural Research Service. Riverside, CA.

Vanapalli, S.K., D.G. Fredlund, D.E. Pufahl, A.W. Clifton. 1996. Model for the prediction of shear strength with respect to soil suction. Can. Geotech. J. 33: 379-392. doi:org/10.1139/t96-060

Vanapalli, S.K., W.S. Sillers, M.D. Fredlund. 1998. The meaning and relevance of residual state to unsaturated soils. In: Proceedings of 51st Canadian Geotechnical Conference, Edmonton, Alberta. p. 101-108

Vanapalli, S.K., D.G. Fredlund, 2000. Comparison of different procedures to predict unsaturated soil shear strength. Proceedings of the GeoDenver 2000 Conference, ASCE, Denver, CO. pp. 3-8. doi: 10.1061/40510(287)13

Vaunat, J., E. Romero, C. Marchi, C. Jommi. Modeling the shear strength of unsaturated soils. In: Unsaturated Soils, Swets and Zeitlinger, Lisse, Netherlands

Walker, J.P., G.R. Willgoose, J.D. Kalma. 2001. The Nerrigundah data set: Soil moisture patterns, soil characteristics, and hydrological flux measurements. Water Resour. Res. 37(11): 2653-2658. doi:10.1029/2001WR000545

Wei, L., B. Zhang, M. Wang. 2007. Effects of antecedent soil moisture on runoff and soil erosion in alley cropping systems. Agric. Water Manag. 94(1-3): 54-62. doi: 10.1016/j.agwat.2007.08.007.

Werbylo, K.L., J.D. Niemann. 2014. Evaluation of sampling techniques to characterize topographically-dependent variability for soil moisture downscaling. J. Hydrology. 516:304-326. doi: 10.1016/j.jhydrol.2014.01.030

Western, A.W., R.B. Grayson. 1998. The Tarrawarra data set: Soil moisture patterns, soil characteristics, and hydrological flux measurements. Water. Resour. Res. 34(1): 2765-2768. doi:10.1002/(SICI)1099-1085(19990415)13:5<633::AID-HYP770>3.0.CO;2-8.

Wijewardana, C., K.R. Reddy, F.A. Alsajri, J.T. Irby, J. Krutz, B. Golden. 2018. Quantifying soil moisture deficit effects on soybean yield and yield component distribution patterns. Irrigation Sci. 36(4-5): 241-255. doi: 10.1007/s00271-018-0580-1

Williams, J.M., F. Vahedifard, G.L. Mason, I.L. Howard, A. Borazjani, J.D. Priddy. 2017. Expansion and application of database records for off-road vehicle environments

(DROVE). Proceedings of Integrated Virtual NATO Vehicle Development, Applied Vehicle Technology Panel (AVT), STO-MP-AVT-265, Vilnius, Lithuania.

Wills, B.D.M. 1964. The design and development of a hydraulic bevameter. J. Terramechanics. 1(1), 91-97. doi:10.1016/0022-4898(64)90125-9

Wilson, D.J., A.W. Western, R.B. Grayson. 2005. A terrain and data-based method for generating the spatial distribution of soil moisture. Adv. Water Resour. 28(1): 43-54. doi:/10.1016/j.advwatres.2004.09.007.

Wong, J.Y., 1980. Data processing methodology in the characterization of the mechanical properties of terrain. J. Terramechanics. 17(1). 13-41. doi:10.1016/0022-4898(80)90014-2

Wong, J.Y. 2010. Terramechanics and Off-Road Vehicle Engineering. 2nd Ed. Elsevier, Oxford, UK.

Zhang, Y., H. Wei, M.A. Nearing. 2011. Effects of antecedent soil moisture on runoff modeling in small semiarid watersheds of southeastern Arizona. Hydrol. Earth Syst. Sci. 15: 3171-3179. doi: 10.5194/hess-15-3171-2011

Zhang, C., N. Lu. 2019. Generalized effective stress equation for soil. *Manuscript submitted for publication*.

APPENDIX

This appendix contains AutoCAD design drawings prepared for custom-machined components for the laboratory-focused bevameter. All items were constructed by a local machinist in Fort Collins, CO, USA. The items are presented from bottom to top of bevameter, starting with the shear plate components and pressure-sinkage plates and ending with the top guide plate which supports shafts used to ensure linearity in vertical motion.

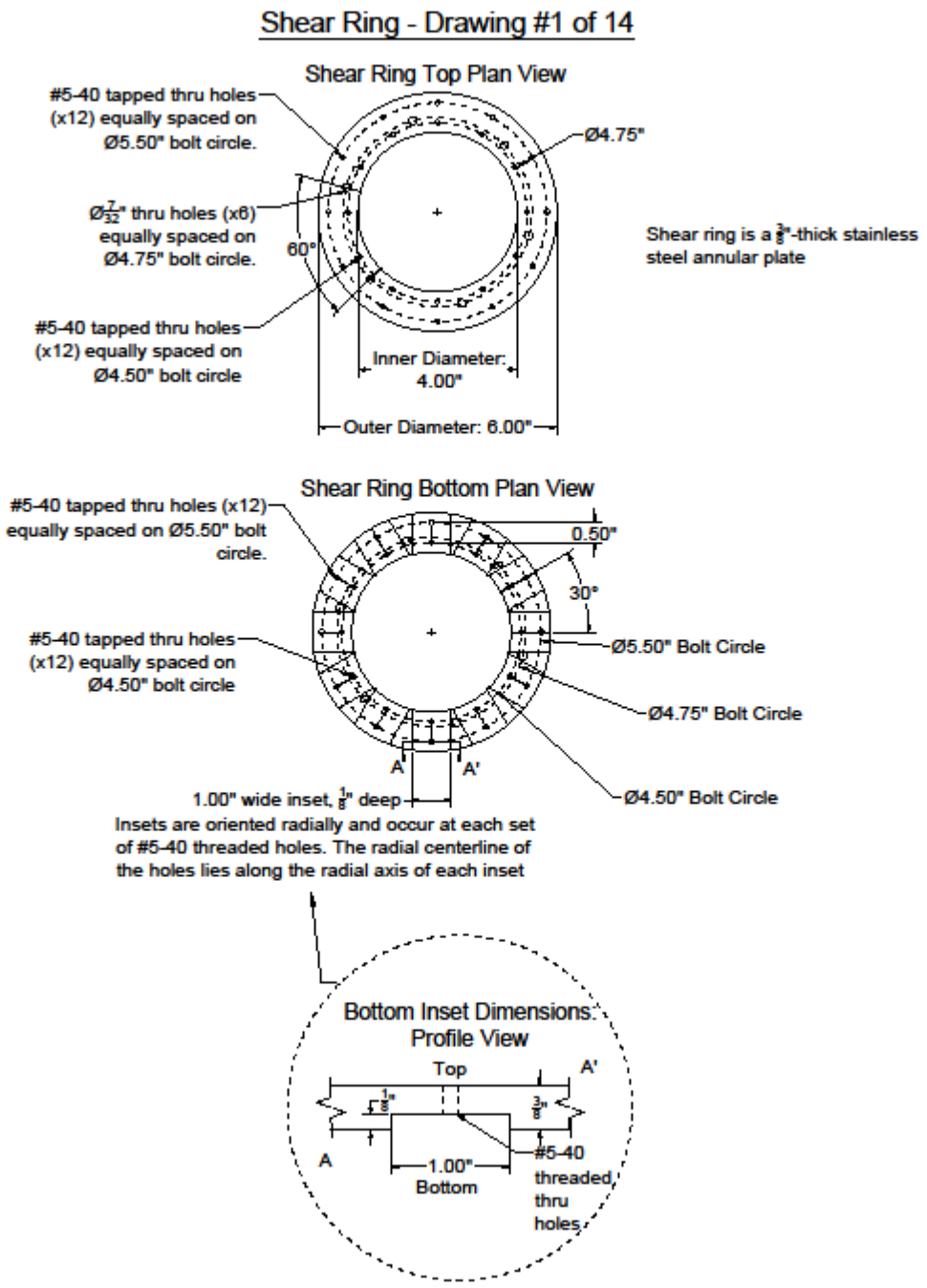

Fig A.1. Shear ring bottom component

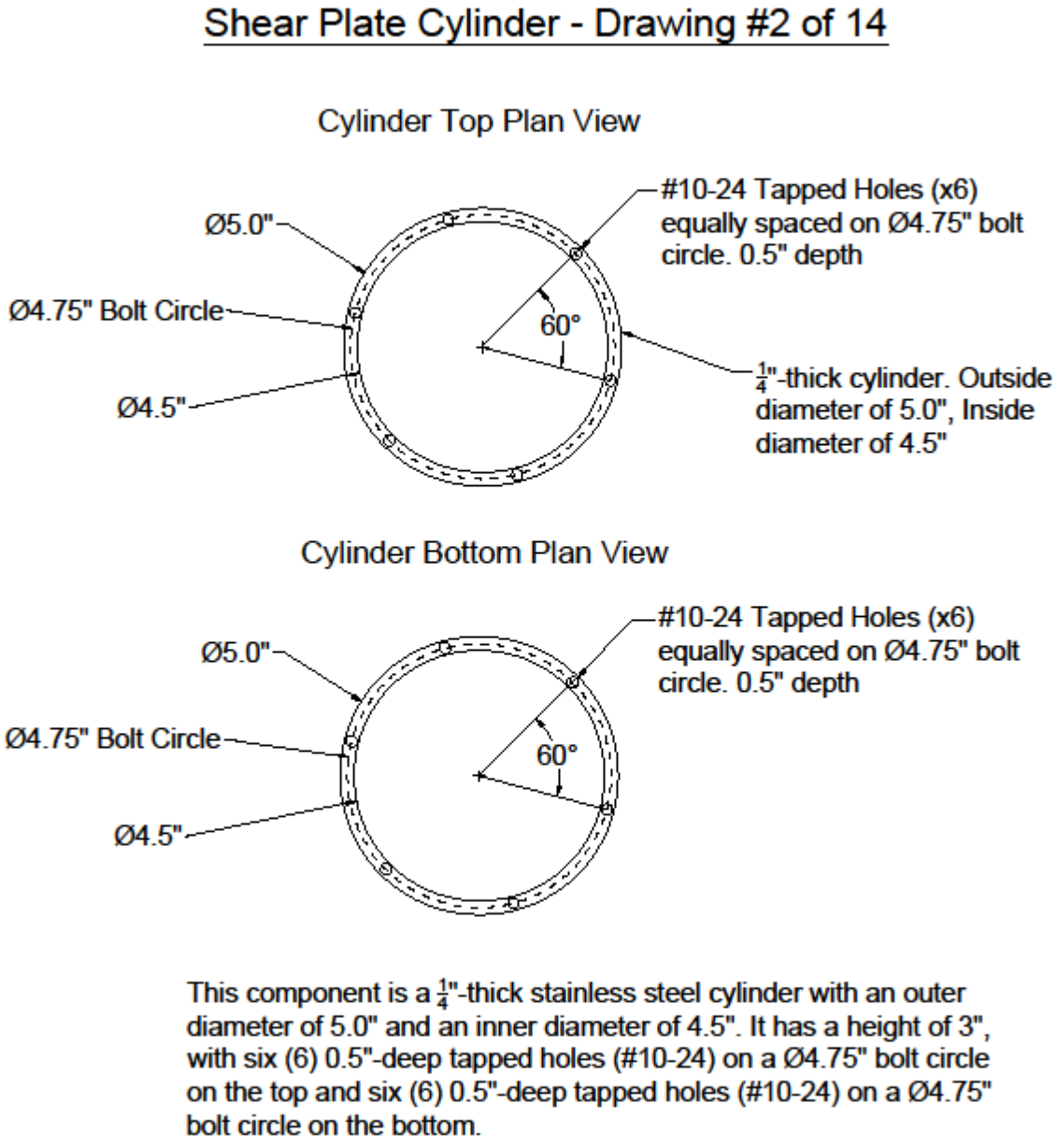

Fig. A.2. Shear ring cylinder component

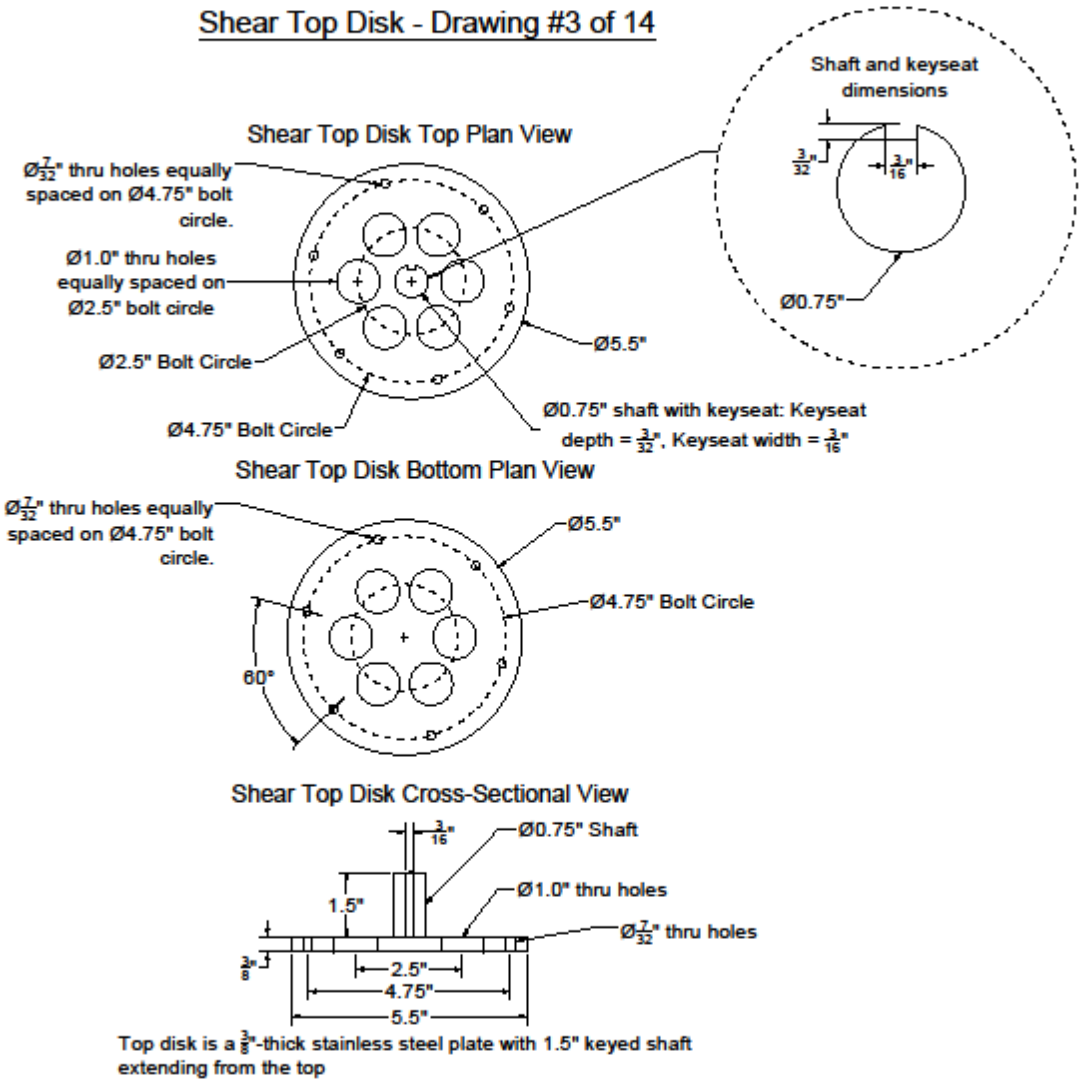

Fig A.3. Shear ring top disk component

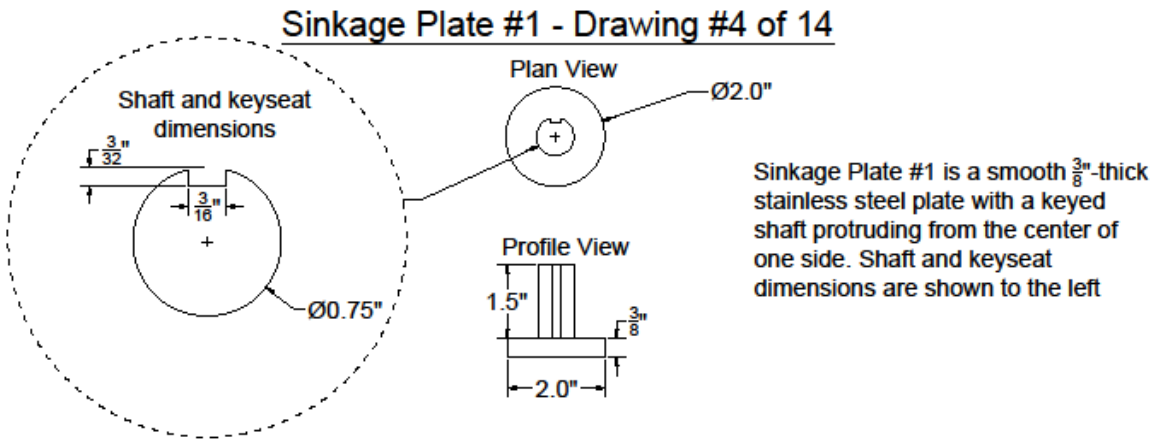

Fig. A.4. Sinkage plate 1

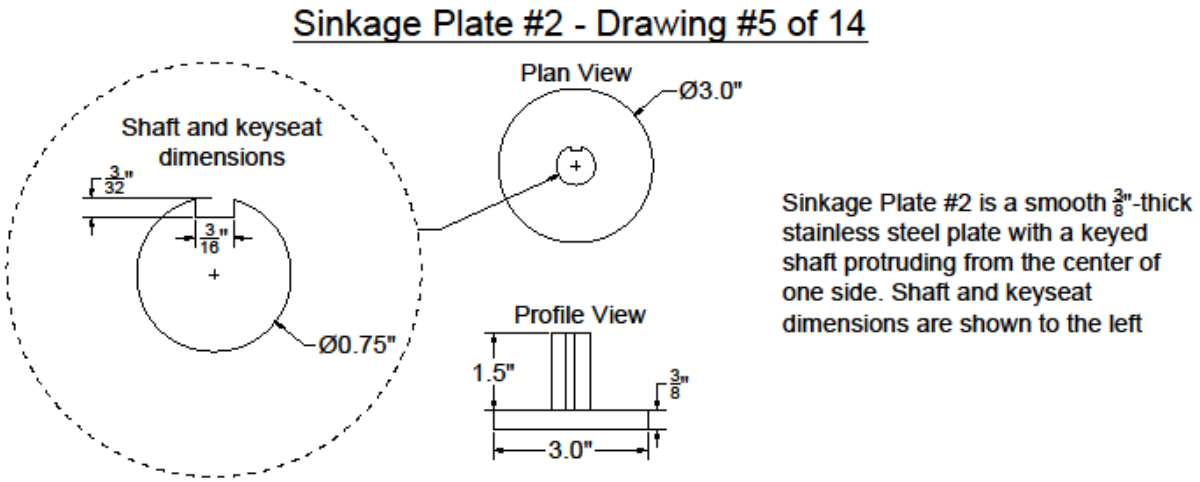

Fig. A.5. Sinkage plate 2

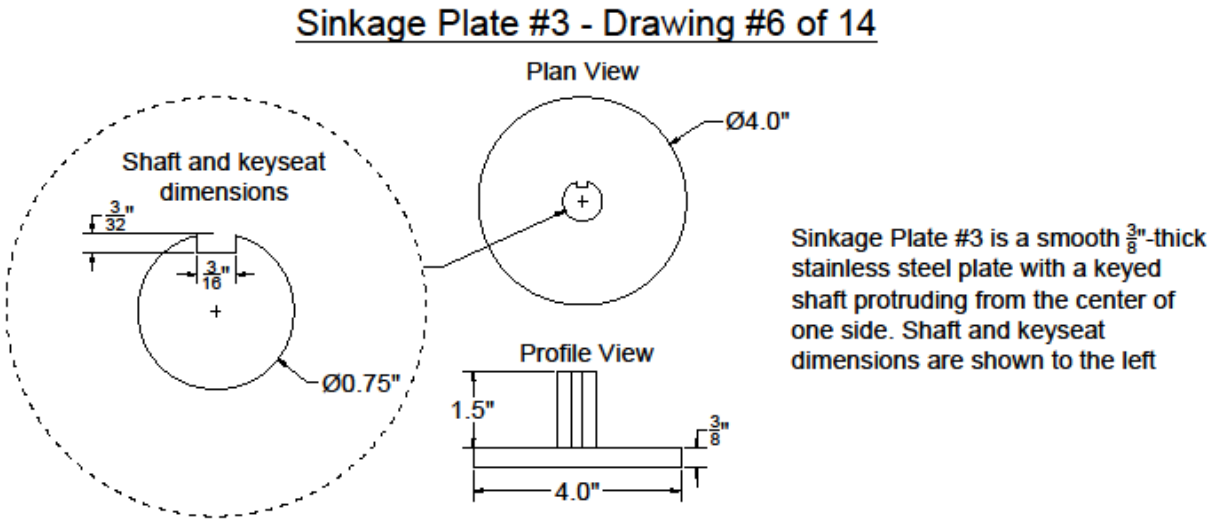

Fig. A.6. Sinkage plate 3

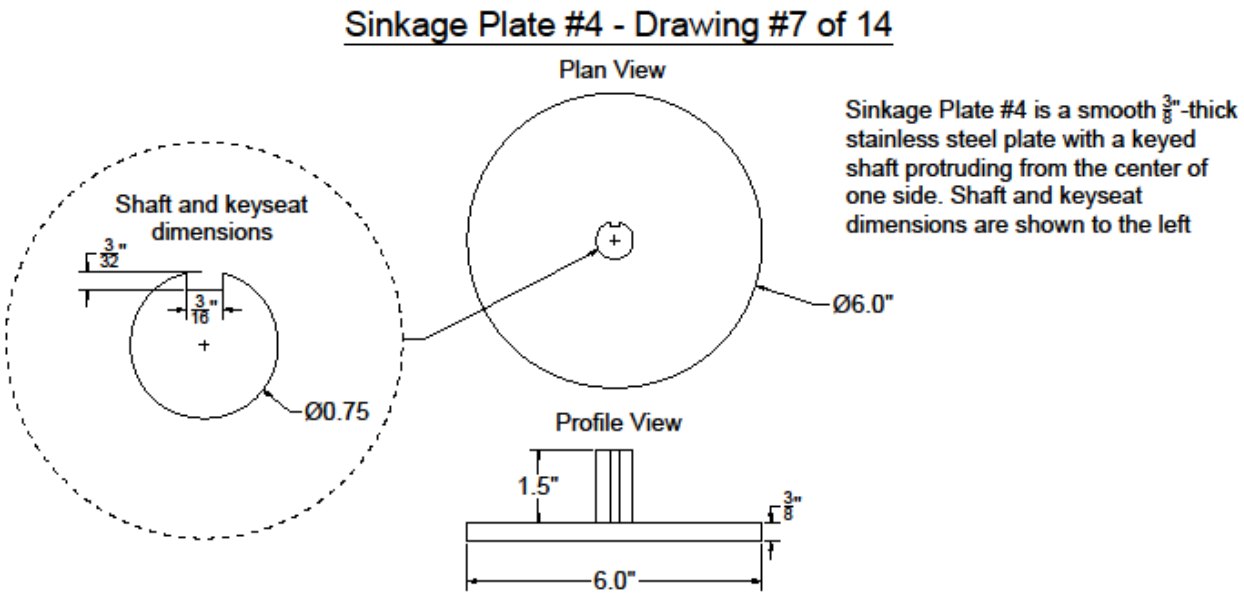

Fig. A.7. Sinkage plate 4

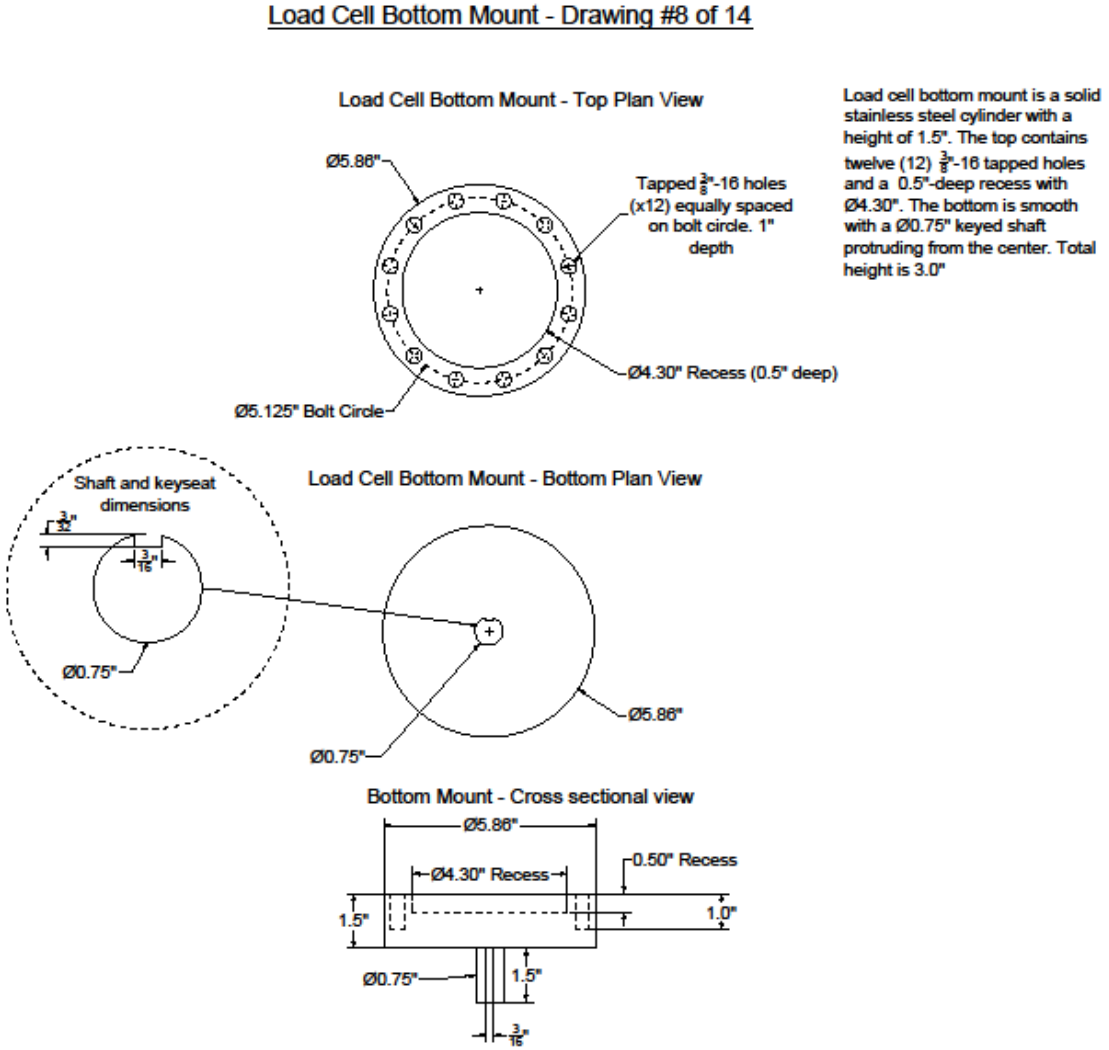

Fig. A.8. 2-Axis torsional load cell bottom mount

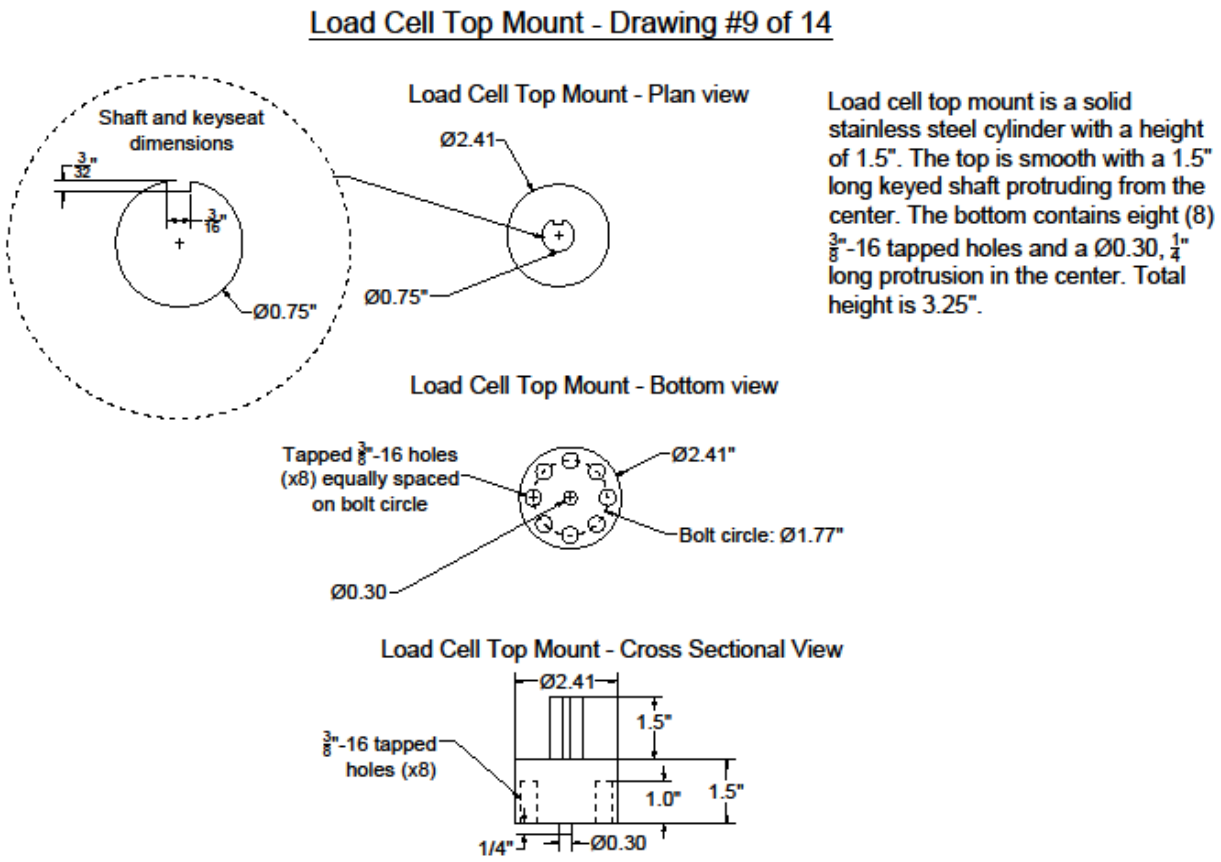

Fig. A.9. 2-axis torsional load cell top mount

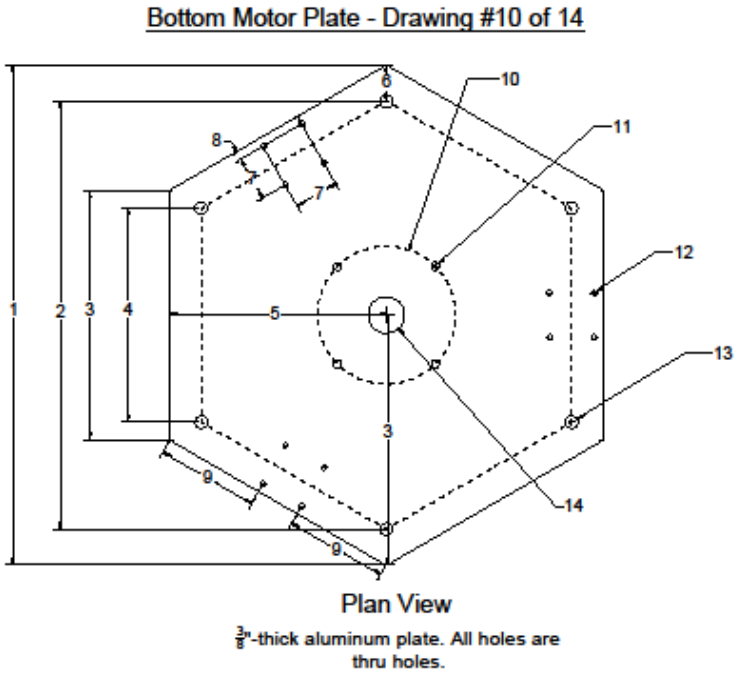

Dimensions	
1 - Regular Hexagon Plate Diameter	14.0
2 - Distance between opposite holes defined by (13)	12.00
3 Regular hexagon side length	7.0
4 - Distance between adjacent holes defined by (13)	6.00
5 - Midpoint of hexagon side to center	6.06
6 - Hexagon vertex to center of holes defined by (13)	1.00
7 - Side length of bolt squares with holes defined by (12) (x3)	1.25
8	0.24
9	2.875
10 - Bolt circle concentric with (14) and hexagon	Ø3.875
11 - Equally-spaced holes (x4) on (10)	Ø7/32
12 - Holes (x4) on square as defined by (7) (x12 total holes)	Ø5/32
13 - Holes (x6) located at each vertex of inner hexagon with diameter (2) and side length (4)	Ø3/8
14 - Hole concentric with hexagon and (10)	Ø1.0

All dimensions in inches
Note: Dashed hexagon represents the "inner hexagon" formed by 6 holes defined by (13). Dimension (2) is the diameter of this inner hexagon and dimension (4) is the side length

Fig. A.10. Bottom motor mounting plate

Top Motor Plate - Drawing #11 of 14

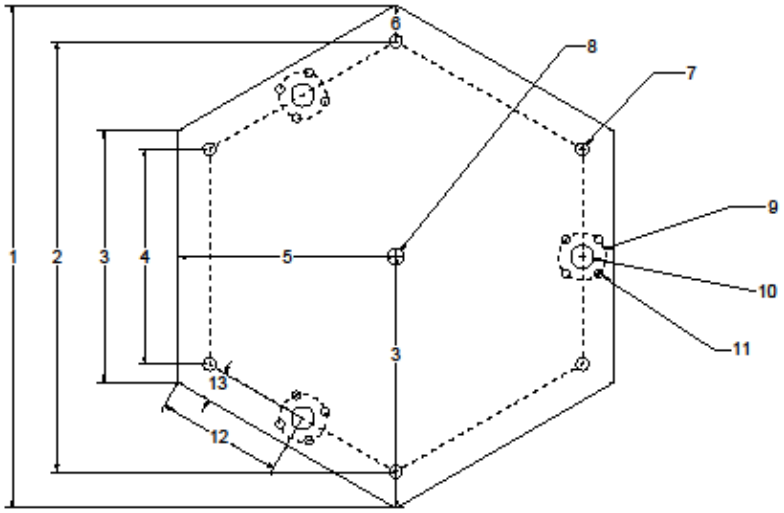

Plan View

$\frac{3}{8}$"-thick aluminum plate. All holes are thru holes.

Dimensions	
1 - Regular Hexagon Plate Diameter	14.0
2 - Distance between opposite holes defined by (7)	12.00
3 - Regular hexagon side length	7.0
4 - Distance between adjacent holes defined by (7)	6.00
5 - Midpoint of hexagon side to center	6.06
6 - Hexagon vertex to center of holes defined by (7)	1.00
7 - Holes (x6) located at each vertex of inner hexagon with diameter (2) and side length (4)	Ø$\frac{3}{8}$
8 - Hole concentric with hexagon	Ø$\frac{7}{16}$
9 - Bolt circle concentric with (10)	Ø1 $\frac{5}{16}$
10 - Holes (x3) concentric with (9)	Ø$\frac{5}{8}$
11 -Equally-spaced holes (x4) on each occurrence of (9) (x12 total)	Ø$\frac{7}{32}$
12	3.50
13	0.87

All dimensions in inches
Note: Dashed hexagon represents the "inner hexagon" formed by 6 holes defined by (7). Dimension (2) is the diameter of this inner hexagon and dimension (4) is the side length

Fig. A.11. Top motor mounting plate

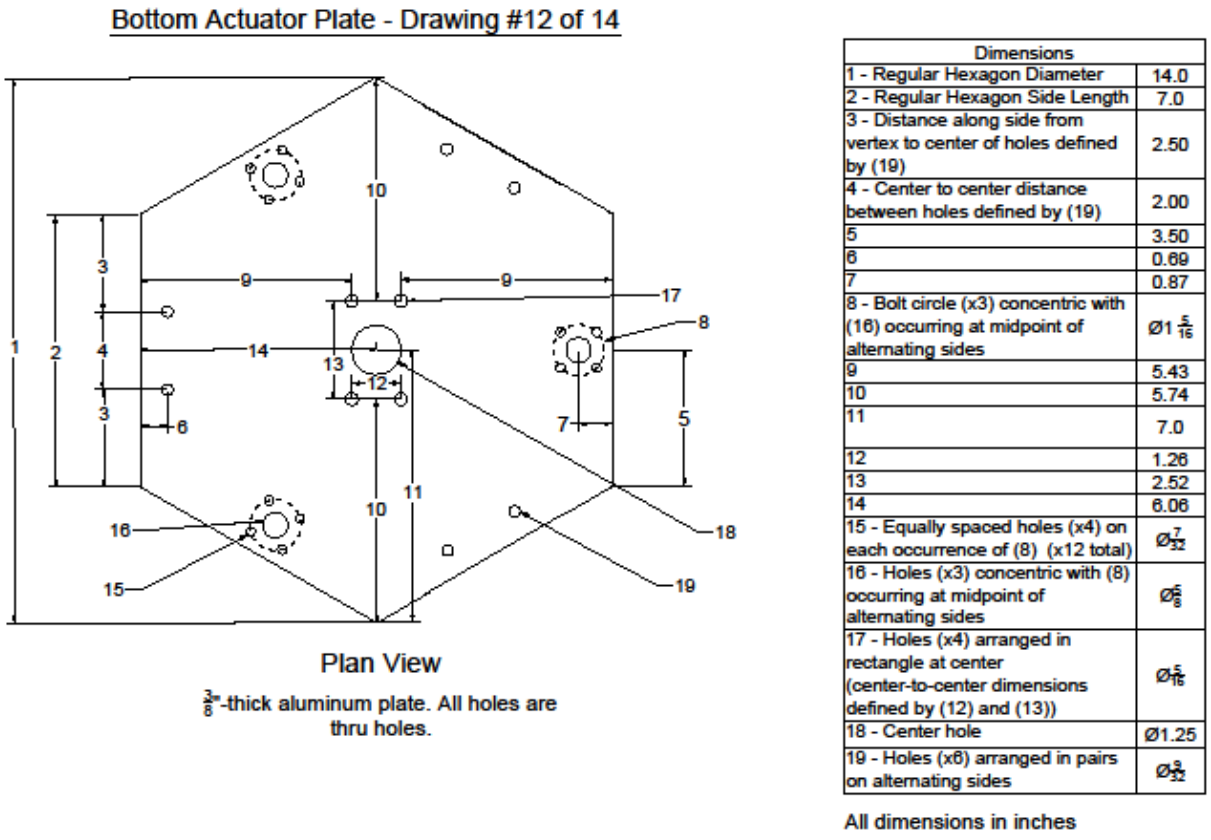

Dimensions	
1 - Regular Hexagon Diameter	14.0
2 - Regular Hexagon Side Length	7.0
3 - Distance along side from vertex to center of holes defined by (19)	2.50
4 - Center to center distance between holes defined by (19)	2.00
5	3.50
6	0.69
7	0.87
8 - Bolt circle (x3) concentric with (16) occurring at midpoint of alternating sides	Ø1 5/16
9	5.43
10	5.74
11	7.0
12	1.26
13	2.52
14	6.06
15 - Equally spaced holes (x4) on each occurrence of (8) (x12 total)	Ø7/32
16 - Holes (x3) concentric with (8) occurring at midpoint of alternating sides	Ø5/8
17 - Holes (x4) arranged in rectangle at center (center-to-center dimensions defined by (12) and (13))	Ø5/16
18 - Center hole	Ø1.25
19 - Holes (x6) arranged in pairs on alternating sides	Ø3/32

All dimensions in inches

Fig. A.12. Bottom actuator mounting plate

Top Actuator Plate - Drawing #13 of 14

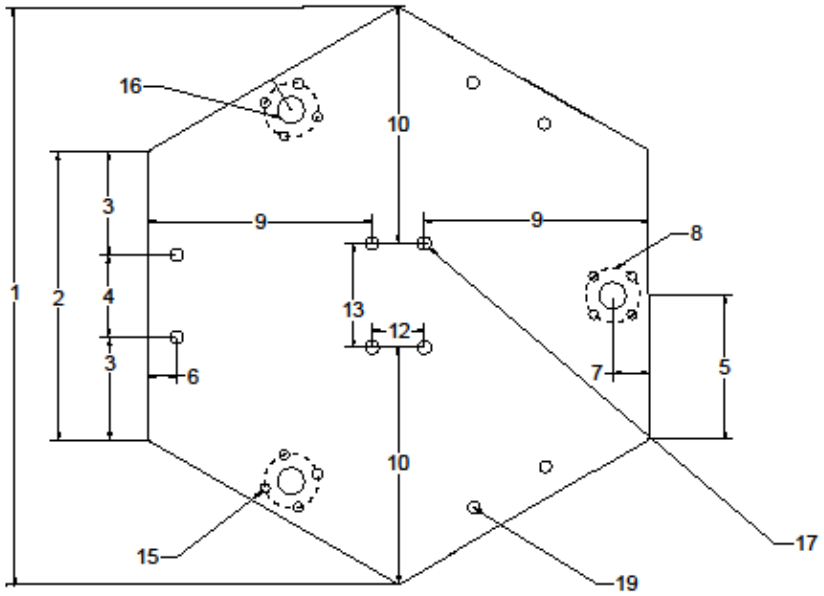

Plan View

$\frac{3}{8}$"-thick aluminum plate. All holes are thru holes.

Dimensions	
1 - Regular Hexagon Diameter	14.0
2 - Regular Hexagon Side Length	7.0
3 - Distance along side from vertex to center of holes defined by (19)	2.50
4 - Center to center distance between holes defined by (19)	2.00
5	3.50
6	0.69
7	0.87
8 - Bolt circle (x3) concentric with (16) occurring at midpoint of alternating sides	Ø1 $\frac{5}{16}$
9	5.43
10	5.74
11	7.0
12	1.26
13	2.52
14	6.06
15 - Equally spaced holes (x4) on each occurrence of (8) (x12 total)	Ø$\frac{7}{32}$
16 - Holes (x3) concentric with (8) occurring at midpoint of alternating sides	Ø$\frac{5}{8}$
17 - Holes (x4) arranged in rectangle at center (center-to-center dimensions defined by (12) and (13))	Ø$\frac{5}{16}$
18 - Holes (x6) arranged in pairs on alternating sides	Ø$\frac{9}{32}$

All dimensions in inches
Note: Dimensions 11 and 14 are not relevant to Top Actuator Plate

Fig. A.13. Top actuator mounting plate

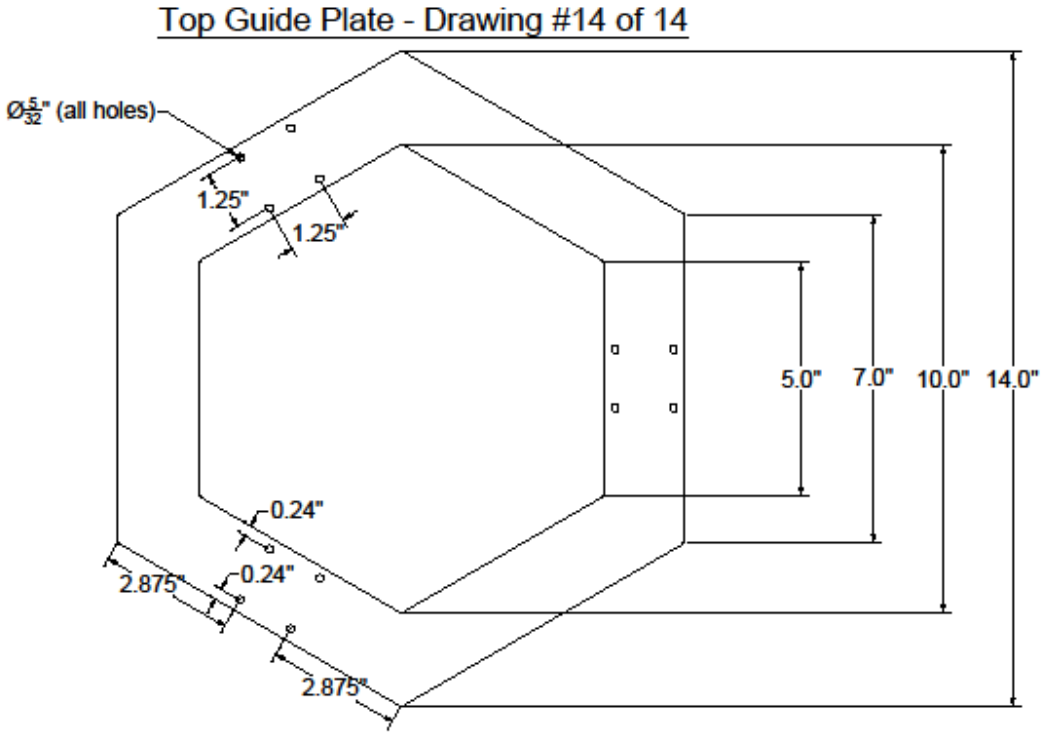

Fig. A.14. Top guide plate